



**AERODYNAMIC LOSS AND MIXING OVER A CAVITY FLAME HOLDER
LOCATED DOWNSTREAM OF PYLON-AIDED FUEL INJECTION**

THESIS

Lane C. Haubelt, Second Lieutenant, USAF

AFIT/GAE/ENY/06-M13

**DEPARTMENT OF THE AIR FORCE
AIR UNIVERSITY**

AIR FORCE INSTITUTE OF TECHNOLOGY

Wright-Patterson Air Force Base, Ohio

APPROVED FOR PUBLIC RELEASE; DISTRIBUTION UNLIMITED

The views expressed in this thesis are those of the author and do not reflect the official policy or position of the United States Air Force, Department of Defense, or the U.S. Government.

AFIT/GAE/ENY/06-M13

**AERODYNAMIC LOSS AND MIXING OVER A CAVITY FLAME HOLDER
LOCATED DOWNSTREAM OF PYLON-AIDED FUEL INJECTION**

THESIS

Presented to the Faculty

Department of Aeronautics and Astronautics

Graduate School of Engineering and Management

Air Force Institute of Technology

Air University

Air Education and Training Command

In Partial Fulfillment of the Requirements for the
Degree of Master of Science in Aeronautical Engineering

Lane C. Haubelt, B.S. Aeronautical Engineering

Second Lieutenant, USAF

March 2006

APPROVED FOR PUBLIC RELEASE; DISTRIBUTION UNLIMITED

**AERODYNAMIC LOSS AND MIXING OVER A CAVITY FLAME HOLDER
LOCATED DOWNSTREAM OF PYLON-AIDED FUEL INJECTION**

Lane C. Haubelt, B.S. Aeronautical Engineering

Second Lieutenant, USAF

Approved:

/signed/

23 March 2006

Paul I. King

Date

/signed/

23 March 2006

Richard D. Branam

Date

/signed/

23 March 2006

Mark F. Reeder

Date

Abstract

Cavity-based fuel injection and flame holding, typically found in hydrocarbon-fueled scramjet applications, are of current interest for use in supersonic combustors. Both the Air Force Research Lab (AFRL) and the Air Force Institute of Technology (AFIT) at Wright-Patterson Air Force Base in Ohio are investigating the enhancement of fuel-air mixing with small pylons that project into the supersonic flow upstream of a flame holder cavity. This work follows previous qualitative (Mie scattering and NO-PLIF visualizations) results which suggested that these small pylons, combined with injection, may improve fuel-air mixing. The pylons were of three sizes (medium, tall, and wide) and shaped as a thin triangular wedge with a 30° inclination angle. A total of four configurations (pylons plus baseline) were tested at two different fuel injection pressures. The facility, provided by AFRL, was a supersonic (Mach 2) continuous flow wind tunnel with an existing cavity and pylon setup. The goal was to measure the mixing efficiency and shock loss of each pylon setup for comparison to the baseline condition of transverse injection without pylons. Non-reacting flow was measured using intrusive and non intrusive techniques to obtain pitot pressure, total temperature, cone-static pressure and laser induced Raman spectroscopy to determine species concentration over the cavity downstream of the injection port. Results demonstrated that pylons increase fuel penetration, while not adding significantly to shock losses or overall mixing compared to baseline.

Acknowledgments

I would like to express my sincere gratitude to my faculty advisor, Dr. Paul King, for his patient guidance and instruction throughout this process. His insight and experience was appreciated. My sponsor, Dr. Mark Gruber from AFRL Propulsion Directorate has my deepest respect and thanks for the support he provided to me in this endeavor.

I am indebted to Dr. Campbell Carter from AFRL/PR and Dr. Mark Hsu from ISSI for the countless hours spent guiding me through the experiment and data reduction process. Many thanks go to the Bill Terry and Dave Schommer who spent their valuable time explaining and running the testing facility.

I would like to thank my family for their encouragement and love. Finally, thanks to my wife who patiently endured the late nights and weekends spent on this project. She sustained me throughout.

Lane C. Haubelt

Table of Contents

	Page
Abstract.....	iv
Acknowledgments.....	v
List of Figures	ix
List of Tables	xiii
Page.....	xiii
Nomenclature	xiv
1. Introduction.....	1
1.1. Background.....	1
1.2. Aim of Experimental Investigation	3
1.3. Research Objectives.....	3
2. Literature Review.....	4
2.1. Scramjet Propulsion Overview	4
2.2. Supersonic Combustors	5
2.3. Cavity Flame holders.....	6
2.4. Transverse Fuel Injection and Mixing.....	9
3. Experimental Methods.....	12
3.1. Test Facility	12
3.1.1. Wind Tunnel	12
3.1.2. Test Section Cavity	15
3.1.3. Fuel Injection	17
3.2. Pylons	17
3.3. Dynamic Pressure Ratio	21
3.4. Testing Strategy	23
3.4.1. Overview.....	23
3.4.2. Test Matrix.....	25
3.5. Species Composition Sampling	26
3.5.1. Overview.....	26
3.5.2. Principle of Operation.....	28
3.5.3. Instrumentation	34
3.5.4. Calibration	37

	Page
3.6. Aerothermodynamic Probing.....	38
3.6.1. Overview.....	38
3.6.2. Pitot Pressure Probe.....	41
3.6.3. Cone-Static Probe.....	41
3.6.4. Total Temperature Probe.....	42
3.6.5. Calibration.....	43
3.7. Shadowgraph Photography.....	43
3.7.1. Principle of Operation.....	43
3.7.2. Instrumentation.....	44
3.8. Laboratory Procedure.....	46
3.8.1. Overview.....	46
3.8.2. Species Composition.....	47
3.8.3. Aerothermodynamic Probing.....	48
3.8.4. Shadowgraph.....	49
4. Data Reduction.....	50
4.1. Non-dimensionalization.....	50
4.2. Species Composition.....	50
4.2.1. Overview.....	50
4.2.2. Determination of Number Density.....	51
4.2.3. Mole Fraction and Equivalence Ratio.....	55
4.2.4. Summary.....	57
4.3. Aerothermodynamic Probing.....	58
5. Results and Discussion.....	63
5.1. Overview of Data Analysis.....	63
5.2. Shadowgraphs.....	63
5.3. Species Composition Contour Plots.....	74
5.4. Mixing Analysis.....	79
5.4.1. Overview.....	79
5.4.2. Fuel Penetration.....	80
5.4.2.1. Plume Penetration Height Comparison.....	81
5.4.2.2. Core Penetration Height Comparison.....	83
5.4.2.3. Comparison to Previous Research.....	85
5.4.2.4. Penetration Trajectory.....	87
5.4.3. Decay of Maximum Equivalence Ratio.....	90
5.4.4. Plume Area.....	94
5.4.4.1. Plume Area Comparison.....	95
5.4.4.2. Plume Spreading.....	97
5.4.5. Mixing Efficiency.....	101
5.5. Aerodynamic Loss Analysis.....	103

	Page
5.5.1. Overview.....	103
5.5.2. Total Pressure Contours.....	103
5.5.3. Mach Number Contours	108
5.5.4. Total Pressure Loss Coefficient.....	113
6. Conclusions and Recommendations	115
6.1. Experiment Overview	115
6.2. Synopsis of Results.....	115
6.3. Conclusions of Research.....	118
6.4. Recommendations for Future Action.....	120
Appendix A Species Sampling and Aerothermodynamic Probing Data Meshes.....	121
Appendix B Image Correction Methods	124
Appendix C High Resolution Equivalence Ratio Plots.....	131
Appendix D Method of Least Squares Correlation	133
Appendix E Error Analysis	134
E-1 Overview.....	134
E-2 Species Composition Sampling: Equivalence Ratio Uncertainty.....	135
E-3 Aerothermodynamic Probing Uncertainty	137
E-4 Dimensional Uncertainty	137
Appendix F Supplementary Pressure Data.....	139
Bibliography	148
Vita.....	153

List of Figures

	Page
Figure 1. Schematic diagram of a ramjet	4
Figure 2. Dual-mode scramjet combustor technical challenges	5
Figure 3. Rectangular cavity design with shear layer impingement	7
Figure 4. Cavity flame holder design with ramp for acoustic wave suppression	8
Figure 5. Perspective of transverse jet injection	10
Figure 6. Supersonic combustion facility schematic	13
Figure 7. Profile view of tunnel midsection.....	14
Figure 8. Closeup profile view of test section cavity.....	16
Figure 9. Simplified schematic of cavity	16
Figure 10. Pylon and injection port geometry	18
Figure 11. Pylon inserts used in research.....	20
Figure 12. Pylon location relative to the cavity	21
Figure 13. Polarization of a molecule induced by an electric field	30
Figure 14. Radiation incident upon a diffraction grating.....	31
Figure 15. Schematic of single point Raman experiment setup	33
Figure 16. Example single point stokes Raman spectrum in bi-species medium.....	33
Figure 17. Left side-view of Raman spectroscopy setup.....	34
Figure 18. Skewed right-view of Raman spectroscopy setup.....	35
Figure 19. Schematic of planar Raman scattering setup used in experiment	36
Figure 20. Calibration Raman scattering a) 0.0 mm and b) 15.2 mm from centerline	38
Figure 21. Probe actuator and wall traverse plate system.....	39

	Page
Figure 22. Side and top views of cone-static probe installed in tunnel	40
Figure 23. Total temperature and pitot probes used in experiment	40
Figure 24. Illustration of a simple shadowgraph	44
Figure 25. Profile view of shadowgraph setup, flow from right to left	45
Figure 26. View of camera and target screen used in shadowgraph.....	46
Figure 27. Tunnel Raman scattering of air at atmospheric conditions	51
Figure 28. Tunnel Raman scattering for ethylene-air mixture at atmospheric conditions	53
Figure 29. Raman spectrum at $x/d = 12$, $y/d = 4.92$ for baseline configuration.....	55
Figure 30. Shadowgraph of baseline configuration without injection.....	68
Figure 31. Shadowgraph of medium configuration without injection.....	68
Figure 32. Shadowgraph of tall configuration without injection.....	69
Figure 33. Shadowgraph of wide configuration without injection	69
Figure 34. Shadowgraph of baseline configuration with $\bar{q} =$ a) 1.0 and b) 4.0.	70
Figure 35. Shadowgraph of medium configuration with $\bar{q} =$ a) 1.0 and b) 4.0.	71
Figure 36. Shadowgraph of tall configuration with $\bar{q} =$ a) 1.0 and b) 4.0.	72
Figure 37. Shadowgraph of wide configuration with $\bar{q} =$ a) 1.0 and b) 4.0.	73
Figure 38. Baseline equivalence ratio contours for a), c), e) $\bar{q} = 1$ and b), d), f) $\bar{q} = 4.75$	
Figure 39. Wide equivalence ratio contours for a), c), e) $\bar{q} = 1$ and b), d), f) $\bar{q} = 4$	77
Figure 40. Medium equivalence ratio contours for a) $\bar{q} = 1$ and b) $\bar{q} = 4$	78
Figure 41. Tall equivalence ratio contours for a) $\bar{q} = 1$ and b) $\bar{q} = 4$	79
Figure 42. Plume penetration (h_p/d) comparison between inserts at $x/d = 12$	81

	Page
Figure 43. Plume core penetration (h_c/d) comparison between inserts at $x/d = 12$	83
Figure 44. Ethylene plume penetration trajectory.....	88
Figure 45. Ethylene plume core penetration trajectory.....	89
Figure 46. Maximum equivalence ratio decay vs. axial distance for wide and baseline inserts	92
Figure 47. Total (A_p) and flammable plume (A_f) area comparison for all inserts at $x/d = 12$	95
Figure 48. Total plume area (A_p) trajectory for baseline and wide inserts	98
Figure 49. Flammable plume area (A_f) trajectory for baseline and wide inserts	99
Figure 50. Normalized total pressure contours at $x/d = 12$	106
Figure 51. Mach number contours at $x/d = 12$	111
Figure 52. Raman scattering for wide insert at $x/d = 7.2$, $y/d = 16$, $z/d = -8$	125
Figure 53. Background subtracted Raman scattering for wide insert, $x/d = 7.2$, $y/d = 16$, $z/d = -8$	126
Figure 54. Equivalence ratio with correction step 1 for wide insert, $x/d = 7.2$ and $y/d = 16$	127
Figure 55. Equivalence ratio with correction steps 1 and 2, wide insert, at $x/d = 7.2$ and $y/d = 16$	128
Figure 56. Equivalence ratios with and without correction Step 3, wide insert, $x/d = 7.2$ and $y/d = 8$	129
Figure 57. High resolution equivalence ratio contours for baseline, $\bar{q} = 1.0$ and 4.0 ...	132
Figure 58. High resolution equivalence ratio contours for wide, $\bar{q} = 1.0$ and 4.0	132

	Page
Figure 59. Supplementary pressure plots for baseline, $q = 1.0$ at $x/d = 12$	140
Figure 60. Supplementary pressure plots for baseline, $q = 4.0$ at $x/d = 12$	141
Figure 61. Supplementary pressure plots for the medium pylon, $q = 1.0$, at $x/d = 12$	142
Figure 62. Supplementary pressure plots for the medium pylon, $q = 4.0$, at $x/d = 12$..	143
Figure 63. Supplementary pressure plots for the tall pylon, $q = 1.0$ at $x/d = 12$	144
Figure 64. Supplementary pressure plots for the tall pylon, $q = 4.0$ at $x/d = 12$	145
Figure 65. Supplementary pressure plots for the wide pylon, $q = 1.0$ at $x/d = 12$	146
Figure 66. Supplementary pressure plots for the wide pylon, $q = 4.0$ at $x/d = 12$	147

List of Tables

	Page
Table 1. Geometries for medium, tall and wide pylons.....	20
Table 2. Summary of freestream flow conditions at nozzle exit	24
Table 3. Summary of jet conditions at injection port exit.....	24
Table 4. List of inputs and resulting outputs for Fuller algorithm.....	58
Table 5. Plume penetration (h_p/d) comparison between inserts at $x/d = 12$	82
Table 6. Plume core penetration (h_p/d) comparison between inserts at $x/d = 12$	84
Table 7. Comparison of current and previous plume penetration at $x/d = 12$	86
Table 8. Plume penetration trajectory for the wide and baseline inserts	90
Table 9. Maximum equivalence ratios for configurations	91
Table 10. Flammable plume percentage for each configuration at $x/d = 12$	96
Table 11. Flammable plume percentage for baseline and wide inserts	99
Table 12. Mixing efficiency (η_m) for all configurations at $x/d = 12$	102
Table 13. Total pressure loss coefficient ($\bar{\omega}$) for all configurations at $x/d = 12$	114
Table 14. Species sampling data mesh used for each run.....	122
Table 15. Aerothermodynamic probing data mesh used for each run	123
Table 16. Illustration of assignment array used for median filtering.....	129
Table 17. Species composition sampling uncertainty	134
Table 18. Aerothermodynamic probing uncertainty	135

Nomenclature

A_f	Flammable Plume Area
A_i	Injection Port Area
A_p	Total Plume Area
B_n	Image Background Magnitude
C	Molar Density
D	Cavity Depth
E	Electric Field Strength
E_o	Vibrational Amplitude
FPP	Flammable Plume Percentage
$I_{m,n}^l$	Local Background Intensity Image
$I_{m,n}^r$	Raw Raman Scattering Image
$\bar{I}_{m,n}^f$	Average Freestream Intensity Image
L	Cavity Length
M_j	Jet Mach Number
MW	Molecular Weight
M_∞	Freestream Mach Number
\mathcal{M}	Molecule
N	Number Density
\mathcal{N}_A	Avogadro's Number
P	Static Pressure
P_j	Jet Exit Static Pressure
P_t	Total Pressure
$P_{t,ref}$	Plenum Stagnation Pressure
\bar{P}_t	Mass-averaged Total Pressure
$P_{\bar{x}}$	Precision Uncertainty Interval of the Mean
$Px_{i,j}$	Image Pixel
P_∞	Freestream Static Pressure
\mathcal{P}	Induced Dipole Moment
R	Specific Gas Constant
RSS	Root Sum of the Squares
S	Raman Scattering Intensity
T	Static Temperature
T_o	Stagnation Temperature
T_r	Recovery Temperature
T_t	Total Temperature
U_∞	Freestream Velocity
W	Pylon Width
X	Mole Fraction
X_p	Injection Proximity
a_∞	Freestream Speed of Sound

c_p	Specific Heat, Constant Pressure
c_v	Specific Heat, Constant Volume
d	Injection Port Diameter
h_c	Jet Core Penetration
h_p	Jet Plume Penetration
\hbar	Incident Photon
k	Optical Calibration Constant
ℓ	Pylon Length
m	Diffraction Order
\dot{m}	Mass Flow Rate
n	Power-Law Rate Variable
q	Dynamic Pressure
\bar{q}	Dynamic Pressure Ratio
r	Recovery Factor
s_{grat}	Grating Groove Spacing
u_j	Jet Exit Velocity
w	Uncertainty Interval
x	Tunnel Streamwise Coordinate
x_{fm}	Fully Mixed Distance
x_{flam}	Flammable Mixture Distance
y	Tunnel Transverse Coordinate
z	Tunnel Spanwise Coordinate
Φ	Equivalence Ratio
Φ_L	Lower Flammability Limit
Φ_{max}	Maximum Equivalence Ratio
Φ_U	Upper Flammability Limit
α	Polarizability
β	Power-Law Coefficient
δ_i	Incident Light Angle
δ_r	Reflected Light Angle
γ	Ratio of Specific Heats
η_m	Mixing Efficiency
λ	Incident Light Wavelength
ν_o	Incident Photon Frequency
ν_m	Molecular Vibrational Frequency
$\tilde{\nu}$	Wavenumber
θ	Pylon Wedge Angle
ρ_j	Jet Exit Density
ρ_∞	Freestream Density
$\bar{\omega}$	Total Pressure Loss Coefficient

AERODYNAMIC LOSS AND MIXING OVER A CAVITY FLAME HOLDER LOCATED DOWNSTREAM OF PYLON-AIDED FUEL INJECTION

1. Introduction

1.1. *Background*

Efficient fuel injection and mixing is critical to successful development of a hypersonic air-breathing propulsion system. Supersonic velocities within the combustor section limit the time fuel can mix with the air flow. Surface interactions with the flow create undesirable losses and drag. A current area of interest is cavity-based flame holders within the combustor section. This type of flame holder has demonstrated lower drag than conventional intrusive designs, while providing a low momentum region for flame stabilization.^{1,2} However, the need still remains for efficient methods of fuel injection.

Ongoing experimentation at the Air Force Research Laboratory Propulsion Directorate (AFRL/PR) at Wright-Patterson Air Force Base (WPAFB) aims to enhance supersonic combustion through pylon-aided transverse fuel injection. Intrusive devices such as pylons create disturbances in the flow which may be beneficial to fuel mixing and penetration. Conventional intrusive injection such as ramp and strut injectors have been shown to increase mixing potential due to vortex formation, but because of their large surface area, they tend to suffer severe loss penalties and thermal loading. Thin, swept pylons are employed to reduce aerodynamic losses while maintaining the high mixing potential associated with intrusive injectors.³ Initial research utilizing pylons placed

upstream of injection ports have shown increased fuel penetration and the possibility for similar or better pressure loss recovery than seen in transverse injection alone. Penetration lifts the fuel plume into the freestream and away from the combustor wall, shortening combustor length and preventing boundary layer flashback, or the ignition of fuel which has become entrained in the boundary layer.⁴ Use of pylon injection systems may improve total combustor performance when coupled with cavity-based flame holders.

Previous work by Montes et al.⁵ employed three pylons, configured with circular transverse injection ports at their base and installed upstream of a cavity flame holder employed at the AFRL Supersonic Combustion Facility. State-of-the-art non-intrusive visualization techniques were used to gather qualitative information regarding the ability of the pylons to improve fuel mixing and penetration at various injection pressures. The research was performed in a non-reacting Mach 2 flow environment. Each pylon was a triangular wedge with a 30° inclination. Pylon designs were based on the two best geometries determined from a computational study⁶, and correlated with sizes used in separate experimental work.^{7,8} The research showed that pylons improve penetration and mixing potential over baseline transverse injection case without a pylon. However, due to the techniques used, information on aerodynamic losses could not be obtained. The purpose of the present research is to build upon the previous work and procure quantitative data on both supersonic mixing and flow losses for pylon-aided pre-injection upstream of a cavity flame holder.

1.2. Aim of Experimental Investigation

Using the three pylon configurations implemented in previous research at the Supersonic Combustion Facility, this experiment seeks to gain understanding in two areas: the pylons' effect on fuel mixing and supersonic aerodynamic losses. The pylons are compared to a baseline configuration of transverse injection with no pylon. Fuel injection pressure is varied to gauge its contribution to the mixing process. Gaseous ethylene (C_2H_4) is used as the injectant.

Four total configurations are tested: three pylons (which varied in size and geometry), and a baseline (no pylon). All pylons are inserted along the tunnel centerline approximately 0.14 cavity lengths upstream of the flame holder. A single, circular injection port is placed immediately downstream of the pylons. The intent of the research is to compare injection schemes to determine optimal design for a supersonic combustor utilizing pre-injection upstream of a cavity-based flame holder.

1.3. Research Objectives

The research objectives are:

- *Quantify pylon's contribution to fuel dispersion and penetration.*
- *Determine pylon's contribution to aerodynamic losses.*

2. Literature Review

2.1. *Scramjet Propulsion Overview*

In the quest to achieve high Mach number flight, significant issues must be overcome. High stagnation temperatures and large drops in total pressure prevent traditional turbine engines from operating at Mach numbers above 4.0.⁹ Within this flight regime, a ramjet maximizes simplicity, performance and high temperature tolerance. The concept shown in Figure 1¹⁰, valid at flight Mach numbers $2 < M_\infty < 6$, operates by compressing the air as it enters the inlet. To provide stable combustion, the flow remains subsonic throughout the interior of the engine. However, at Mach numbers around 6, the incoming air temperature is so high that most of the chemical energy is transferred into dissociation reactions preventing combustion from occurring.¹¹ Much research and

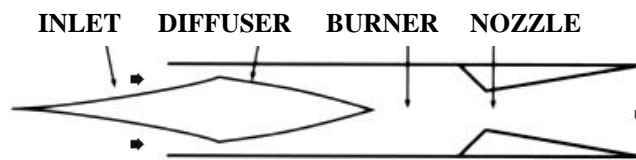


Figure 1. Schematic diagram of a ramjet¹⁰

development has been and continues to be done on a ramjet with supersonic combustion (scramjet). By introducing the air into the engine interior at supersonic velocities, the temperature rise and pressure losses associated with a ramjet are reduced. Mach numbers for scramjets proceed well into the hypersonic realm ($M_\infty > 5$). Dual-mode scramjets

broaden the operable Mach number range to include Mach numbers below 5. Many formidable challenges are associated with dual-mode scramjet combustion as shown in Figure 2.¹² Fuel must be injected, mixed, and burned in approximately one millisecond. This process must be done efficiently while minimizing total pressure losses and keeping the combustor length short to reduce drag and surface exposure to high temperatures.¹³

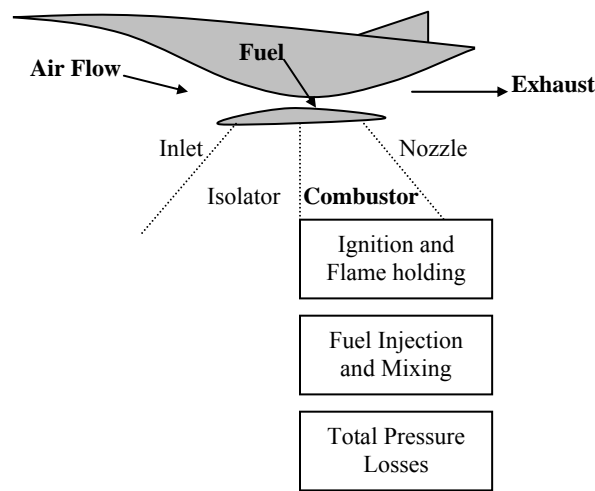


Figure 2. Dual-mode scramjet combustor technical challenges

2.2. Supersonic Combustors

Current dual-mode scramjet designs incorporate a diverging combustor section downstream of the isolation section. This isolation section is of constant area, it is designed to allow engine operation over a wider range of Mach numbers while preventing inlet unstart (caused by high increases in pressure from combustion from far upstream).¹⁴ Once in the combustor, fuel is injected, mixed, and burned, causing a rise in temperature

high enough to thermally choke the flow. The choked flow is then accelerated through the diverging section of the combustor and out the nozzle.^{15,16}

Proper fuel choice is important to any scramjet combustor design. Hydrogen is a popular fuel choice because of its short ignition delay and high energy release.¹² However, its high volatility and low density create operational difficulty. Despite their increased ignition delay and lower useful Mach limits (Mach 8), hydrocarbon fuels are much more feasible from an operational standpoint.¹⁷

Any design of a scramjet combustor must address three important factors: fuel injection strategy, ignition and flameholding.¹⁸ While efficient injection is important, it alone cannot support combustion. Flame holders have been employed to create a stable environment for continuous combustion to take place.¹⁸ In an effort to minimize flow disturbances and improve fuel residence time and mixing, recessed cavity flame holders have been the focus of current research.

2.3. Cavity Flame holders

Because of their aerodynamic uses, supersonic flow over cavities is studied extensively. Research into their uses as a flame holder for supersonic combustors began in the 1950s¹⁹ and has experienced a surge of interest since the early 1990s. Further stimulating the field, flight tests of supersonic combustors employing cavities have shown their effectiveness as flame holding mechanisms.¹⁸ A simple cavity design shown in Figure 3 incorporates two 90° steps recessed away from the surface. Subsonic,

recirculation zones within the cavity increase residence time of entrained fuel, making cavities conducive to fuel mixing and flame holding.

Typically, cavity geometries are defined by their length to depth ratio (L/D). The first type of cavity is termed open and generally has L/D less than 7-10. Open cavities are characterized by a reattachment of a shear layer to the rear step (see Figure 3). If the value for L/D is high enough (greater than 10-13), the shear layer reattaches to the cavity floor and the cavity is termed “closed”. Closed cavities are rarely used because of severe drag penalties.¹⁸

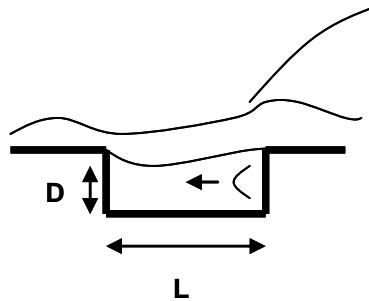


Figure 3. Rectangular cavity design with shear layer impingement¹⁸

Open cavities form a shear layer between the higher momentum core flow and the subsonic flow in the cavity. This shear layer is unsteady and impinges on the rear wall allowing mass to enter.¹⁸ This causes a cavity pressure increase and creates self-sustaining longitudinal pressure oscillations that result in drag. Resonance may be controlled and stabilized by slanting the back wall at an angle.^{20,21} The design shown in Figure 4a suppresses the unsteady shear layer and acts to eliminate the acoustic wave.¹⁸ Geometric intrusions or injection upstream of the cavity may further enhance cavity stability by tripping the flow and enhancing shear layer growth; Figure 4b shows this effect. Furthermore, research by Yu et al. determined that this geometry is efficient in increasing

combustor pressure and exit recovery temperature.²² Since these modifications are typically permanent, it is advantageous to design these open cavities for optimal performance.

Research performed by Gruber et al. on slant-wall cavities have shown that drag is reduced at optimal ramp angles.^{1,2} If the ramp angle is too low, the expansion wave created at the cavity lip couples with the shear layer impingement further down into the cavity and creates a large recompression on the rear face. Additionally, further research by Gruber

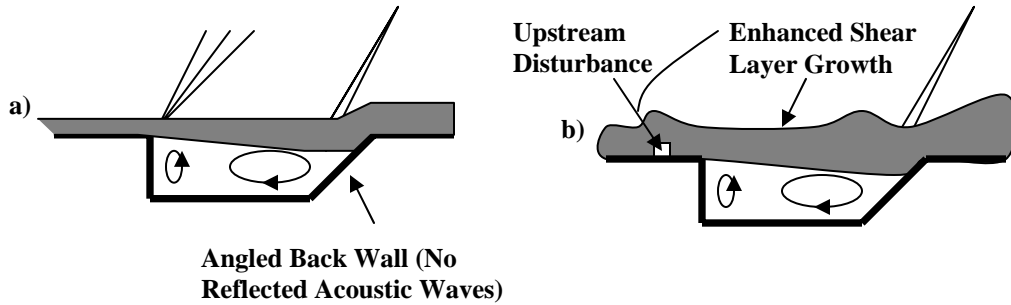


Figure 4. Cavity flame holder design with ramp for acoustic wave suppression¹⁸

and Hsu measured combustor performance as a function of cavity size, L/D and ramp angle and concluded that ramp angle is the largest contributor to drag.²³ Current research aims at coupling enhanced core flow mixing from upstream injection with the robustness of flame holding cavities.^{24,25,26}

2.4. Transverse Fuel Injection and Mixing

Many injection schemes have been employed, typically either flush mounted or intrusive to improve the mixing potential of the system^{13,14,27,28,29}. The goal of injection is to introduce fuel into the flow using a scheme that provides rapid mixing with minimal pressure loss and stable combustion. Transverse injection offers relatively rapid near-field mixing and penetration due to its high jet-to-freestream momentum flux ratio.¹³ However, a large three-dimensional bow shock forms because of the jet's obtrusive nature and strong crossflow interaction. Experiments involving angled injection are shown to reduce the bow shock strength and thereby decrease pressure loss associated with transverse injection.³⁰ Furthermore, at Mach numbers above approximately 10, angled injectors significantly add to net engine thrust.²⁸ However, the angled injectors create poor near-field mixing which causes unfavorable delays in ignition until much further downstream of the jet. Therefore, due to its superior mixing characteristics at lower Mach numbers, transverse injection is the favorable injection scheme for dual-mode scramjets.³¹

Schetz, et al presented a comprehensive survey of supersonic mixing of transverse and wall jets.³² Early research of transverse jets provided descriptions of their structure.³³ Figure 5³⁴ shows the local flow field around an under-expanded transverse injector. The jet introduces fluid perpendicular to the direction of flow causing a highly three-dimensional bow shock to form. This bow shock interacts with the incoming boundary

layer and forms a separated area ahead of and immediately behind the injector.³⁵ The penetration of the fluid into the freestream is dependent upon the jet-to-freestream momentum flux ratio. However, drag and induced pressure losses also increase with jet momentum.³⁶ The fluid initially expands and accelerates forming a barrel shock around

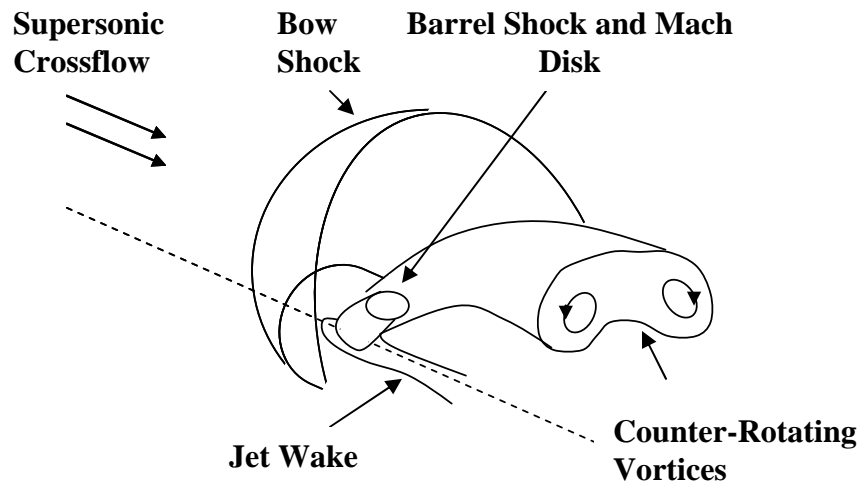


Figure 5. Perspective of transverse jet injection

the jet. A Mach disk normal to the jet occurs and compresses the emerging plume. Most of the fuel plume bypasses the barrel shock and Mach disk forming a shear layer with the supersonic crossflow. This shear layer may penetrate two to three times higher than the center of the Mach disk.³⁴ As the freestream momentum begins to dominate and turn the jet plume, two counter-rotating vortices form. The mechanism behind the formation of the vortex pair is not completely understood, but the general consensus is that they are created by the interaction between the vortex sheet emanating from the injection port and the freestream.³⁷ It is certain though that the counter-rotating vortices enhance mixing by transporting air into the plume interior from the crossflow.³⁴

It is known that jet vorticity positively enhances fuel mixing. The introduction of swirl into the transverse injector port is shown to increase mixing potential and jet plume total area without increasing shock losses.³⁸ Higher mixing also occurs due to vorticity generated by intrusive objects such as ramps and struts.³⁹ Work done by Fuller et al. concluded that while physical ramp injectors have superior mixing due to vortex generation, pressure losses created are much greater when compared to aerodynamic ramps.²⁹ In an attempt to balance mixing efficiency and pressure loss, thin pylons inserted upstream of transverse injectors have been suggested as an alternative.^{3,4} These pylons enhance mixing and penetration by creating a low pressure region in their base. Pylons reduce pressure losses associated with ramps due to their smaller physical size. Numerical and experimental research found optimal pylon geometries for fuel mixing and lower pressure losses.⁶⁻⁸ Combining these injectors with appropriate flame holder designs may offer beneficial scramjet combustor configurations. Recent work using state-of-the-art non-intrusive visualization techniques of pylon-aided injection upstream of a cavity flame holder indicate increases in penetration and mixing potential compared to transverse injection alone.⁵ However, this field of study is mostly untouched and requires further research for verification.

3. Experimental Methods

3.1. Test Facility

3.1.1. Wind Tunnel

The facility used in these experiments is the Supersonic Combustion Facility of the Air Force Research Laboratory, Propulsion Directorate (AFRL/PR). The wind tunnel is designed to allow basic studies of principles governing supersonic mixing and combustion processes using conventional and non-intrusive diagnostic techniques. A continuous supply of clean, compressed air is available to provide stagnation conditions up to 1660°R and 400 psia and a total maximum flow rate of 34 lbm/s. Compressors and a gas-fired heat exchanger supplies air at required conditions. An immense exhaust system allows for smooth starting and operation. The wind tunnel is made up of five major components: the inlet, settling chamber, nozzle, test section and diffuser. A schematic of the facility is provided in Figure 6, and all descriptions are taken from the chief designers of the facility, Gruber and Nejad.⁴⁰ Note that the end-viewing window is no longer available.

The purpose of the inlet section is to provide air for the tunnel from the main supply manifold. A hot and cold line, supplying 17 lbm/sec of 750 psig air at temperatures of 1660°R and ambient, are used in tandem to obtain desired stagnation conditions. The entire inlet section, consisting of four pieces: an upper and lower manifold, block valve and expansion section, is mounted onto support carts which roll on rails allowing for thermal

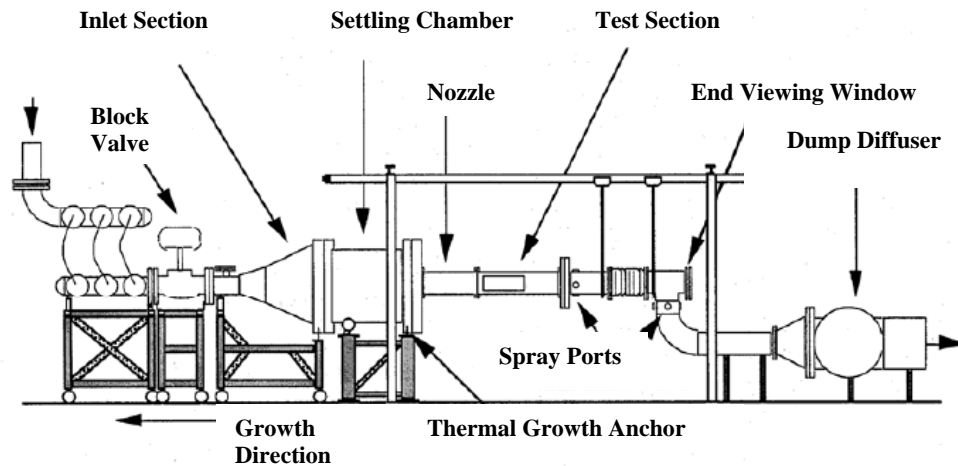


Figure 6. Supersonic combustion facility schematic⁴⁰

growth in the upstream direction. The Masoneilan[®] block valve, when closed, diverts the continuously supplied air through an exhaust valve and muffled vent line when the tunnel is idling. This allows specific run conditions to be maintained while modifications are being made to test section hardware. When the block valve opens, flow can be evenly distributed into the settling chamber by a rearward-facing cone expansion section.

The settling chamber conditions the flow using an array of coarse and fine mesh screens along with a honeycomb section to break up large-scale turbulence and align the flow before it is accelerated by the converging-diverging nozzle section. The chamber is capable of withstanding pressures up to 400 psig and temperatures up to 1660°R. Pressure and temperature measurements provide the approximate stagnation conditions within the chamber. To avoid vortex shedding at corners, the flow is geometrically transitioned before it leaves the axisymmetric settling chamber and enters the two-dimensional nozzle.

The planar converging-diverging nozzles used by the tunnel are designed using the method of characteristics with corrections to account for boundary layer growth. Several nozzles are available to provide Mach numbers from 2 to 4.5. The nozzle used for this experiment expands the flow to a Mach number of 2.0 at the test section entrance.

A constant area isolator 7 inches in length begins immediately after the nozzle's 2 inch high by 6 inch wide exit. The isolator is followed by a 30 inch divergent floor ramp with a 2.5° slope. The entire test section, shown in Figure 7 (flow is from right to left), is

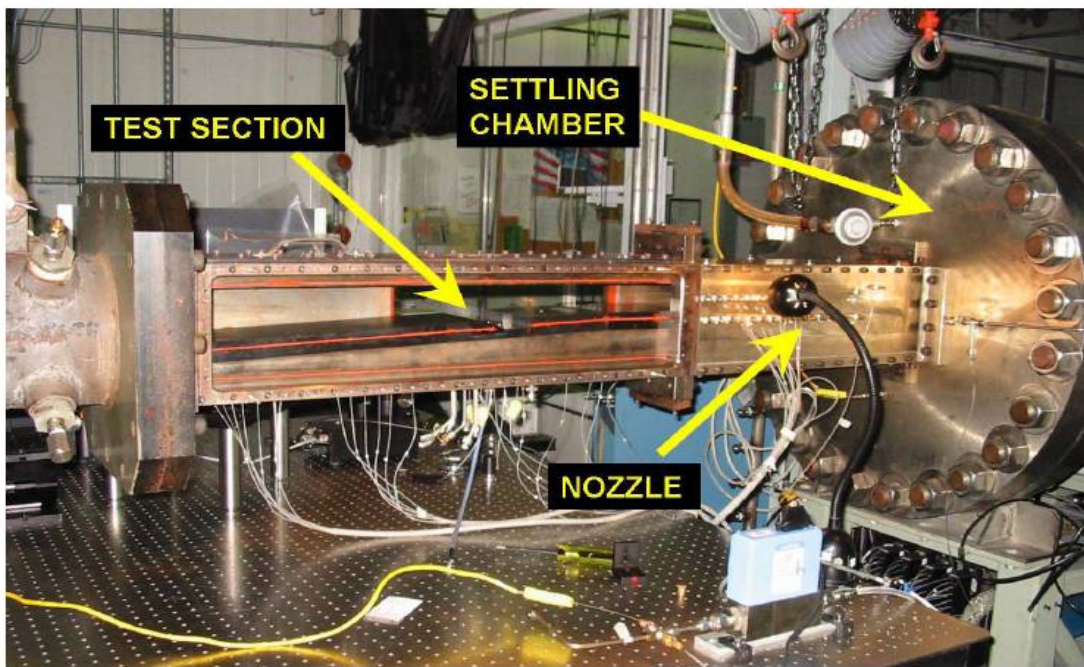


Figure 7. Profile view of tunnel midsection.⁵

completely visible through fused silica windows, with material properties excellent for transmission of ultraviolet wavelengths used in common non-intrusive diagnostics (such as Raman scattering). Two windows mounted on either side wall enables full viewing of the

transverse direction. Approximately 3 inches of spanwise viewing is available through a single window mounted on the top wall. Various hardware modifications can be made to the test section floor through various test inserts. All inserts are installed into the test section frame using standard bolt fittings and sealed with silicon o-ring chord. Both the cavity, described in section 3.1.2 and the pylon inserts described in section 3.2 are designed to be incorporated within the test section.

The tunnel axis system used in the research is based upon the test section setup. The positive streamwise (x) coordinate is aligned with the direction of the air flow. The positive transverse (y) coordinate is the upward direction, and positive spanwise (z) can be visualized perpendicular to the left of the air flow referenced as if looking upstream, in accordance with the right-hand rule.

Before the air exits through the exhaust line out to the facility air coolers, it passes through the diffuser section. Its role is to slow and cool the flow to required levels using a water injected dump diffuser design. The pressure and temperature within the diffuser is monitored by a series of transducers and type-K thermocouples.

3.1.2. Test Section Cavity

A modular cavity is mounted flush within the first 12 inches of the divergent test section floor. The cavity design accommodates various injection and combustion schemes. A close up view of the cavity is shown in Figure 8. Figure 9 gives a simplified profile

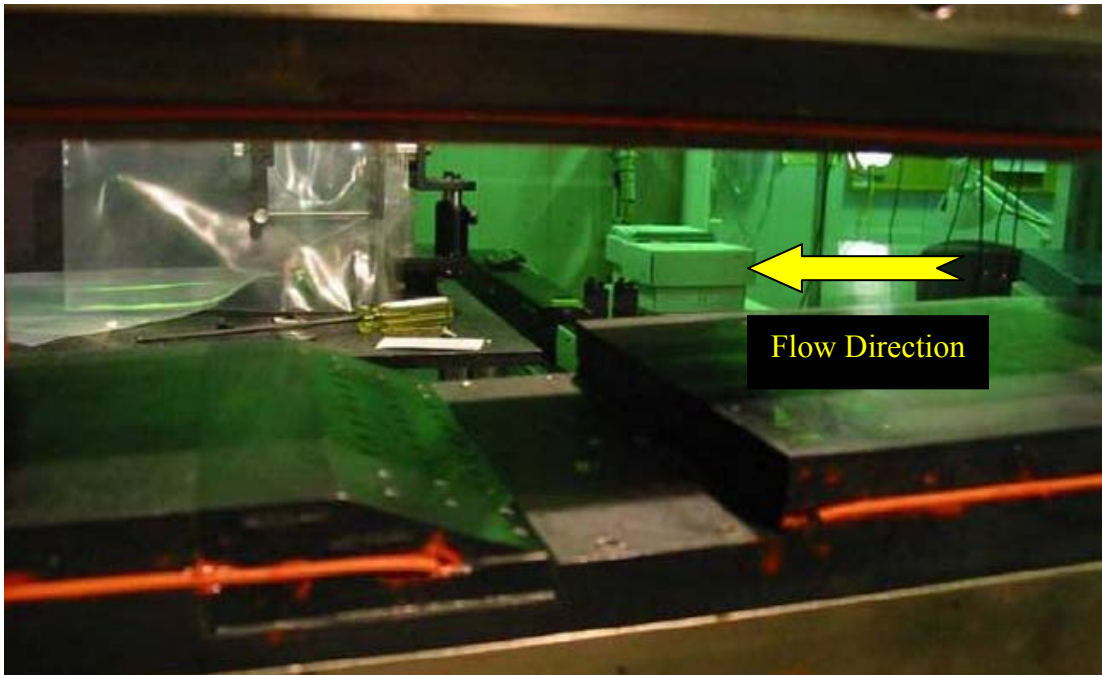


Figure 8. Closeup profile view of test section cavity⁵

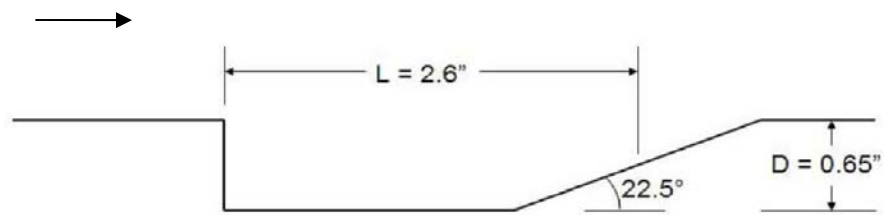


Figure 9. Simplified schematic of cavity⁵

schematic of the cavity, with flow from left to right. Notice the rear ramp fuel injection ports and spark plugs which are not used for this experiment. As seen in the figure, the cavity spans the entire width of the tunnel test section, and is recessed from the surface by a 90° backward-facing step to a depth (D) of 0.65 inches followed by a 22.5° trailing edge ramp. The total cavity length (L) is 2.6 inches producing an aspect ratio (L/D) of 4.0.

3.1.3. Fuel Injection

The ethylene gas injection is controlled through analog valves and digital flow controllers. An injectant supply line provides repeatable jet pressure conditions at the jet exit. A gas manifold is used to control the bottle pressure and connect several pressurized gas cylinders, where the ethylene is stored. The gas is provided from the cylinders by a Tylan[®] 2925 series mass flowmeter and monitored by a Tylan[®] RO-28 controller. An in house computer program is used to oversee the mass and volumetric flow rates of the injectant. Jet stagnation pressure and temperature is monitored using a series of pressure transducers and thermocouples.

3.2. Pylons

The four injection hardware inserts used are of previous design.⁵ Three inserts utilized various pylon geometries upstream of the injection port while the fourth insert is flat (no pylon). The three pylons' optimal heights, widths and distances from the injection port are determined from previous computational methods⁶ and correlated to sizes used in prior experimentation.^{7,8} Designs are determined from the top two configurations which

show enhancement of fuel penetration. Pylon wedge angle is determined from injection studies.⁵ Further detail into the design and manufacturing of the pylons used in this experiment are given elsewhere.⁵ Each insert is given a designator based upon its geometry. The no pylon case is referenced as the baseline configuration, while the three pylon inserts are described as the medium, tall and wide configurations. Each of the three pylon inserts contains a circular 1/16th inch injection port and the pylon at a set distance upstream from the port. The distance between the port and pylon is based on the pylon's size.

A schematic of the pylon and injector port design used in this research is given in Figure 10. Notice that the streamwise (x), transverse (y) and spanwise (z) coordinates are given in the figure, with origin at the center of the injection port at the surface. The pylon geometry is characterized by the length (l), height (h), width (W). The wedge angle (θ) is derived from l and h . As noted above, the injection port diameter, d , is constant at 1/16th

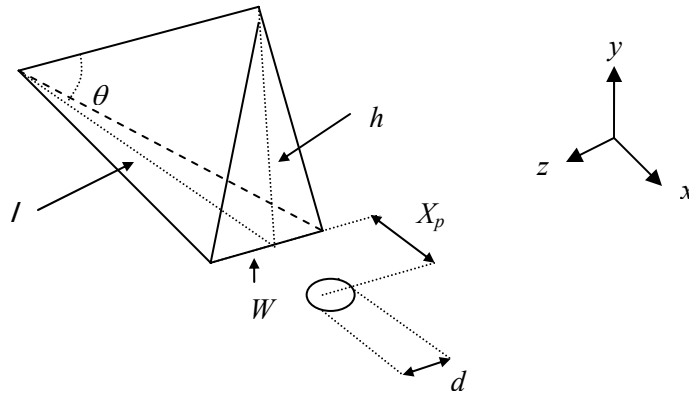


Figure 10. Pylon and injection port geometry⁵

inches. The axial distance between the pylon's trailing edge and the port's spanwise centerline, X_p , is defined as the *injection proximity*.

The numerical study focused on the pylon's width and proximity to the port. It found that the optimum value for X_p/d and W/d are approximately 2.0 and 1.0 respectively. The second most optimum configuration is deemed to have values for X_p/d and W/d of about 3.0 and 1.5. The injection studies determined that the ideal value for X_p/W is approximately 2.0 with an optimum wedge angle of 30°. The medium and tall pylon configurations are based on the optimum geometry found in the numerical study, the tall pylon is simply scaled due to a larger height. The wide pylon's geometry is based on the second optimal case determined from the numerical study. All pylons meet the criteria for optimum X_p/W and wedge angle from the injection study. Pylon height is the only independent geometry variable specified. The medium and wide pylons both had a height of 0.25 inches ($1/8^{\text{th}}$ the height of the test section) while the tall pylon's height was 0.375 inches ($3/16^{\text{th}}$ the height of the test section). Pylon geometry is summarized in Table 1 below. The four hardware inserts are designed to be flush mounted and aligned within the test section base plate. Figure 11 compares each pylon insert used in the research. Note the injectant feed line attachment for each insert. The similar wedge angle between the pylons is seen. The wide and medium pylons are not readily distinguishable from the profile view due to their similar length and heights; however, the tall pylon's larger size is clearly noticeable. Once installed, the injector port for each configuration is located approximately 0.35 inches upstream of the cavity's leading edge. Figure 12 gives a schematic of the installed pylon and cavity configuration, flow direction is indicated.

Table 1. Geometries for medium, tall and wide pylons⁵

		Medium	Tall	Wide
Height, h	(in)	0.25	0.375	0.25
Length, l	(in)	0.43	0.65	0.43
Width, W	(in)	0.07	0.07	0.1
Proximity, X_p	(in)	0.14	0.14	0.2
Wedge Angle, θ	(deg)	30.2	30	30.2
h/d	(-)	4	6	4
W/d	(-)	1.12	1.12	1.6
X_p/d	(-)	2.24	2.24	3.2

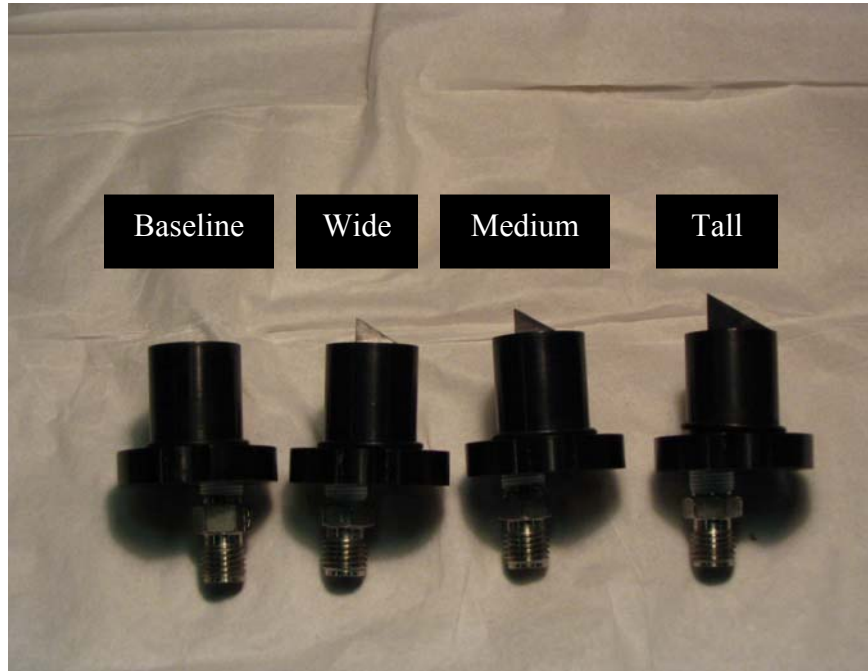


Figure 11. Pylon inserts used in research

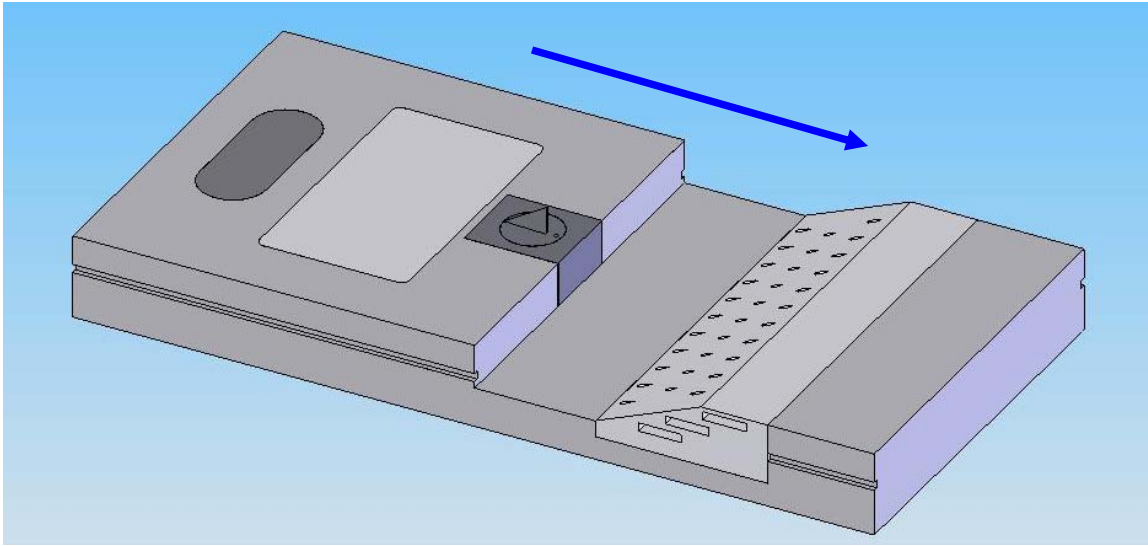


Figure 12. Pylon location relative to the cavity⁵

3.3. *Dynamic Pressure Ratio*

Gaseous ethylene (C_2H_4) was injected through the $1/16^{\text{th}}$ inch choked, circular injection port for all test conditions. Two different injection total pressures are selected based upon the highest and lowest injection total pressure conditions used during previous research.⁵ This allows for comparison between a higher momentum jet with strong penetration and vortex pair characteristics to a lower momentum jet which diffuses quicker out into the freestream. Every insert configuration is then tested with injection total pressures of 50 and 200 psia.

It is important to characterize the injection characteristics in a fuel mixing study. Typically, this is done using the non-dimensional dynamic pressure ratio, \bar{q} also known as the *jet-to-freestream momentum flux ratio*. This variable is defined by:

$$\bar{q} = \frac{(\rho u^2)_j}{(\rho u^2)_\infty} = \frac{(\gamma P M^2)_j}{(\gamma P M^2)_\infty} \quad (1)$$

where subscript j indicates *jet properties at the injection port exit* and γ is defined as the *ratio of specific heats* and varies dependent upon flow conditions and species. Many important mixing characteristics have been found to depend upon \bar{q} .³²

Freestream conditions are known from upstream plenum measurements and the flow is assumed to consist of air at $\gamma = 1.4$. At the jet exit, where the flow is choked, the Mach number is known to be unity. While the true value of P_j is unknown, an estimate can be made based on the adiabatic relations given below:

$$\frac{P}{P_t} = \left(1 + \frac{\gamma-1}{2} M^2 \right)^{-\frac{\gamma}{\gamma-1}} \quad (2)$$

and

$$\frac{T}{T_t} = \left(1 + \frac{\gamma-1}{2} M^2 \right)^{-1} \quad (3)$$

Using the above relations, values for the static temperature and pressure can be obtained from the measured total jet temperature and pressure and the jet's γ . Values for γ vary with species but also with temperature and pressure, properties which in turn depend on γ to be calculated. Using exhaustive databases such as the National Institute of Standards' (NIST) webbook⁴¹, the thermophysical properties of given fluids can be looked up for given conditions. An iterative process may be used by making an initial guess for γ , solving for P and T using the isentropic relations then finding the corresponding γ value for comparison to the original guess. Little difference in the overall value for \bar{q} is seen when applying an iterative method versus assuming γ to be at standard conditions.

For these experiments, values for \bar{q} are approximately 1.0 for an injection total pressure of 50 psia, and 4.0 for an injection total pressure of 200 psia. Comparison of \bar{q} calculated in previous research⁵ using nitrogen (of similar molecular weight to ethylene) showed similar match in values. Therefore, this non-dimensional variable is used to define injection pressure throughout the entire report.

3.4. Testing Strategy

3.4.1. Overview

Tests are conducted with a main flow Mach number of 2.0. Freestream conditions are set for a total pressure of 50 psia and an average total temperature of 550° R. Total temperature could not be explicitly controlled and varied with atmospheric. These values produce a freestream Reynolds number of 7.70×10^6 per foot, indicating a turbulent boundary layer at the injection station. Table 2 lists the freestream flow conditions at the nozzle exit. Note that since the test section expands at a given angle, the Mach number accelerates to approximately 2.1.

Table 2. Summary of freestream flow conditions at nozzle exit

M_∞	2.0	-
$P_{t,\infty}$	50	psia
$T_{t,\infty}$	550	°R
P_∞	6.39	psia
T_∞	306	°R
a_∞	857	ft/sec
U_∞	1714	ft/sec
ρ_∞	0.056	lb/ft ³
γ_∞	1.4	-
\dot{m}_∞	8.0	lb/sec

As mentioned in previous sections, two injection total pressures are used. During testing, measurements of injection total pressure and total temperature are monitored. Total temperature cannot be controlled freely and is an ambient condition. The average total temperature for both injection pressures is 516° R. The 1/16th inch injection port is choked for both injection pressures creating a jet Mach number of 1.0. Table 3 summarizes the conditions at the ethylene jet exit.

Table 3. Summary of jet conditions at injection port exit

	$\bar{q} = 1.0$	$\bar{q} = 4.0$	
M_j	1.0	1.0	-
$P_{t,j}$	50	200	psia
$T_{t,j}$	516	516	°R
P_j	27.3	106	psia
T_j	451	433	°R
a_j	1014	939	ft/sec
U_j	1014	939	ft/sec
ρ_j	0.162	0.702	lb/ft ³
γ_j	1.29	1.38	-
\dot{m}_j	3.5×10^{-3}	1.4×10^{-2}	lb/sec

3.4.2. *Test Matrix*

As mentioned previously, a right-handed, Cartesian coordinate system is chosen based upon the test section geometry. The origin of the system is on the test section floor at the center of the injection port along the tunnel centerline. The positive x -axis is in the freestream direction, the positive y -axis is in the positive vertical direction, and the positive z -axis is perpendicular to the flow toward the left side wall if facing upstream. For complete analysis of a supersonic flow field, four measurements are required; these measurements can be partitioned into two categories. The first category is species composition sampling, performed using the non-intrusive Raman spectroscopy technique. The second category is aerothermodynamic probing, performed using conventional pitot pressure, cone-static pressure and total temperature probes. To characterize the mixing associated with the cavity combustor, all eight configurations (four inserts at two injection pressures) are measured at axial locations over the cavity. Comparison of all configurations is performed at an x of 0.75, the approximate location of the spark plug within the cavity. It is shown in previous research that the wide pylon demonstrates the best improvement in mixing potential compared to baseline⁵, therefore multiple axial stations for species measurement are taken for the baseline and wide inserts to allow comparison. For the species composition sampling, all data is taken for the baseline and wide configurations at an axial distance of 0.45, 0.75 and 1.85 inches. The medium and tall pylons' species compositions are measured at an axial distance of 0.75 inches. For the aerothermodynamic probing, all the measurements are taken at an axial location of 0.75 inches.

At each axial station, a test mesh perpendicular to the flow is established for the species sampling and probe measurements, with test grid ranges of $-0.125 \leq y \leq 1.0$ inches and $-0.5 \leq z \leq 0.5$ inches. The techniques in both measurement categories allow different test mesh resolution. Charged Couple Device (CCD) camera resolution and laser beam width forms the basis of species sampling grid refinement. This allows for a spatial resolution of 0.04 inches in the y direction and 0.011 inches in the z direction. For the aerothermodynamic probing, the resolution is based on the diameter of the probes and is 0.125 inches in both the y and z direction. This yields a total of 3712 data points for the species composition sampling and 90 data points for each of the probing measurements. The test meshes for both the species sampling and aerothermodynamic probing is presented in Appendix A.

Finally, shadowgraph profile images are taken of the region of interest to allow orientation and illustration of the flow's physical features. Shadowgraphs are taken with and without fuel injection. Additionally, images of no flow conditions are taken for subtraction of background distortion. The images encompass a region from $-0.63 \leq x \leq 1.56$ inches and $-0.25 \leq y \leq 1.63$ inches.

3.5. Species Composition Sampling

3.5.1. Overview

Species composition measurements are required to fully understand and describe a supersonic flow with foreign gas injection. It is known that flow parameters such as Mach

number and total pressure in a mixed gas environment are functions of the ratio of specific heats (γ).⁴² The ratio of specific heats is defined below:

$$\gamma = \frac{c_p}{c_v} \quad (4)$$

where c_p and c_v are the *specific heats at constant volume and constant pressure*. For a gas of single species, calculation of the specific heats is based upon the conditions of the medium. However, for a mixture of gases, such as air and ethylene, each species have different specific heats. The following equation must be used to determine the specific heats of a mixture:

$$c_{p,mixture} = \sum X_i * c_{p,i} \quad (5)$$

and

$$c_{v,mixture} = \sum X_i * c_{v,i} \quad (6)$$

where X_i is the *mole fraction* of species i . Additionally, mixing analysis requires knowledge of local species concentration which can only be done through species composition sampling.

Species composition sampling is performed using a non-intrusive laser induced spontaneous Raman spectroscopy method. Raman spectroscopy takes advantage of the Raman scattering phenomenon that occurs when photons of light interact with individual molecules. The method is commonly used for determination of species in both cold and reacting flows. A brief overview of the process is presented in the following section.

3.5.2. Principle of Operation

Raman scattering can be considered an instantaneous (occurring within a time of 10^{-12} seconds or less) inelastic collision of an incident photon, (\hbar_i) with a molecule (\mathcal{M}) both at different discrete energy levels.⁴³ An inelastic process occurs when there is an exchange of energy occurring between \hbar_i and \mathcal{M} , emitting scattered light shifted from its original frequency.⁴⁴ This energy exchange can be termed rotational, vibrational or electronic based upon the nature of the collision. Typically the energy exchange is related to the dipole moment (\mathcal{P}) of \mathcal{M} .^{43,44,45} The definition of a dipole moment is given below.

Consider a time fluctuating electric field of strength E from an incident wave as shown in the equation below:

$$E = E_o \cos(2\pi\nu_o t) \quad (7)$$

where E_o is the *vibrational amplitude* and ν_o is the *wave frequency*.⁴⁵ The wave, irradiating a molecule, causes an induced electric dipole moment. An electric dipole is basically a separation of equal but opposite charges within an atom or molecule caused by the presence of an electric field.⁴⁴ The electric field causes polarization in the direction of the field which arises from the displacement of the electron cloud from the nucleus of the molecule or atom as shown in Figure 13. The dipole moment then can be described by the equation below:

$$\mathcal{P} = \alpha E \quad (8)$$

combining with equation 7:

$$\mathcal{P} = \alpha E_o \cos(2\pi\nu_o t) \quad (9)$$

where α is defined as *polarizability* which is a proportionality constant.⁴⁵ For molecules vibrating with frequency ν_m (which are of interest to this study), the polarizability can be

expanded as the summation of a static term and q which relates the nuclear displacement caused by the polarization and shown below in equation 10.^{43,44,45}

$$\alpha = \alpha_o + \left(\frac{\partial \alpha}{\partial q} \right)_o q \quad (10)$$

where:

$$q = q_o \cos 2\pi \nu_m t \quad (11)$$

therefore, combining equation 9 with equations 10 and 11 and using trigonometric identities to obtain the electric dipole moment split gives:^{43,44,45}

$$\begin{aligned} \mathcal{P} = & \alpha_o E_o \cos(2\pi \nu_o t) \\ & + \frac{1}{2} \left(\frac{\partial \alpha}{\partial q} \right)_o q_o E_o \left[\cos \{ 2\pi (\nu_o + \nu_m) t \} + \cos \{ 2\pi (\nu_o - \nu_m) t \} \right] \end{aligned} \quad (12)$$

The induced dipole moment defined above oscillates, thereby creating new waves generated by the molecule, \mathcal{N} .⁴³ The first term, leading to elastically scattered waves at the frequency of ν_o , is called the Rayleigh process and is not species specific. In the second term, the scattered waves are specific to the vibrational frequency of the molecule; the frequency of such scattering is “shifted” from that of the incident by characteristic frequency of the molecule.⁴⁴ That change in frequency is termed the Raman shift. For a medium with a mixture of gases, each constituent at a given initial energy level will then produce a certain amount of Raman scattered waves at an intensity dependent on its number density N_i .⁴³ Waves at frequency $\nu_o - \nu_m$ are described

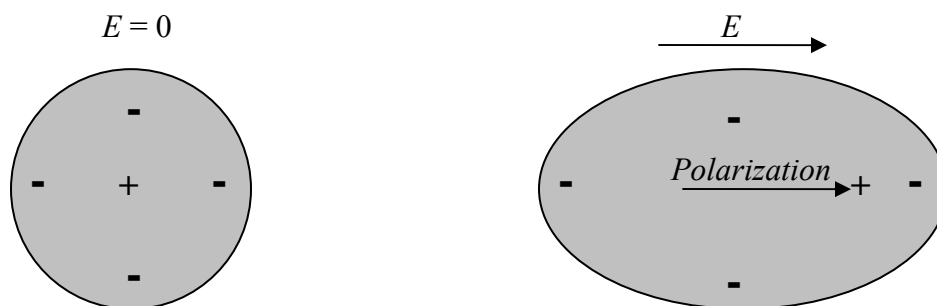


Figure 13. Polarization of a molecule induced by an electric field⁴⁴

historically as the Stokes component while waves at $\nu_o + \nu_m$ are termed the anti-Stokes component.⁴³ It must be noted that while frequencies predicted by this classical approach are correct, the intensities are not and require a more thorough quantum analysis as given by Demtröder.⁴³ Radiation in the Stokes component allows the initial energy state of molecules to be in the vibrational ground state, while molecules must have an initial excitation for emission of the anti-Stokes component.⁴³ For this reason, the Stokes component has a higher population density and its waves are usually measured.⁴⁵ This scattered light can be collected and the intensities separated according to frequency using a spectrometer (see following paragraph). The separated light intensities may be related to the number density of the gas. This process is presented in section 4.2.2. The intensity of the Raman scattering is very low, with intensities below 10^{-10} that of the incident beam. Therefore to ensure adequate signal strength, a strong incident beam is used, specifically lasers.⁴⁵

Spectrometers are optical instruments which form images of incident radiation from an entrance slit which is laterally separated for different wavelengths.⁴³ This dispersion of radiation is achieved through either a prism or a so-called diffraction grating. In laboratory

settings, diffraction gratings are more common.⁴³ The device employed here is based on a diffraction grating. The basic premise is that the incident light upon entering the spectrometer is reflected onto a grating which consists of small grooves parallel to the entrance slit. The grating is covered in a reflective layer and the light is reflected from the grating onto a radiation detector (i.e. a photomultiplier tube, photographic plate, or a digital camera). A zoomed-in illustration of a grating is shown below in Figure 14. Light incident to the grating at angle δ_i is reflected at an angle δ_r . This reflected angle is related to the incident angle, the distance between grooves on the grating and the wavelength of the incident light by the grating equation given below:

$$s_{grat}(\sin \delta_i - \sin \delta_r) = m\lambda \quad (13)$$

s_{grat} is the *groove spacing*, λ is the *incident wavelength* and m is the *diffraction order* which depends upon grating design. Thus according to the above equation, radiation will be reflected from the grating at an angle dependent upon its wavelength; for the Raman scattering application, this wavelength is the Stokes component of the Raman shift.

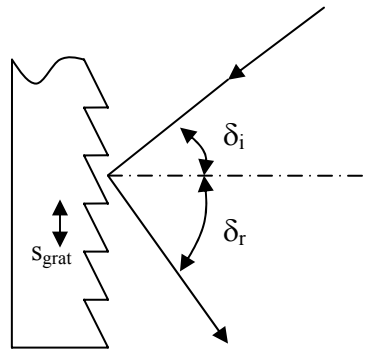


Figure 14. Radiation incident upon a diffraction grating⁴³

In Raman spectroscopy, the region of interest is irradiated by a laser beam, and the scattering is observed perpendicular to the beam. An illustration of a basic experimental arrangement for Raman scattering is shown in Figure 15. The area of interest is the focal region of the focusing lenses. The resulting scattering, is imaged onto the spectrometer entrance slit, and the light intensity is split into a Raman spectrum. As an example, Figure 16 gives a generic Raman spectrum (typically expressed as a plot of intensity versus Raman shift) for a medium with two species. The illustration above shows the layout for a point measurement; however, one can generally arrange the optics to image a portion of the laser beam path, thereby allowing a 1-D measurement of species concentrations along the beam path. This requires that the beam image be focused along the length axis of the entrance slit and that a 2-D imaging system be used for detecting the scattered radiation. For this experiment, a continuous wave (CW) laser is employed and time-average concentrations (over the sampling time) are derived. Pulsed lasers have also been used for instantaneous concentration measurements. These lasers can generate pulses with very high peak irradiances (W/cm^2). If the irradiance is too high, a phenomenon called dielectric breakdown occurs. During dielectric breakdown spontaneous plasma forms near the point of the laser focus⁴⁶, generally limiting the pulse energy that can be used for Raman scattering.

The Raman shift is commonly measured in wavenumber, $\tilde{\nu}$, defined as the inverse of wavelength (units of cm^{-1}), and an example spectrum is shown in Figure 16. For two species to be resolved, it is critical that the dispersion of the spectrometer (typically determined by the focal length of the spectrometer plus the grating's groove density) be

great enough. Clearly species A and B are separated by a sufficient distance along the detector plane that they can be distinguished and their concentrations quantified.

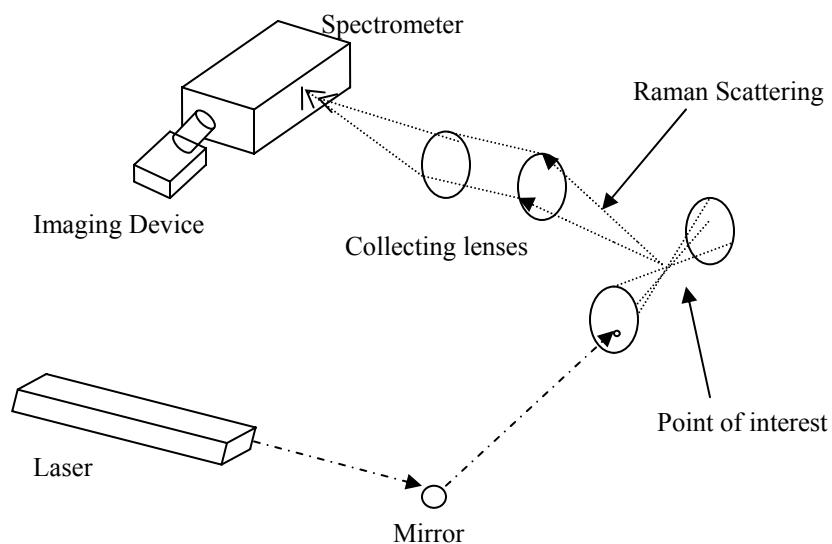


Figure 15. Schematic of single point Raman experiment setup⁴⁴

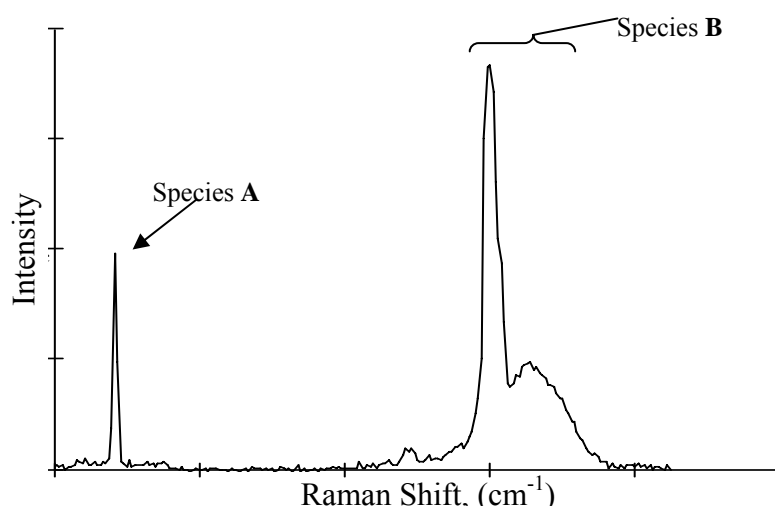


Figure 16. Example single point Stokes Raman spectrum in bi-species medium

3.5.3. Instrumentation

Instrumentation setup for the Raman spectroscopy is shown in Figure 17 and Figure 18, and a simple schematic is given in Figure 19. A Spectra-Physics® Millennia Pro continuous wave (CW) laser producing 8.5 Watts at 532 nm is used as an excitation source. The beam is passed through a half wave plate to rotate the polarization to the horizontal plane. The beam is then turned 90 degrees, perpendicular to the flow and passed through a 500 mm focusing lens and through the tunnel window. Focusing the beam perpendicular to the flow allows for one-dimensional measurements in the z -direction approximately 15 mm on

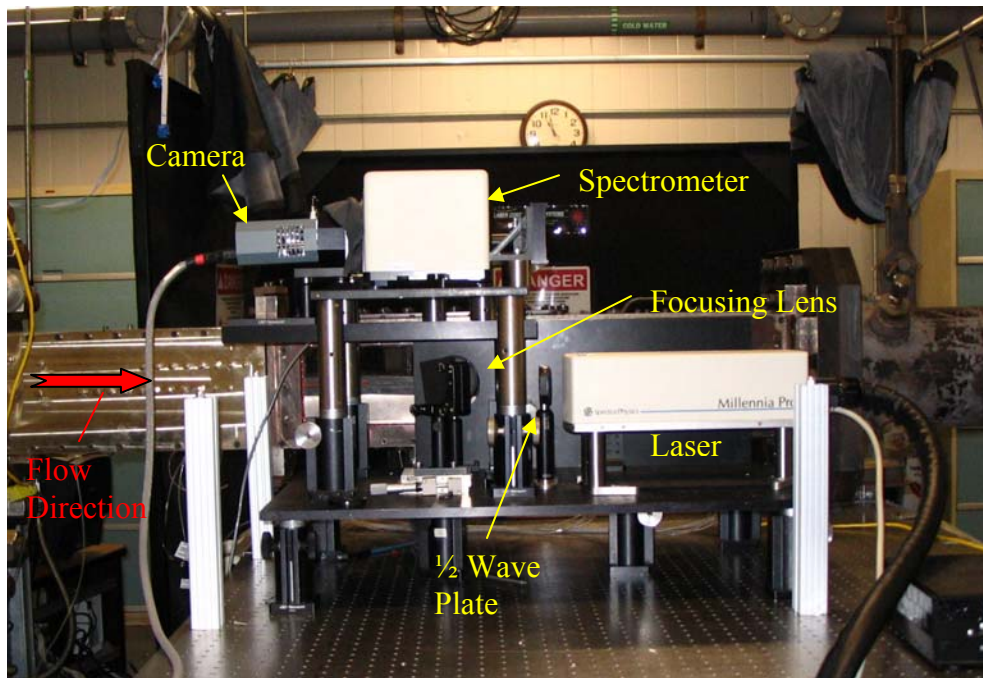


Figure 17. Left side-view of Raman spectroscopy setup

either side of tunnel centerline. Scattering is collected through the top tunnel window. The scattered light is reflected using a 3-inch diameter aluminum mirror; a Schott glass OG-590 long-pass filter is employed to block background scattering (at 532 nm). The radiation is

then focused by a 58-mm focal length Nikon® lens onto the entrance slit a Kaiser Holospec™ $f/1.8$ imaging spectrometer. A 35-mm diameter Uniblitz shutter was placed between the lens and the spectrometer. This shutter, which was controlled through the I/O port of the camera, is employed to define the sampling time of each measurement. The precision of the shutter is expected to be about 10-20 ms, less than or equal to 0.1% of the sampling time. The shutter system is supported by a Thor® ring plate. The focused light is then passed into a high resolution grating. The Raman scattering is detected by an Andor®

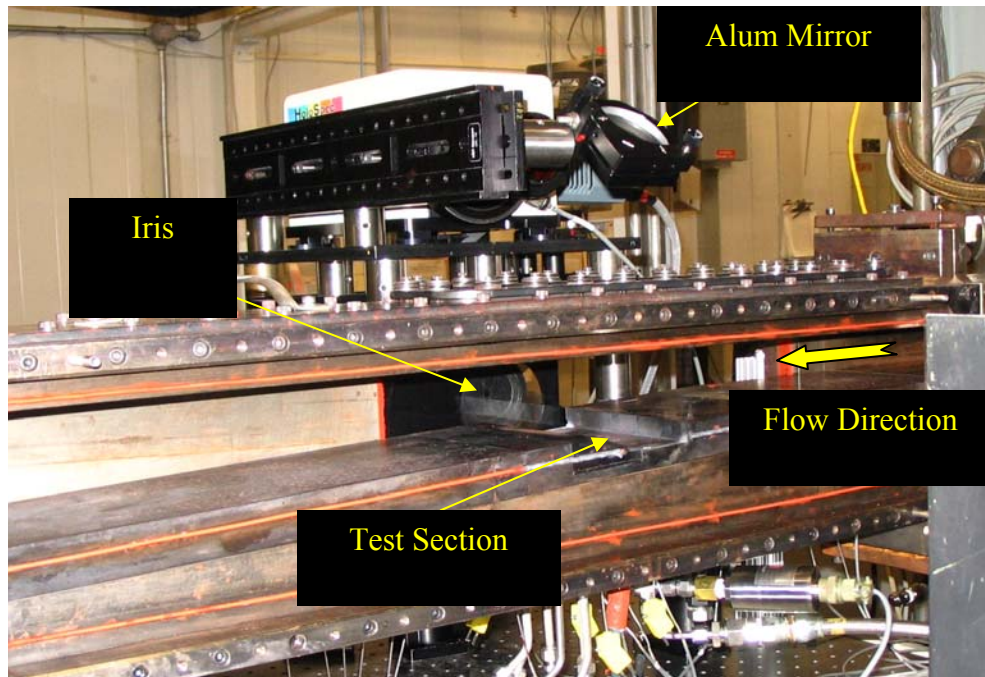


Figure 18. Skewed right-view of Raman spectroscopy setup

back-illuminated, thermo-electrically cooled spectroscopy CCD camera having a 2048 by 512 pixel array (each pixel 12.5 microns square). Pixels are binned into 4 by 4 groups prior to camera readout. The entire setup is placed on a two-axis traversing table with freedom of movement in the transverse and streamwise directions (tunnel x and y).

Andor's[®] image acquisition software is used to capture and record the digital images onto a computer. Through a 1-mm wide entrance slit, the scattering image (of the laser beam is much smaller than the slit width; the spectral resolution is largely determined by the binned pixel width (50 microns), which effectively acts as a spectrometer exit slit. Due to the selected grating, scattering only from nitrogen and ethylene signals is collected by the CCD camera (the vibrational Raman shift of oxygen scattering is 1556 cm^{-1} , much less than for nitrogen, at 2331 cm^{-1} , and ethylene, at 3020 cm^{-1}). The ratio of oxygen to nitrogen number density is constant at 1/3.76. This fraction is determined by assuming air is a mixture of 79% nitrogen and 21% oxygen (by volume). The nitrogen vibrational Raman line is about 1 to 2 binned pixels in width, while the ethylene's vibrational band is much broader (10 to 20 pinned pixels).

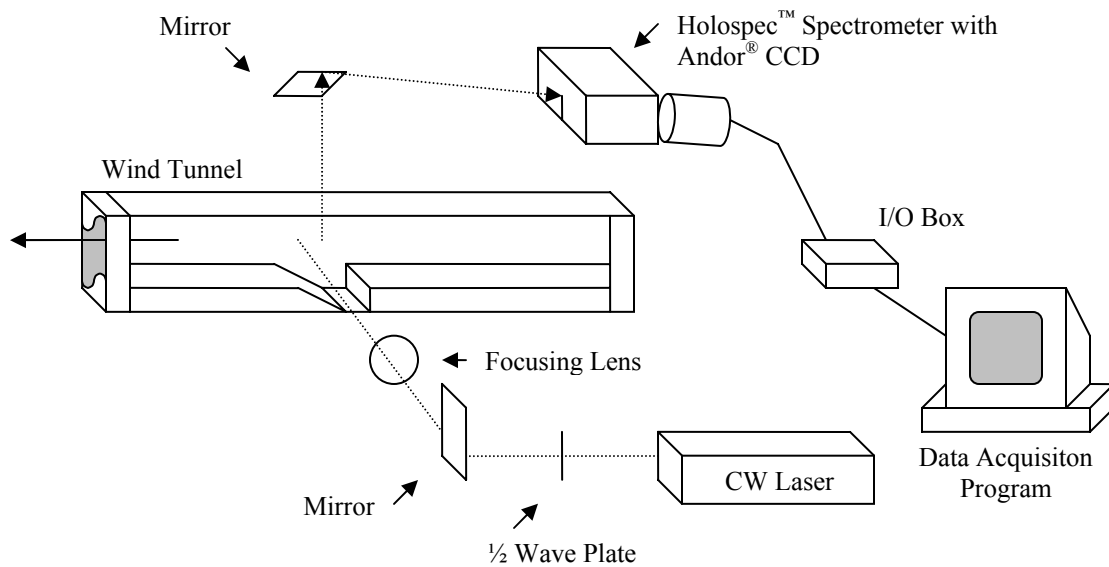


Figure 19. Schematic of planar Raman scattering setup used in experiment

The image acquisition is synchronized with the table movements so that collection of an entire plane of data is automated. Each 1-D measurement of the scattering is sampled for 20 seconds (controlled by the shutter). Afterwards, a signal is read by the traversing table movement software (while the image is being read out) and then the table translated to the next vertical sampling location.

3.5.4. Calibration

Calibration involved determining the camera field of view (that is length of space viewed by each pixel). The field of view is determined by imaging injection of ethylene from a small injection hole at various spanwise table positions. Sample images are shown in Figure 20a and b; in Figure 20b the translation table has been moved by 15.2 mm (in the spanwise direction) and the movement of the ethylene jet is clearly seen (while one can also see that the tunnel is filling with a small fraction of ethylene, evident from the small signal throughout the imaged region). To derive the imaged length per binned pixel, the location of peak signal is recorded and the traverse moves to a new location along its tunnel z axis. Note that the line image does show some curvature; this is a common imaging artifact for spectrometers. A linear correlation between the pixel location and the tunnel z axis is performed using a data reduction program. From this correlation a simple linear equation is used to obtain location along the tunnel z -axis. The linear correlation has a norm of residuals of 0.26 and is presented as:

$$z = 0.28 * pixel - 17 \quad (14)$$

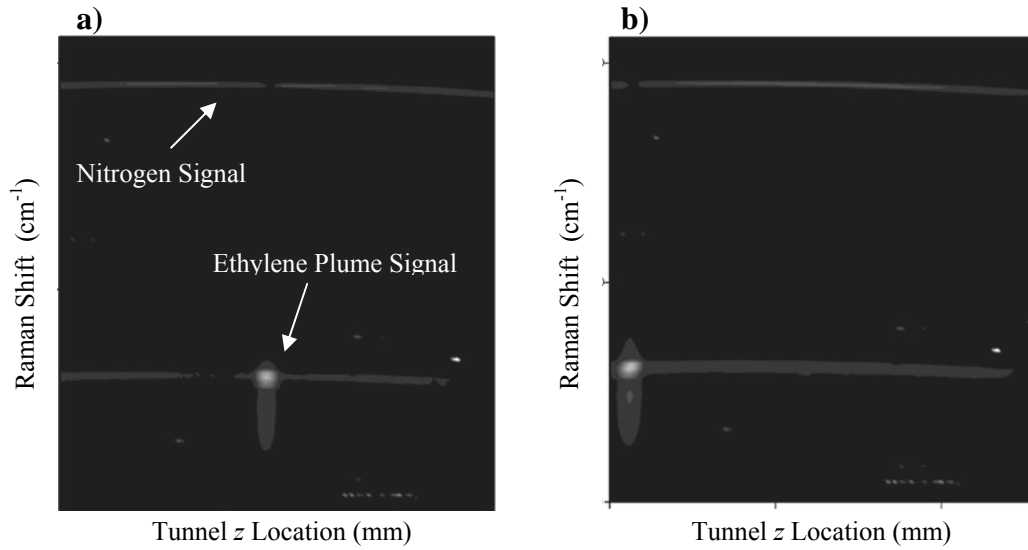


Figure 20. Calibration Raman scattering a) 0.0 mm and b) 15.2 mm from centerline

where *pixel* ranges from 0 to 128 and *z* is represented in millimeters. The norm of the residual is a measure of “goodness” of correlation fit. In this case it is the average difference between the correlation’s and the discrete data point’s values for *z*. The norm of the residual also affects the error in position measurements for the Raman method which is discussed in Appendix E.

3.6. *Aerothermodynamic Probing*

3.6.1. *Overview*

Three sets of conventional probes are used to examine the flow field at an axial location of 0.75 inches. Measurements are performed using a pitot, cone-static probe and total temperature probe with similar test meshes. All probes are approximately the same

length with similar circular capture areas of $3.9 \times 10^{-3} \text{ in}^2$ and are secured within identical 7.75 inch long and 1.0 inch wide diamond-wedge struts. The shape of the strut allows for low supersonic flow drag and flush installation through the side wall. The probes have a 90° bend at the end of the strut to bring the probe tip parallel to the main flow. The probe protrudes approximately 1.0 inches in front of the strut. In between the probe tip and the bend, a slight jog in the probe allow for near wall measurements. All probes are connected to a Parker® probe actuator system through a traversing wall plate as shown in Figure 21. The wall plate allows for probe movement in the transverse direction while the actuator moves the probe perpendicular to the flow along the spanwise axis. The traverse-actuator system allows for sampling in the entire desired range specified by the test mesh. Views of a typical probe setup are shown in Figure 22, the probe shown in the picture is the cone static (flow direction is indicated). The total temperature and pitot probes are shown in Figure 23.

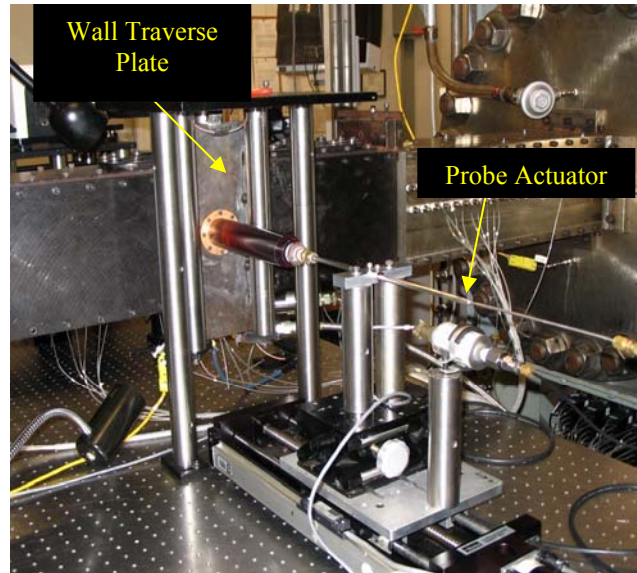


Figure 21. Probe actuator and wall traverse plate system

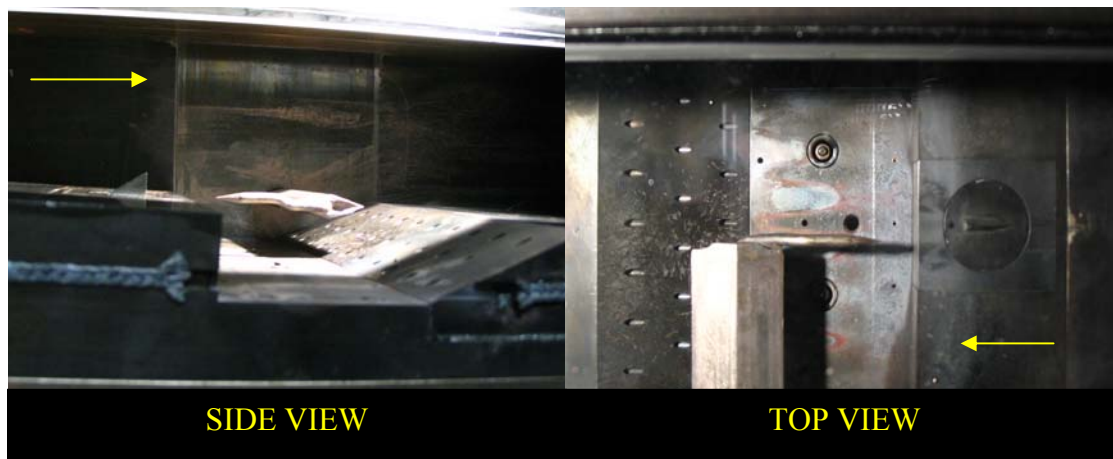


Figure 22. Side and top views of cone-static probe installed in tunnel

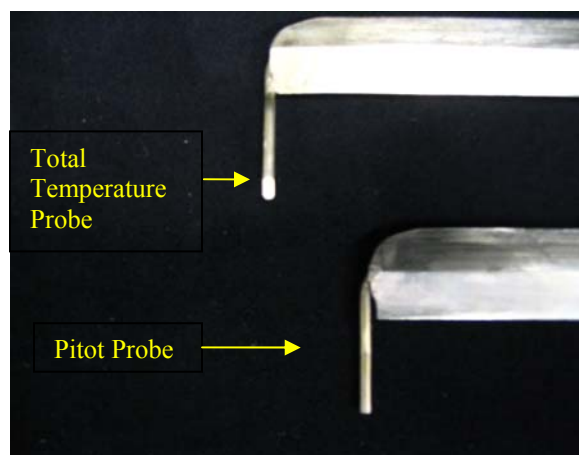


Figure 23. Total temperature and pitot probes used in experiment

3.6.2. *Pitot Pressure Probe*

The pitot probe used in this research is a simple open-ended tube (the open end is perpendicular to the flow; the other end is connected to a manometer). With the exception of very low Reynolds numbers (not the issue for the current research), the flow inside the tube is assumed to decelerate to rest isentropically, and therefore, the pressure sensed by the tube is the stagnation or total temperature at the mouth of the tube.⁴⁷ For supersonic flow, the indicated pitot pressure is not the local total pressure due to a detached shock wave standing ahead of the tube. Fuller⁴⁸ created a method (summarized in section 4.3) for determining the total pressure.

The pitot probe is designed in house to standard specifications. The pitot probes open end is well within the diameter limit of 1/5 inches to prevent local flow disturbance.⁴⁷ Plastic tubing ran the pneumatic measurement from the probe to a Sensotec[®] pressure transducer with a sensing range of 0 to 100 psia. The pressure transducer converts the sensed pressure from the manometer linearly to a corresponding analog voltage at approximately 50 mA. The voltage is then sent to a National Instruments[®] PCI-MIO-16XE, 16 bit data acquisition board where the signal is calibrated and fed digitally to the computer hard drive.

3.6.3. *Cone-Static Probe*

To measure the cone-static pressure in a supersonic flow, a long, slender probe with a cone tip is desirable to ensure minimum flow disturbance.⁴⁷ The cone-static probe consisted of a closed end tip with a conical half-angle of 10°. To prevent distortion from the nose's region of influence, four pressure ports are placed parallel to the spanwise and

transverse axis downstream of the tip at 90° angles from each other. To decrease sensitivity to yaw, all ports feed to a common manometer lead, and an average pressure is measured. Pressure measurements are made using the same instrumentation as the pitot probe.

3.6.4. Total Temperature Probe

Total temperature probes measure temperature similar to how pitot probes measure pressure. A simple opening perpendicular to the flow should bring the flow to rest in equilibrium and measure the resulting temperature.⁴⁷ However, due to heat conduction and radiation, equilibrium does not exist and the temperature sensed in the probe is lower than the actual temperature. For temperature probes, the recovery factor, r , becomes important. The recovery factor is defined as:

$$r = \frac{T_r - T_1}{T_0 - T_1} \quad (15)$$

where T_r is the *temperature sensed by the probe*, T_0 is the *actual stagnation temperature* and T_1 is the *static air temperature of the medium*.⁴⁷ For the present research total temperature measurements are made with a pitot design by Winkler⁴⁹ which obtains values of constant r nearly equal to 1 over a wide range of conditions.⁴⁷

The total temperature probe utilizes a standard type K thermocouple with an operating range of 6°R to 2961°R with approximate sensitivity of 0.039 mV/°C.⁵⁰ Thermocouple leads are attached to a 16 bit National Instruments® PCI-MIO-16XE data acquisition board and conditioned through a National Instruments® SCXI interface before being recorded onto the computer hard drive.

3.6.5. Calibration

The pressure probes are calibrated using a third-order least squares correlation between a known sensed pressure from a Ruska[®] precision calibration unit and the voltage output from the pressure transducer. Total temperature calibration is performed through a highly accurate standard look up table for a type-K thermocouple provided by National Instruments[®]. The lookup tables relate output voltage from the thermocouple to temperature.

3.7. Shadowgraph Photography

3.7.1. Principle of Operation

Shadowgraph is a visualization technique where flowfield physical properties are visible because of light ray deviations. These deviations are caused by the fact that the speed of light varies with a medium's density.⁴⁷ The ratio of the speed of light in a medium to the speed of light in a vacuum is the index of refraction. The shadowgraph is a simple imaging method which makes use of refractive index changes in a medium.⁵¹ Figure 24 gives a simple graphic illustrating the shadowgraph process. Parallel light entering a test section is deflected from its incident angle by changes in refractive index for density changes in the medium. The light is then captured on an illumination screen. However, if the density change in the medium is constant, then the deflection of the light is similar and will illuminate the screen in a uniform fashion. Flow features are only visible if the deflection of light varies relative to other light, not necessary an absolute deflection. Therefore, visualization occurs with a change in the density gradient of a medium (or

second spatial derivative of density).⁴⁷ If this is the case, the light will emerge from the test section at different angles relative to each other. On the screen, bright regions is where light crowd together and dark regions where light diverge.⁴⁷ Shock waves which result in a sudden drop in density appear as bands of high intensity followed by low intensity. Other features such as expansion fans and boundary layers which cause changes in density gradients appear as well. Since the area of interest is three-dimensional, the light may deflect multiple times. Therefore, any shadowgraph image created will be an integration of all features in the path of the light.

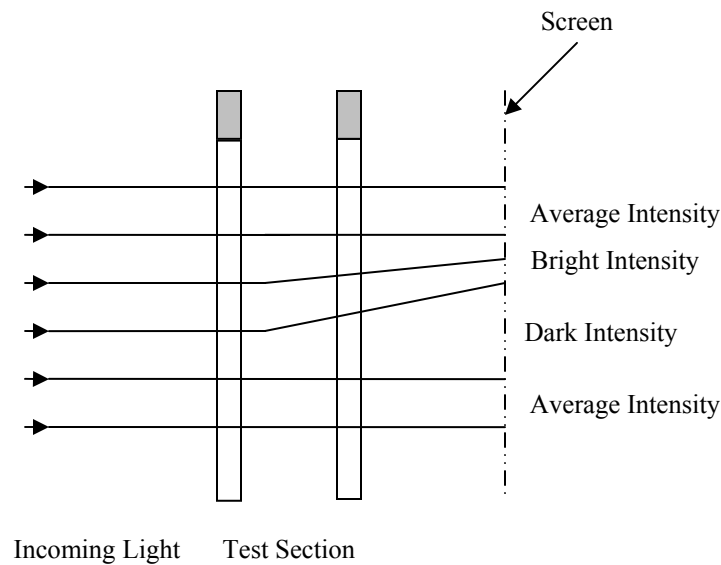


Figure 24. Illustration of a simple shadowgraph⁴⁷

3.7.2. Instrumentation

In the current research a point source of light from an Osram[®] 100 Watt mercury short arc lamp is reflected by a flat mirror and expanded by a J. Unertl concave reflector to collimate the light perpendicular to the main flow through the test section. Since the region

of interest is small in comparison to the size of the total test section, the light exiting the test section illuminated a target screen instead of being focused directly into a camera. Use of the target screen allows for a camera to focus with high resolution on the region of interest; however, this reduces the intensity. During testing, 11 separate shadowgraphs are taken of each configuration at similar exposure time to ensure that there are no time varying properties in the major flow structures. Figure 25 and Figure 26 show the setup used.

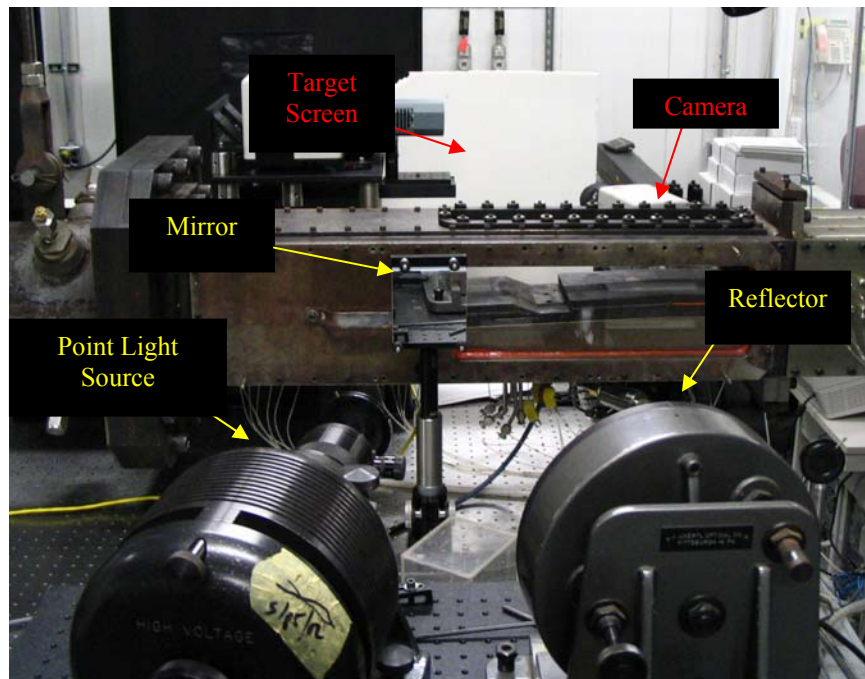


Figure 25. Profile view of shadowgraph setup, flow from right to left

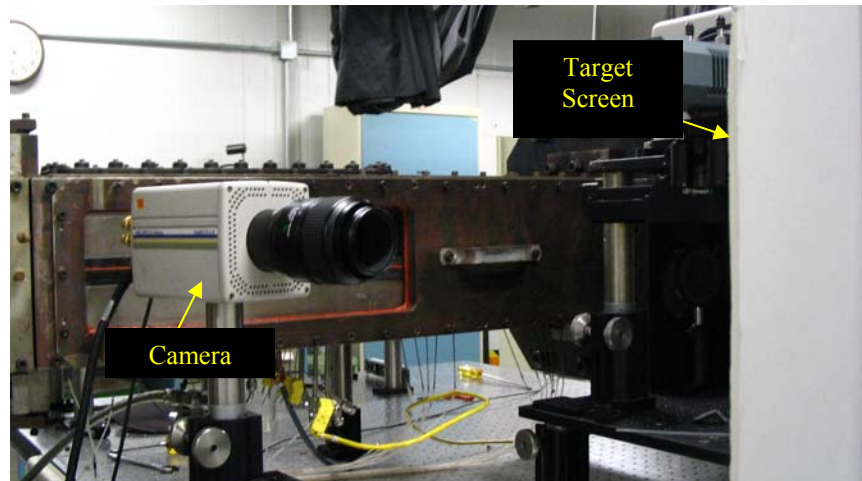


Figure 26. View of camera and target screen used in shadowgraph

3.8. Laboratory Procedure

3.8.1. Overview

Each of the eight inserts is tested in Mach 2 flow. Before testing began, the origin for the traverse mechanism is defined. Once the air flow from the main manifold is at proper testing conditions, it is allowed to enter the test section. The tunnel is then given time to reach steady conditions, and if fuel is being injected, the injection total pressure is set as required. Measurements are then made. Tunnel properties are displayed and recorded on the test facility's in house computerized monitoring system. If for any reason, the test section needed to be isolated for insert modifications or ethylene gas cylinder replacement, a vacuum is created. Any pylon modifications take approximately 15 minutes. It is deemed necessary to replace the gas cylinders when the indicated injection

total pressure fell and continued to fall below approximately 97% of the desired injection total pressure. Cylinder changes take anywhere from 5 to 20 minutes.

3.8.2. Species Composition

Before testing, the laser beam is set to safe intensity levels. Proper alignment with axial position is done by observing the beam off-angle. The traverse is then set to predetermined locations and the beam intensity turned up. Since the Raman method took data on a one-dimensional plane of the spanwise coordinate, the traverse only has to move in the y -direction to obtain the test mesh. Light control is extremely important for this optical process, and all unnecessary lighting in the facility is turned off. A dark covering is provided for the spectrometer assembly to ensure reduction of background lighting. The data acquisition procedure consists of setting tunnel and injection conditions, setting the traverse to its initial testing location and then obtaining the signal. A time-averaged signal is taken for 20 seconds and the traverse is moved to the next vertical position. After each signal is taken, data is stored onto the computer hard drive and the image is displayed for verification purposes using the image acquisition program. As the traverse is moved to each vertical location, the Raman scattering is seen and fuel concentration can be tracked. Once it is evident that no more fuel is being imaged, the fuel is shut off (typically at the last five vertical locations). Once the test mesh is complete, the traverse is returned to its starting position. The entire procedure takes signals at 29 separate vertical locations and lasts approximately 20 minutes per run. Injection pressure is then changed and the procedure is repeated. After data is obtained at the second injection pressure for the medium and tall pylons, the tunnel is isolated, the laser beam's intensity is tuned to a safe

level and the test section insert is changed. For the baseline and wide pylons, since multiple axial locations are being tested, the traverse is moved to the two other axial locations of 0.45 and 1.85 inches and the entire procedure is repeated. A total of 16 separate combinations of axial location, pylon and injection pressure are tested. Testing took two separate nights for an approximately four hours each night.

3.8.3. Aerothermodynamic Probing

The probes, connected to an actuator system from the diamond-wedge strut are allowed to move to each point in the test mesh. The probe locations in the test mesh are preprogrammed and automated. A camera system is utilized to allow viewing of the traverse and probe. A total of eight configurations are tested at a single axial location of 0.75 inches for each of the three probes. At the beginning of each test run, the probe tips are retracted to the traversing wall plate. The tunnel flow is brought to the desired conditions and fuel injection begins. The wall mount traverse begins at a y -location of 0.125 inches. The probe traverse then moves the probe to the first spanwise location and data is obtained. At each location, the probe allows the flow to reach steady state before averaging 1000 data samples over a half second time. Data is recorded after each measurement. The probe measures data at nine points along the spanwise coordinate at 0.125 inch intervals. Once the spanwise sweep is completed, the probe is retracted and the wall traverse moves to the next y -location and the process repeats. Once the entire mesh is measured, the probe retracts and the traverse moves back to the first vertical location. Injection pressure is changed and the entire procedure repeated. After the data mesh is probed for the second injection pressure, injection is shut off and the tunnel is brought to a

vacuum. Pylon inserts are changed and the testing continues. Each data mesh takes approximately five minutes to complete. A total of twenty four runs are conducted for the probes. Probing took approximately 5 hours to complete.

3.8.4. Shadowgraph

The shadowgraph procedure is relatively simple. Once the image capture area is deemed acceptable, all unnecessary background light is turned off. As mentioned previously, eleven time-averaged images are taken of each configuration to ensure similarity in flow field structures. For each insert, four sets of images are taken: one without injection in a vacuum, one without injection at freestream flow conditions, and two with injection at freestream flow conditions. The images are acquired and saved onto the computer hard drive. The eleven images obtained in each run are averaged. The averaged no injection vacuum shadowgraph is treated as a background image. This background image is subtracted off of the averaged no injection and injection flow images to increase clarity of flow structures and reduce undesirable imaging due to tunnel window distortion and camera noise.

4. Data Reduction

4.1. *Non-dimensionalization*

Non-dimensionalization is performed on all presented data. Fluid properties are non-dimensionalized by their freestream values (with the exception of injection pressure as covered in section 3.1.3). All length quantities are divided by the diameter of the injection port as is common practice in injection studies. Similarly, all area values are non-dimensionalized by the injection port area.

4.2. *Species Composition*

4.2.1. *Overview*

Determining the species concentration from the raw Raman spectrum is an extensive process. Discrete values of species concentration are found from relating pixel intensity on the image to actual number densities. The following sections outline the data reduction steps taken to convert the raw Raman spectrum images to actual number densities within the test mesh. All data reduction for species composition is performed in Mathsoft[®] Mathcad[™]. Since the reduction process involves images with distortion and background signal, it is important that objective, uniform correction procedures are applied to reducing the raw images obtained from the camera. These correction procedures are outlined in Appendix B.

4.2.2. Determination of Number Density

The relation between signal intensity (S) and species number density (N) is a complex product of the differential scattering cross section, state number density, incident beam energy (power times sampling time), solid angle of the detection optics, and the length of the detection volume. This relation may be simplified to an optical proportionality constant k_i for species i by the simple equation below:

$$N_i = k_i S_i \quad (16)$$

This must be done for both the nitrogen and ethylene signals obtained.

Consider Figure 27 below, it shows an image of the Raman spectrum attained along the span of the tunnel at a given axial and vertical location in the test section. There is no flow and static properties are known. In short, the image presents an array, $m \times n$, with m

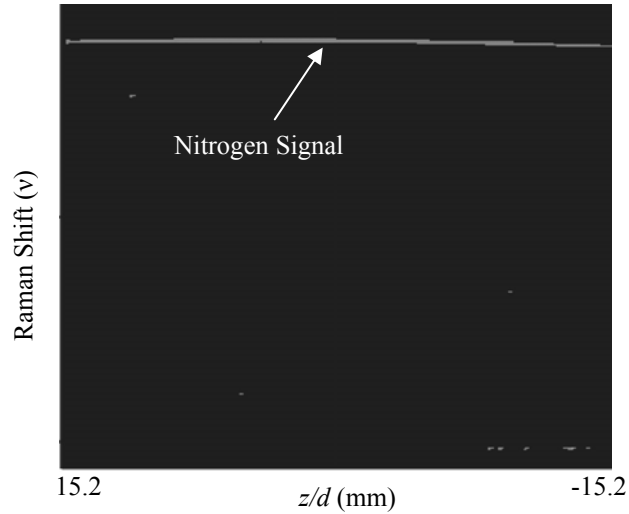


Figure 27. Tunnel Raman scattering of air at atmospheric conditions

rows representing the Raman shift and n columns representing the tunnel spanwise coordinate. The value at each pixel in the array represents a single intensity value at location (m,n) . The number density within the tunnel (assuming uniform distribution) can be determined by the perfect gas relation, where:

$$\rho_{air} = \frac{P_{air}}{R_{air}T_{air}} \quad (17)$$

The molar density C_{air} may be determined by:

$$C_{air} = \frac{\rho_{air}}{MW_{air}} \quad (18)$$

where MW_{air} is the *molecular weight of air*. Furthermore, the number density of air, N_{air} may be found by:

$$N_{air} = C_{air} \cdot \mathcal{N}_A \quad (19)$$

where \mathcal{N}_A is *Avagadro's number*. Considering that air is typically composed of 79% nitrogen, the nitrogen number density, N_{N_2} can be found by:

$$N_{N_2} = 0.79 \cdot N_{air} \quad (20)$$

Thus, the number density of nitrogen is found given the tunnel test section conditions. Due to variation between pixel column intensity and image warping, the nitrogen signal intensity must be found for each of n spanwise location pixels. This is accomplished by integrating the signal intensity over some subset of the m pixels defined as the nitrogen Raman shift. Once this has been accomplished, the n nitrogen optical calibration constants may be found using equation 16 at each spanwise coordinate location.

Next the ethylene optical calibration constant is determined. Since the nitrogen calibration constant is known, a Raman spectrum may be obtained for a mixture of ethylene

and air within the no flow test section at known atmospheric temperature and pressure. This mixture is obtained by saturating ethylene into the tunnel. The gas is allowed to disperse into the surrounding fluid for several minutes. Figure 28 gives a tunnel spanwise Raman spectrum for a mixture of ethylene and air at a fixed axial and vertical location. Notice the uniform spread of ethylene within the tunnel, this shows that the fuel has spread evenly throughout. Additionally, note that due to the high ethylene concentration (relative to nitrogen) within the tunnel, the nitrogen signal while present does not become apparent

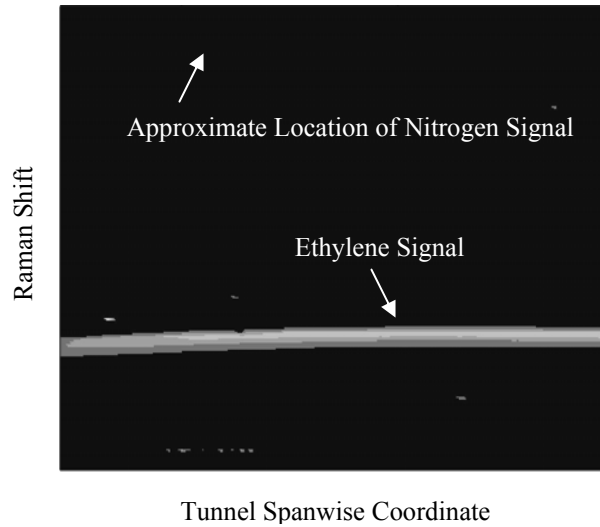


Figure 28. Tunnel Raman scattering for ethylene-air mixture at atmospheric conditions

in the image. Using Dalton's law of partial pressures, the number densities of the air and ethylene add up to the total number density present in the tunnel ($N_{mixture}$) which is found using the above equations. The number density of ethylene can be found by:

$$N_{C_2H_4} = N_{mixture} - (N_{N_2} + N_{O_2}) \quad (21)$$

or using the definition of presented in equation 16 and knowing that the ratio between the moles of nitrogen to oxygen in air is about 3.76 :

$$N_{C_2H_4} = N_{mixture} - \left(k_{N_2} \cdot S_{N_2} + \frac{k_{N_2} \cdot S_{N_2}}{3.76} \right) \quad (22)$$

Once the number density of ethylene is found, the optical calibration constant for each of the m spanwise location pixels may be found. The ethylene signal intensity is integrated over its respective Raman shift. Note that the band comprising the ethylene Raman shift is much larger than the nitrogen Raman shift.

An example of a raw image is shown in Figure 29 taken at x/d of 12 and y/d of 4.92 for the baseline configuration at $\bar{q} = 4.0$. The “salt and pepper” quality to the image is caused by background signal variation and is addressed in Appendix B. Notice that increases in the ethylene signal is accompanied by a respective decrease in nitrogen signal and vice versa. For each of the n spanwise coordinate pixels, the number density is obtained for nitrogen and ethylene by integrated the signal counts over each respective Raman shift and multiplying the integrated signals by their respective optical calibration constant. This results in n ethylene number densities and n nitrogen number densities for each image. This procedure is repeated for all images in a data set resulting in an end view distribution of ethylene and nitrogen number densities.

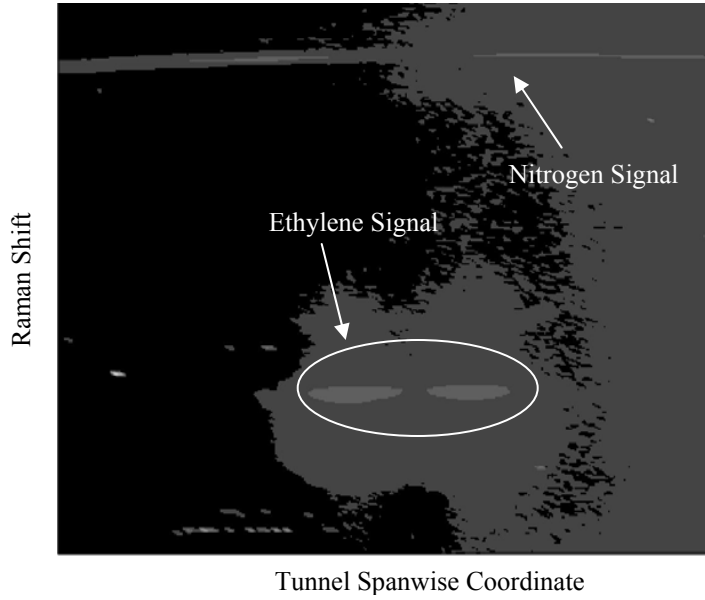


Figure 29. Raman spectrum at $x/d = 12$, $y/d = 4.92$ for baseline configuration

4.2.3. Mole Fraction and Equivalence Ratio

Once the number density of the respective species is determined, mole fraction (X_i) and equivalence ratio (ϕ) can be solved for. For a two species medium, the mole fraction of fuel and the equivalence ratio scale in proportion to one another. In the context of the present research, equivalence ratio gives a better idea of a fuel's combustibility. Mole fraction is used for determination of the ratio of specific heat in the algorithm described in section 4.3.

Mole fraction is defined here as the ratio of the molar density of a medium constituent divided by the total molar density of a system, or symbolically:

$$X_i = \frac{C_i}{C_{total}} \quad (23)$$

The molar density of a constituent is easily obtained from number density and may be found using equation 19.

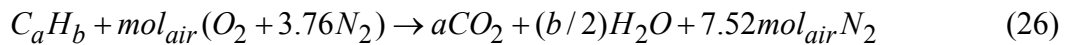
Equivalence ratio offers a unique way of viewing the combustibility of a gas mixture. It is defined as the ratio of the local fuel-air mass ratio to the fuel-air mass ratio for a stoichiometric process. Symbolically, it is defined as:

$$\Phi = \frac{(F / A)}{(F / A)_{st}} \quad (24)$$

where

$$F / A = \frac{\text{mass of fuel}}{\text{mass of air}} \quad (25)$$

the subscript *st* represents stoichiometric. Generally, a stoichiometric process is considered to be a reaction where the air is in just the amount required for complete combustion of the quantity of fuel in the system.⁵² A value of $\Phi = 1$ indicates stoichiometric fuel-air quantities, while a mixture with $\Phi < 1.0$ is termed fuel-lean and $\Phi > 1.0$ is termed fuel-rich. For a given reaction, the value for $(F/A)_{st}$ is constant. Determining $(F/A)_{st}$ is usually done by writing a chemical reaction in terms of one mole of a hydrocarbon fuel completely combusting with air to form carbon dioxide, water and nitrogen. For a given hydrocarbon, a stoichiometric reaction can be written as:⁵²



where

$$mol_{air} = a + b/4 \quad (27)$$

and $(F/A)_{st}$ can be determined as:

$$(F / A)_{st} = \frac{1}{4.762 \cdot mol_{air}} \frac{MW_{air}}{MW_{fuel}} \quad (28)$$

For ethylene:

$$(F/A)_{\text{st}} = 0.0678$$

4.2.4. *Summary*

By applying the analysis presenting in sections 4.2.2 and 4.2.3 to each raw image acquired from the Raman spectroscopy process, number density distributions across the tunnel span are obtained for the given axial and transverse location of the individual raw image. By combining all 29 number density distributions in a test run, a two-dimensional 29×129 (y - z plane) plot of number densities is created for each axial location. Equivalence ratio plots are used for mixing analysis, while mole fractions are used in a computer algorithm to determine the ratio of specific heats. However, the algorithm used requires exact location matching between all data files. In other words, if the algorithm is computing the flow properties in a y - z plane at a specific axial location then all required data sets must have the same data mesh. Since the conventional probing's data mesh (10×9) is much coarser than the mesh used for species sampling, the species sampling mesh must be transformed to match. Since probing data is actually an average within the area of the probe (diameter of 0.125 inches), species data is dividing into 90 smaller matrices of approximate size 0.125 by 0.125 inches. These sub-arrays are averaged to produce a new 10×9 with each new value corresponding in location to the probing data at the same location.

4.3. Aerothermodynamic Probing

Using the ethylene concentration data, along with the pitot pressure, cone-static pressure and total temperature, the conditions such as total pressure and Mach number can be determined at the probing axial location ($x/d = 12$). Since very little is known of the actual properties, an iterative solution is necessary. A computerized solution algorithm developed by Fuller⁴⁸ uses compressible flow relations and look-up tables to determine properties within a supersonic flow field. The algorithm, developed for use in single species injection into air, allows for species data from injection of helium, nitrogen, ethylene, argon or air. Required input and resulting outputs is listed in Table 4. Following is a summary of the algorithm.

Table 4. List of inputs and resulting outputs for Fuller algorithm

Inputs		Outputs	
P_{t2}	Pitot pressure	M	Mach number
P_{c-s}	cone-static pressure	P_t	total pressure
T_t	total temperature pressure	P	static pressure
X_i	injectant mole fraction	T	static temperature
		ρ	static density
		u	bulk velocity
		γ	ratio of specific heats
		a	speed of sound

The flow in question is assumed to be calorically imperfect, but adiabatic and thermally perfect to allow for high-temperature applications. This assumption requires an iterative solution since γ varies as a function of temperature. Therefore, an initial guess of static temperature is needed to compute γ . Using the fluid properties provided by resources such as the NIST webbook⁴¹, curve fits can be developed to relate specific heats c_p and c_v to temperature. From the cone-static pressure, pitot pressure and γ , the Mach number is determined from look up tables generated from the Taylor-McCall exact solution to a supersonic conical flowfield. This second order, ordinary nonlinear differential equation uses a single variable to represent the three-dimensional equations for fluid motion.⁴⁷ At the surface of the cone-static probe, the sensed pressure can be shown to relate to the static and dynamic pressures ahead of the attached cone shock (P_1 and q_1) by the following equation:

$$\frac{P_{c-s}}{P_1} = 1 + \frac{\gamma M_1^2}{2} \frac{(P_{c-s} - P_1)}{q_1} \quad (29)$$

dividing this relation by the Rayleigh-Pitot equation below allows Mach number to become a function of cone-static pressure, pitot pressure and γ which can be interpolated from an appropriate look up table. The numerical solution to the Taylor-McCall equations used in the Fuller algorithm is outlined by Sims⁵³ and allows flow solutions for a range of Mach numbers with γ varying from 1.39 to 1.67. A precise look-up table is formed by combining the Taylor-McCall solutions with solutions to the Rayleigh-Pitot formula. The Rayleigh-Pitot formula relates pitot pressure to static pressure ahead of the normal pitot probe shock in supersonic flow and is given as:

$$\frac{P_{t,2}}{P_1} = \left[\frac{(\gamma+1)M_1^2}{2} \right]^{\frac{\gamma}{\gamma-1}} \left[\frac{\gamma+1}{2\gamma M_1^2 - (\gamma-1)} \right]^{\frac{1}{\gamma-1}} \quad (30)$$

Note that the above method is only valid for Mach numbers above 1.12, below that value; the cone-static probe shock becomes detached.

Once a Mach number has been determined, a new static temperature can be computed using the adiabatic flow relation in equation 3. This new value for static temperature is compared to the original guess and the above process is repeated using the bisection root finding method until:

$$|T_{new} - T_{guess}| \leq tol ; \quad tol \sim 1.8^\circ R \quad (31)$$

where T_{guess} becomes the previous iteration's T_{new} .

Once a static temperature is found, the Rayleigh-Pitot formula in equation 30 may be used to compute a static pressure. Finally, total pressure is found using the adiabatic pressure relation in equation 2. Density may then be found using the perfect gas relation and other properties such as speed of sound and bulk velocity may be found as well.

For the algorithm to work properly, it is important to attempt to determine flow angularity to the probes which may cause erroneous readings. Probe measurement error is directly proportional to the angle between the flow and the probe, this is especially true for cone-static probes which are highly sensitive to flow angularity. To obtain a reading with 1% accuracy, the angle between the cone-static probe and the sensed flow must be less than 5°. Due to its design, the pitot probe is much less sensitive to flow angularity. The angle between the pitot probe and the sensed flow must be less than 20° to achieve 1% accuracy in reading. High flow angularity may manifest itself in the algorithm as a higher than critical value of P_{c-s}/P_{t2} . If the flow is impinging on the probe at high angles, the cone-

static and pitot probes may begin to reverse measurements. For example, consider a flow at 90° to a cone-static and pitot probe (an extreme example to make a point). Due to the configuration of the probe orifices, the cone-static probe begins to sense a stagnation pressure, while the pitot probe senses a static pressure. This causes a ratio of P_{c-s} to P_{t2} very near 1.0, causing imaginary numbers to be computed in the Taylor-McCall equations. This problem appears in the data sets along the bottom y -coordinate, where the probe is below the cavity lip, shielded from the main flow. Previous research on supersonic cavities has shown high regions of circulation exist immediately behind the backward-facing step.¹⁸ Ratios of cone-static to pitot pressure very near 1.0 may indicate high flow angularity causing errors in the data processing algorithm. This problem is not evident however, when the probe is located at or above the cavity ($y/d \geq 0.0$). For this reason, the probing data located below the cavity was no longer considered.

A correction to the method used by the algorithm to compute c_p is necessary. As stated earlier, the gas is assumed to be thermally perfect but calorically imperfect. However, the program assumes a constant c_p at standard temperature and pressure (which in turn can be used to find γ) for ethylene. A modification is made to replace the constant value of γ for ethylene with a temperature dependent curve fit over a range of static temperatures most likely to be seen in the fuel plume. This range of temperatures is determined from the highest and lowest total temperature probe values in the area of the fuel plume. Corresponding maximum and minimum static temperatures are determined by using the adiabatic flow relation for temperature (with γ at standard conditions). Calculated static temperature within the fuel plume ranged from 280°R to 540°R , with a ten percent buffer on either side of the temperature range. Static pressure is assumed to be at

freestream. Data for c_p is taken for ethylene at the given temperature range with a 1.8°R step from the NIST website.⁴¹ A second order correlation of the data with temperature is performed and the resulting equation is entered into the Fuller code. The correlation gives a fit of c_p to static temperature with less than 1% error (at 95% confidence).

5. Results and Discussion

5.1. *Overview of Data Analysis*

Data analysis can be separated into two categories: fuel mixing effectiveness and supersonic flow losses. This chapter scrutinizes each of the eight configurations (four inserts at two injection pressures each) in both categories. Shadowgraphs are presented to orient the reader to overall flow field structure in the region of interest. Of particular note in the shadowgraphs are shock and expansion structures associated with the pylon and cavity. Additionally, equivalence ratio end view contour plots obtained from Raman scattering measurements are shown and general comments on fuel plume shapes and concentration distributions are made.

Mixing and loss analysis is performed on each of the eight configurations at $x/d = 12$. Additional species concentration data are obtained for both the wide and baseline configurations at $x/d = 7.2$ and $x/d = 29.6$, allowing investigation into fuel mixing enhancement as the plume moves downstream. Data taken at $x/d = 12$ may be used as a comparison with previous research.⁵

5.2. *Shadowgraphs*

Shadowgraphs allow for visualization of flow field structures. Of particular interest in supersonic flows are shock waves and expansion fans. It is important to note that shadowgraphs are two dimensional representations of highly three-dimensional flows, any

interpretation of shock structures must be done carefully. For the present study, the shadowgraphs represent the flow field across a 6-inch span of the tunnel.

Figure 30 through Figure 33 show the shadowgraph images for the four inserts without injection. These images are included to help separate the effects of geometry and injection. Figure 34 through Figure 37 is a compilation showing the shadowgraph images of the baseline, medium, tall and wide configurations, respectively, with injection for a \bar{q} of 1.0 and 4.0 as indicated. Main flow in each image is from left to right, with the cavity positioned at the bottom of the images. The tunnel floor upstream of the cavity is visible as a light gray rectangular area on the bottom left of the figures. The cavity's backward facing step is also visible and begins at $x/d = 5.6$. The injection flow features of note are labeled in Figure 34a only but they appear in all configurations with injection. Shock waves are visible in shadowgraphs as an alternation of light and dark bands of image intensity as discussed in section 3.7. Light shock waves formed from upstream disturbances are noticed crossing from the left of the images for all figures. Mach angles of the shock waves are approximately 28° corresponding to a flow Mach number of approximately 2.1. An expansion fan formed from the far upstream is apparent in all images. The expansion fan is labeled in Figure 30 (baseline configuration without injection) and appears as a region of dark intensity between bands of lighter intensity. Once again, the origin of the axial direction ($x/d = 0.0$) is the injection port, and the origin of the transverse direction ($y/d = 0.0$) is the upstream lip of the cavity.

In Figure 30, no major flow features are evident around the injection port. Small disturbance shock waves and the expansion fan are the main features seen. A boundary layer is noticed as a darkened area just above the tunnel floor. As the flow encounters the

backward facing step, a lip shock is formed as the main tunnel flow interacts with the lower momentum cavity flow. A shear layer due to this tunnel and cavity fluid interaction is clearly visible as an expanding darkened region near the top of the cavity. Similar features are evident in Figure 31 for the medium pylon, with the addition of an attached shock off the pylon. The shock angle is consistent for the pylon inclination angle then turns to match the freestream angle. This attached shock is evident on the tall pylon in Figure 32, and due to the pylon's increased size, the shock appears stronger than in the medium case. The wide pylon in Figure 33 has an attached shock of similar angle to the medium due to its similar size. It also appears that the wide pylon's shock is slightly stronger than the medium's shock.

Referring to the baseline injection cases, Figure 34a and Figure 34b, the bow shock originating just upstream of the injection port is well defined, and tends to be the strongest shock feature. Near the wall, the bow shock is nearly perpendicular to the main flow due to the transverse fuel injection, then changes direction to match the main flow Mach angle. Just downstream of the bow shock, slight variation in the boundary layer thickness indicates the presence of the ethylene plume. As the fuel initially penetrates the freestream flow, a barrel shock is formed around the expanding plume. A Mach disk forms behind the barrel shock, though not readily identifiable in the low \bar{q} case.

The most distinguishable differences between Figure 34a and Figure 34b are bow shock shape and strength near the wall as well as barrel shock penetration and size. The initial bow shock angles for $\bar{q} = 1.0$ and $\bar{q} = 4.0$ are approximately $42^\circ \pm 1.5^\circ$ and $44^\circ \pm 0.7^\circ$ respectively. Additionally, because of the injected mass increase, the bow shock for $\bar{q} = 4.0$ displaces higher, and does not reach the final freestream flow Mach angle as quickly

as the $\bar{q} = 1.0$ case. This increase in fuel mass flow is also evident by the much larger and better defined barrel shock in the higher \bar{q} case. These differences indicate greater shock losses, increased fuel plume area and penetration at higher injection pressures.

Many of the same features seen in the baseline configurations are apparent in the medium cases, Figure 35. The primary differences are the strength, angle and position of the bow shock. For all pylons, the bow shock's origin is displaced to the downstream tip of the pylon, located where the attached pylon shock is in the non-injection case. Initial bow shock angles are measured from the origin of the pylon shock instead of at the wall as done in the baseline cases. In fact, for $\bar{q} = 1.0$, the bow shock is not noticeable until further downstream of the pylon. The initial bow shock angle for the low \bar{q} case is $33^\circ \pm 0.6^\circ$. For the high \bar{q} case, the initial shock angle is $42^\circ \pm 0.9^\circ$, less than the baseline shock angle. The barrel shock and cavity shear layer is identifiable for both values of \bar{q} . As \bar{q} increases, the bow shock noticeably strengthens and displaces upward. An increase in barrel shock penetration can be seen as well.

The tall pylons in Figure 36a and b show similar flow features as the baseline. In the vicinity of injection, the presence of the fuel plume strengthens and lifts the shock. The bow shock angle near the origin is $36^\circ \pm 0.5^\circ$ and $41^\circ \pm 0.6^\circ$ for $\bar{q} = 1.0$ and 4.0 respectively. Further downstream the shock matches the freestream Mach angle. As in the baseline cases, the increased shock angle in the higher \bar{q} case is evidence of increased fuel mass injection and penetration. Additionally, the increased intensity of the bow shock in the high \bar{q} case indicates a stronger bow shock when compared with low \bar{q} .

Shadowgraphs for the wide configurations, Figure 37a and b, show similar flow structures as previous pylons relative to the baseline case. Fuel injection raises and

strengthens the attached bow shock. The initial shock angles of $34^\circ \pm 0.7^\circ$ and $46^\circ \pm 0.5^\circ$, respectively, are lower than the baselines' angles, but slightly higher than the angles for the tall pylon. Additionally, the appearance of a dual shock structure near the tip of the pylon may be due to three dimensional effects. The bow shock strengthens and increases in angle as \bar{q} increases.

Overall, shadowgraphs shown below in Figure 30 through Figure 37 allow for general observations and comparisons of flow structure due to geometry and injection. The noticeable difference between the baseline's flow features with and without injection is the strength of the bow shock (which aids dramatically to flow loss). For the pylons, the attached shocks strengthen and lift due to the presence of injection. The important difference between the pylon and the baseline cases is the location of the bow shock origin, and the variation seen in strength and initial shock angle.

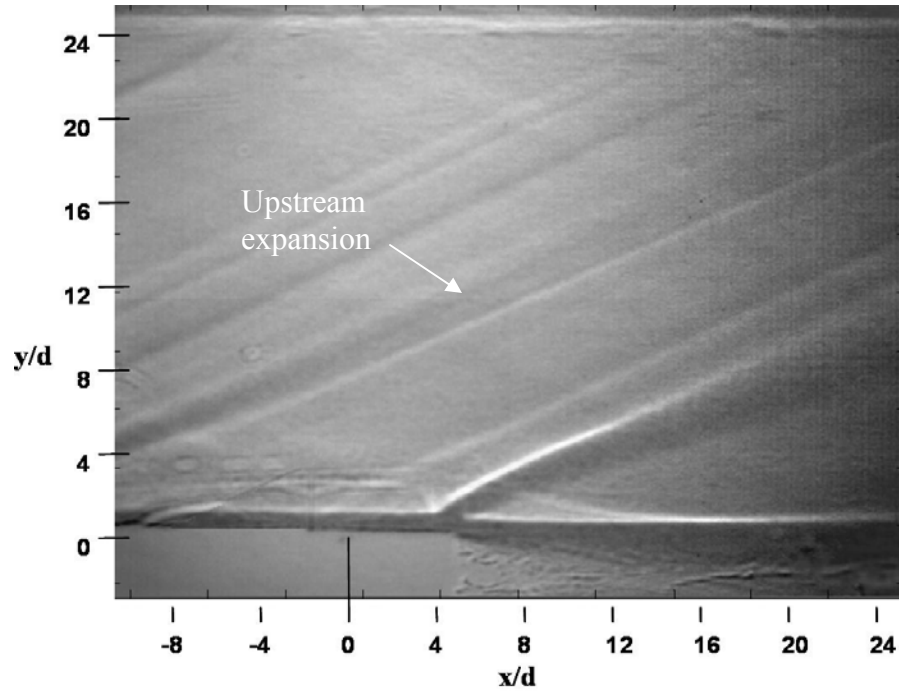


Figure 30. Shadowgraph of baseline configuration without injection

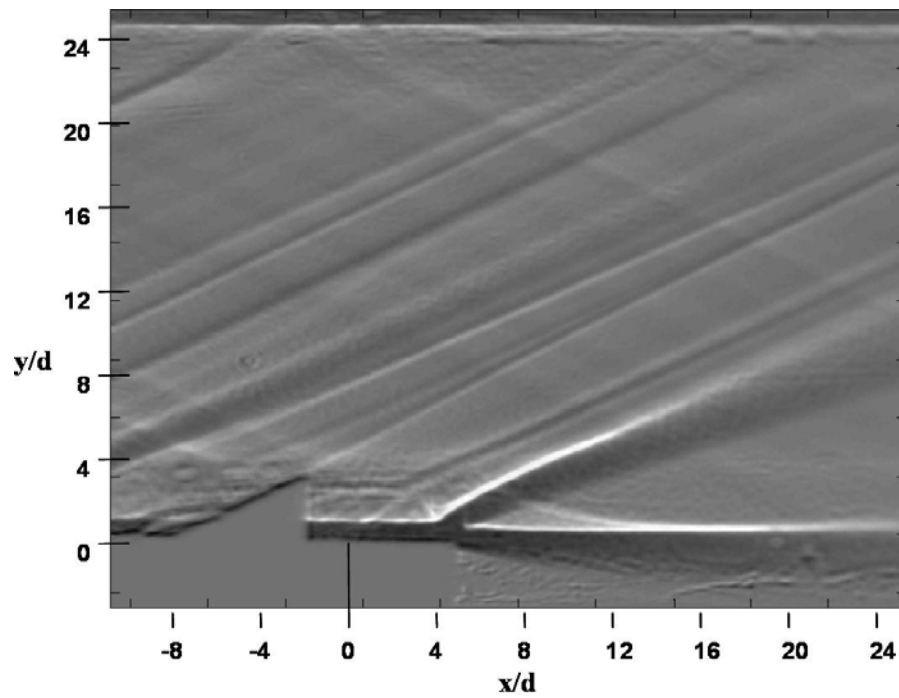


Figure 31. Shadowgraph of medium configuration without injection

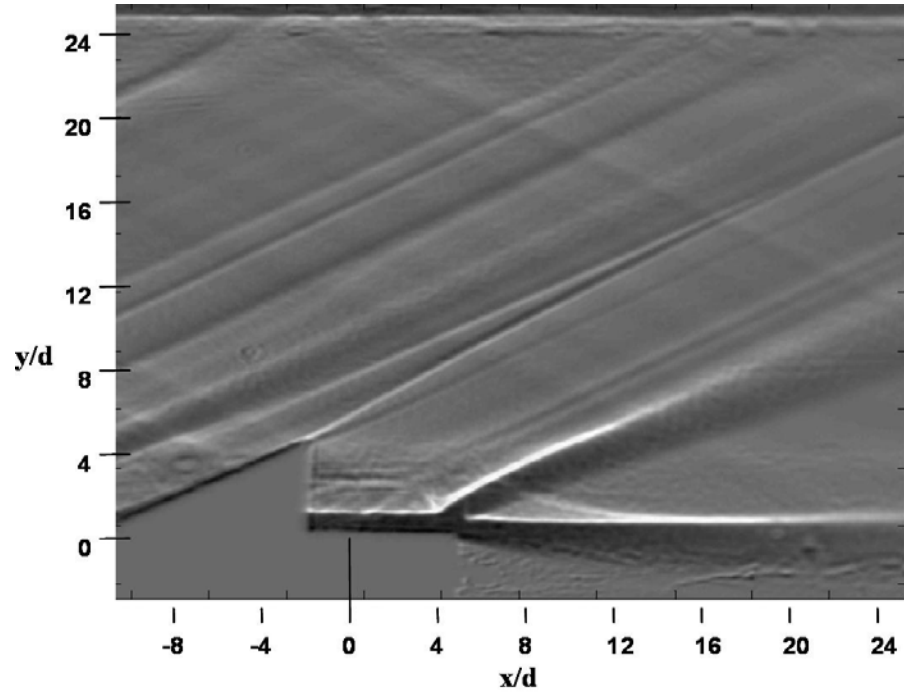


Figure 32. Shadowgraph of tall configuration without injection

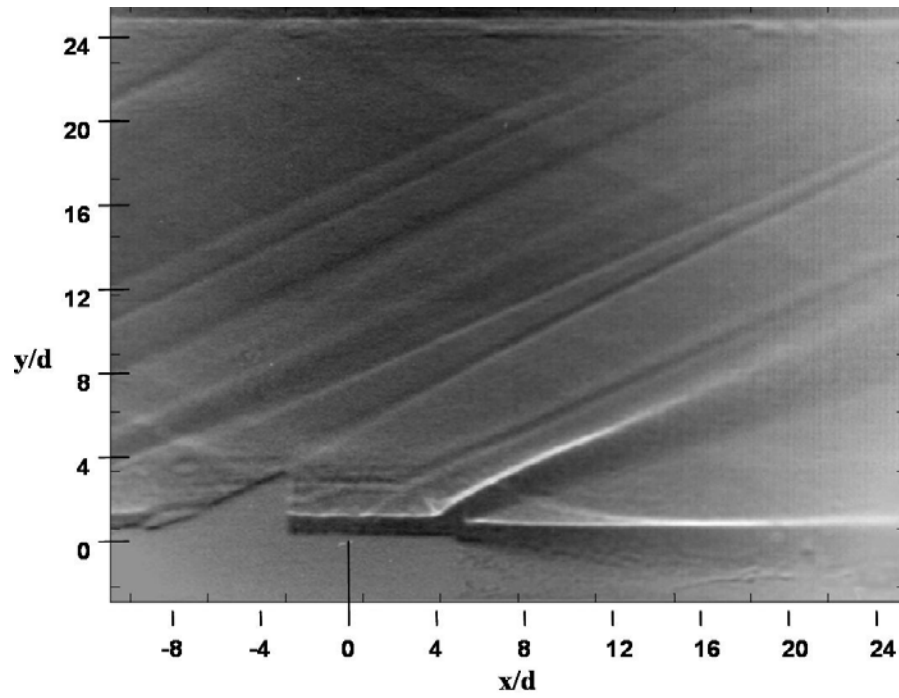


Figure 33. Shadowgraph of wide configuration without injection

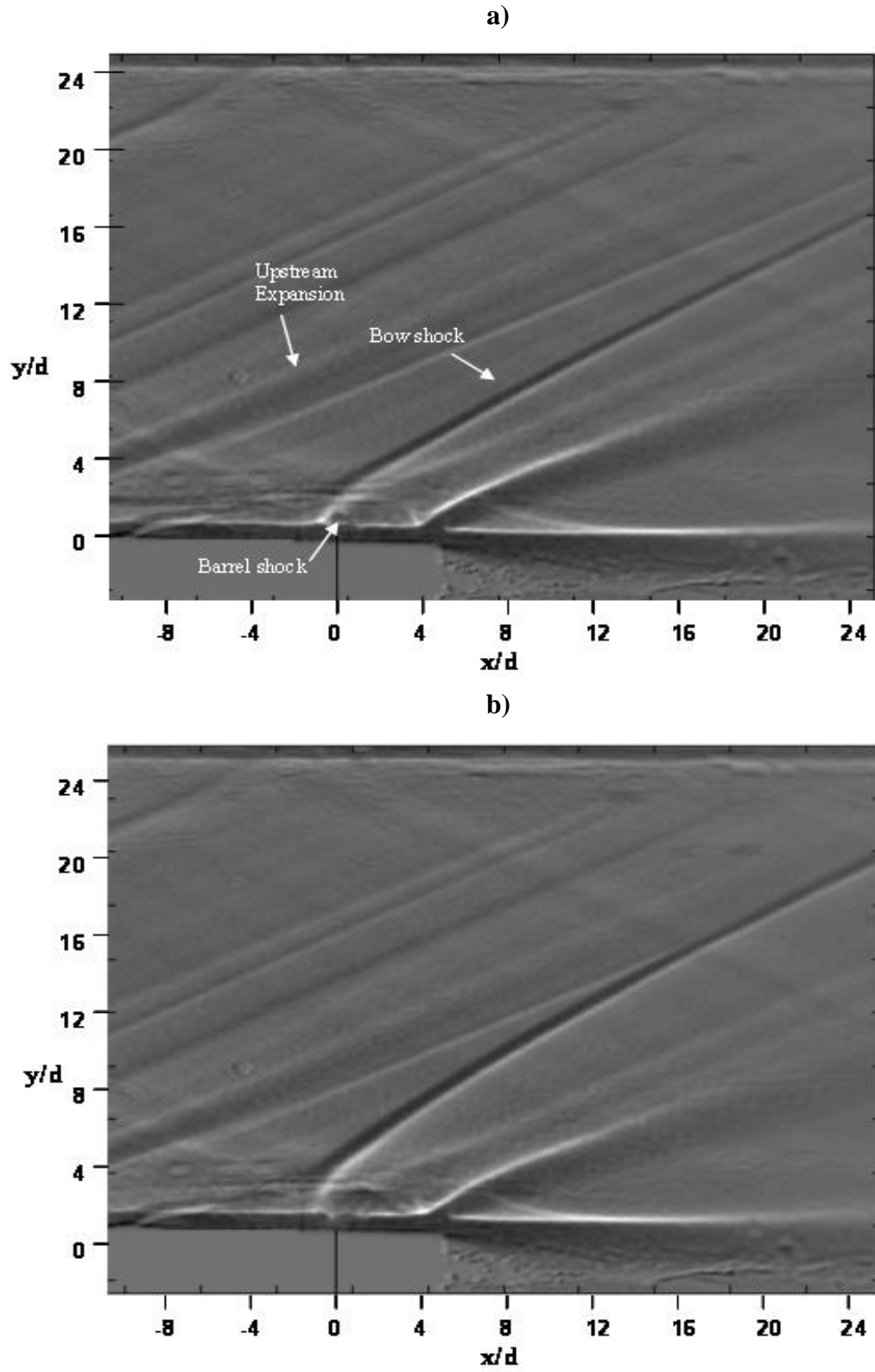


Figure 34. Shadowgraph of baseline configuration with $\bar{q} =$ a) 1.0 and b) 4.0.

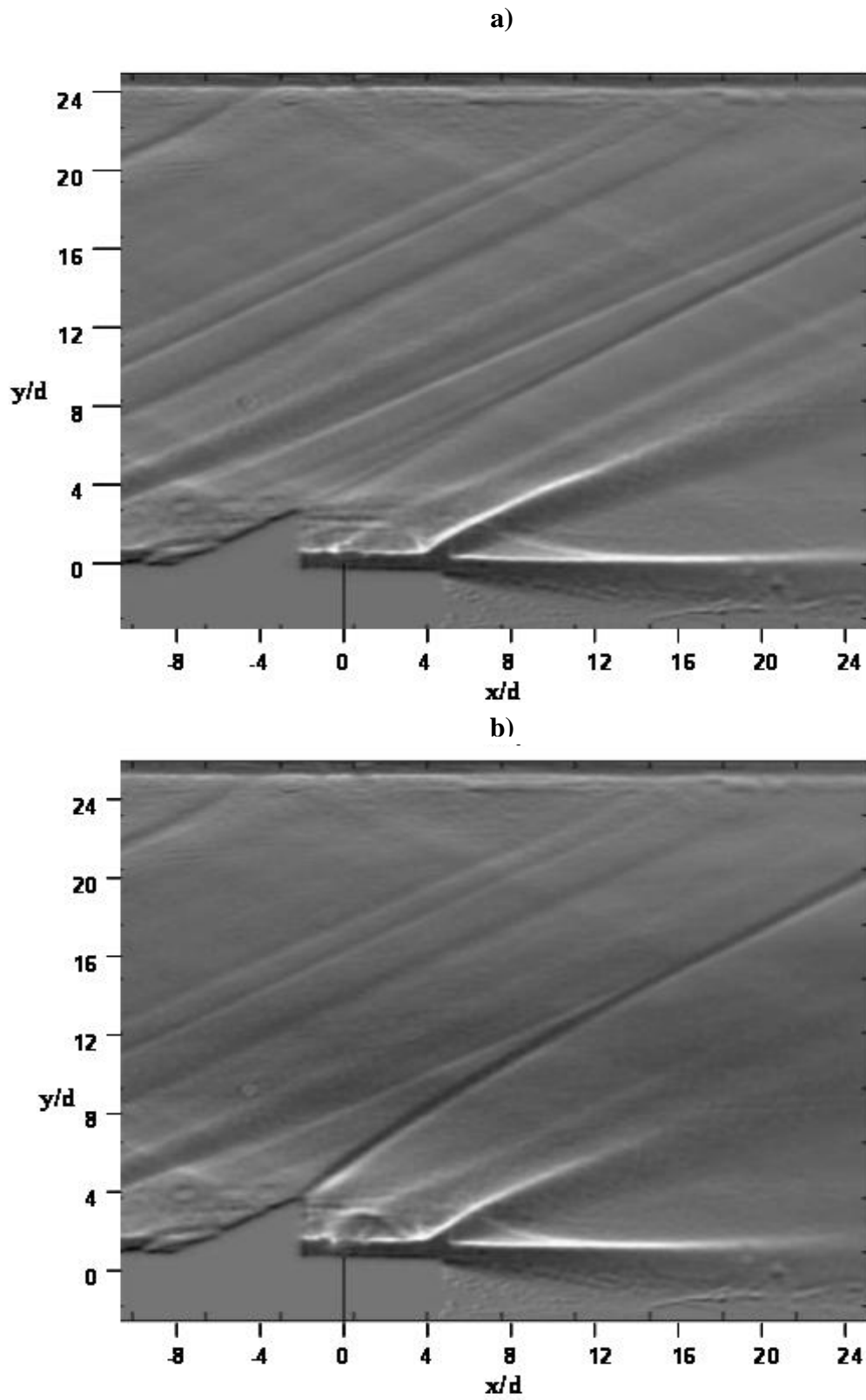


Figure 35. Shadowgraph of medium configuration with $\bar{q} =$ a) 1.0 and b) 4.0.

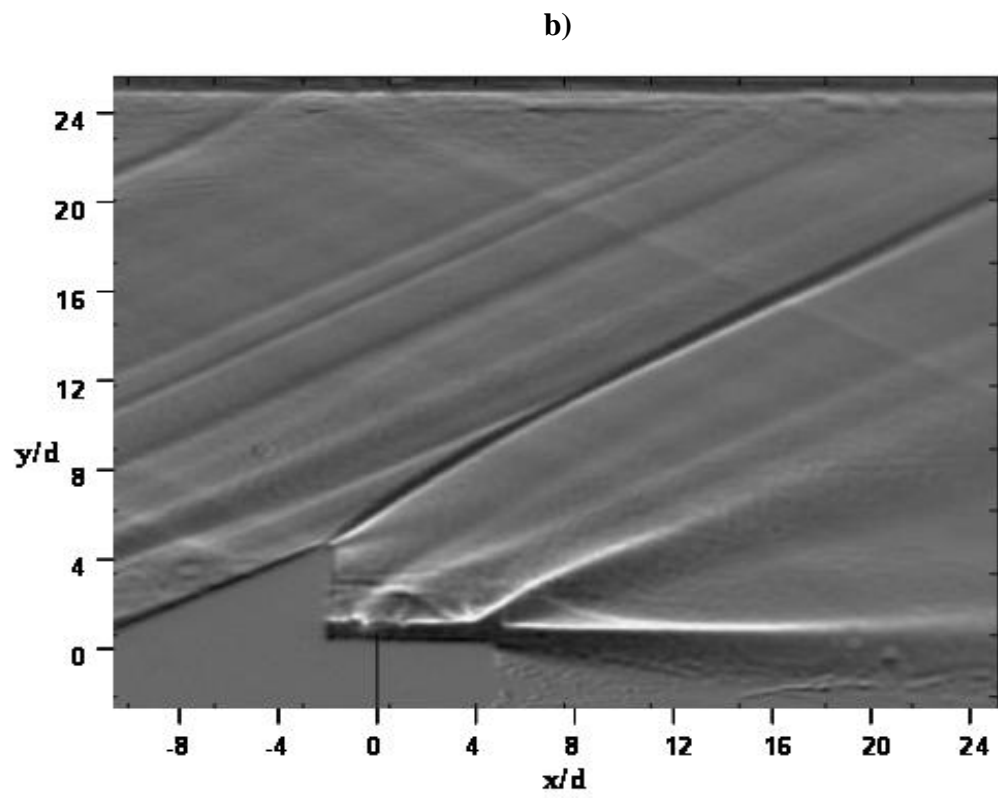
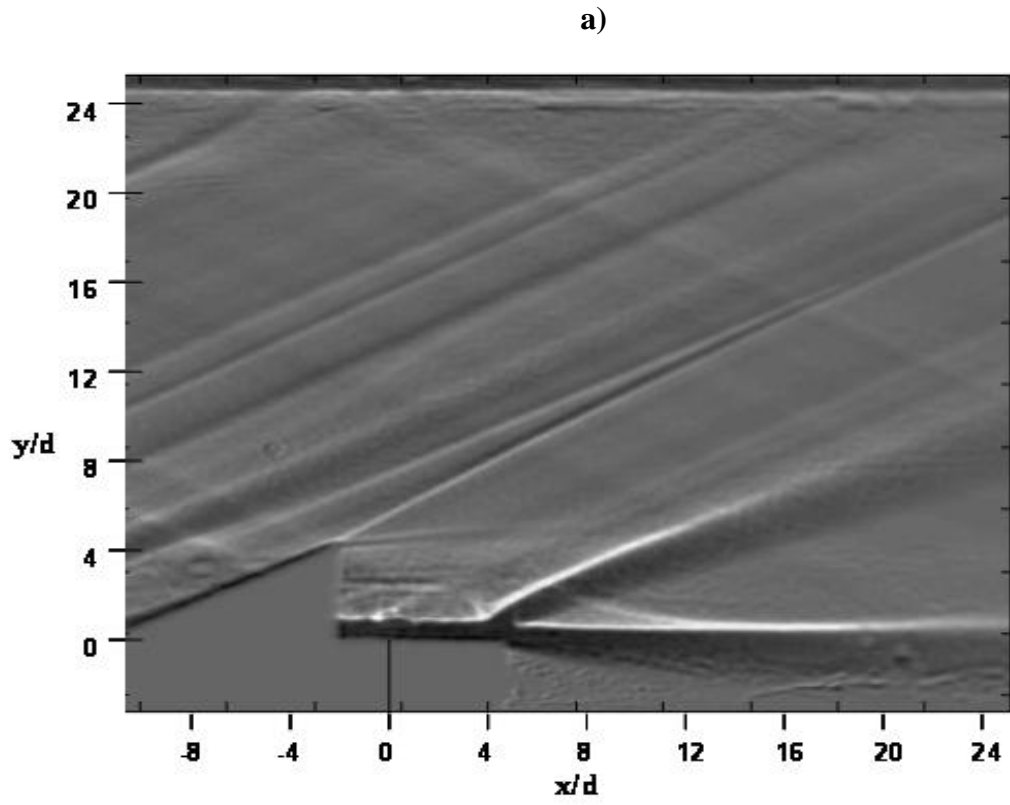


Figure 36. Shadowgraph of tall configuration with $\bar{q} =$ a) 1.0 and b) 4.0.

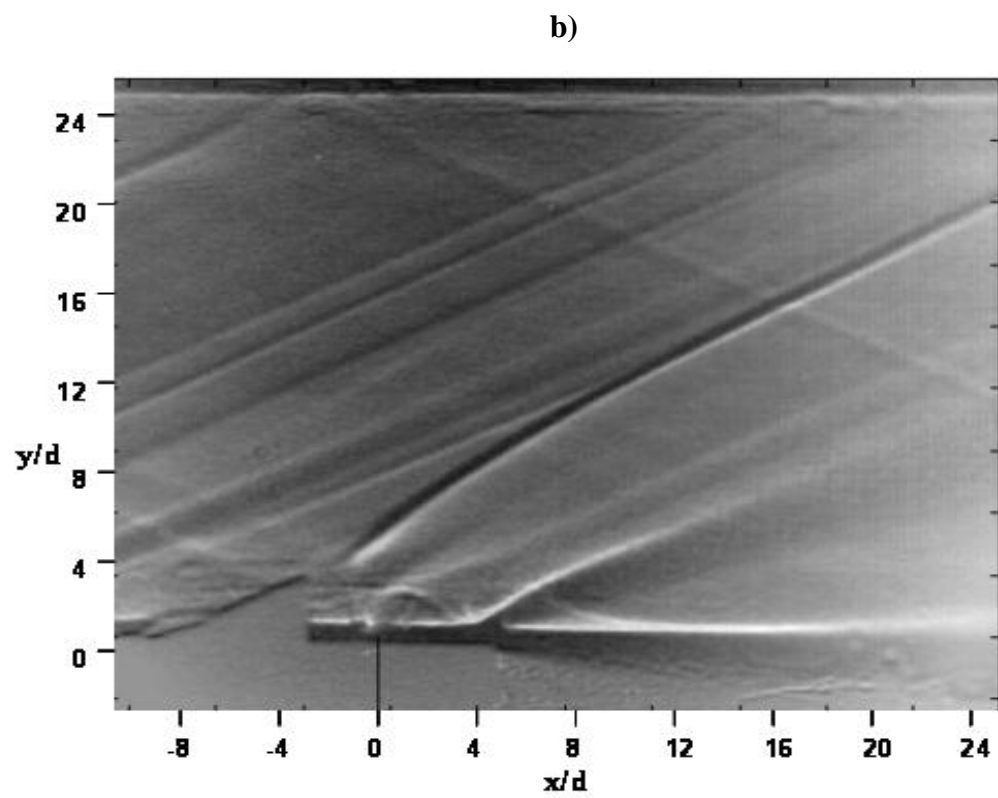
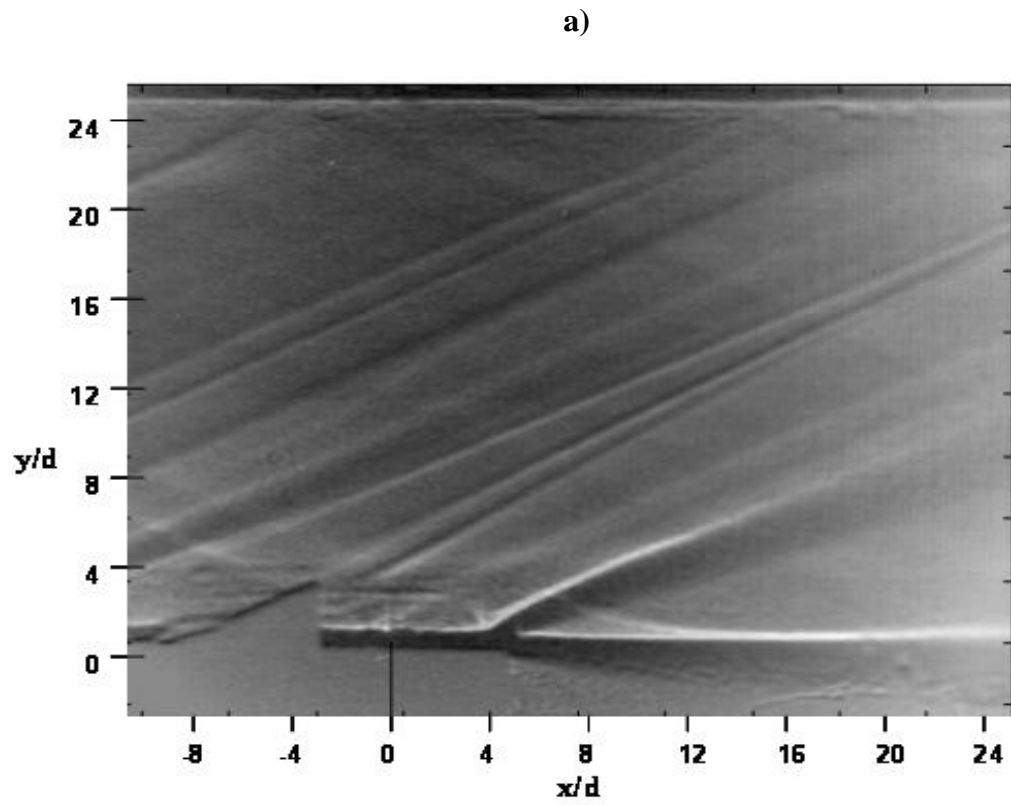


Figure 37. Shadowgraph of wide configuration with $\bar{q} =$ a) 1.0 and b) 4.0.

5.3. Species Composition Contour Plots

Figure 38 through Figure 41 show the time averaged contour profiles of constant ethylene equivalence ratio for each configuration at the measurement stations. The contours are oriented such that the reader is looking upstream toward the pylon, with the freestream flow coming out of the page. To aid in comparison between configurations, the contour color scales are the same for all plots. The minimum value of $\Phi = 0.1$ is used to ensure very low amounts of ethylene are tracked. The maximum value of $\Phi = 12.7$ corresponds to the maximum concentration found in the configurations. The fuel plumes' structures, sizes and locations within the test section are comparable to previous research indicating a good match in test conditions.⁵ Tabulated values for the maximum Φ are presented in Table 9 in section 5.4.3. Higher resolution plots are presented in Appendix C to allow finer detail into the lower injection pressure cases' plume structure.

Figure 38 gives the baseline's Φ contours at each of the three streamwise locations sampled with injection at $\bar{q} = 1.0$ and 4.0 as indicated. At $x/d = 7.2$ (Figure 38a and Figure 38b), the fuel plume crowns and is at its most concentrated state. The counter-rotating vortices are clearly seen as two lobes for both \bar{q} values. Most of the fuel is concentrated within the interior of the vortices and little mixing with the main flow is evident. The asymmetric way the ethylene concentrates within the left vortex at high \bar{q} indicates the three-dimensionality of the flow. Plume penetration is reduced for the low \bar{q} case due to the lower jet momentum. At $x/d = 12$ (Figure 38c and Figure 38d), the fuel plume begins to increase in area. Concentration within the vortices decreases as the fuel begins to spread and mix with the main flow. An increased amount of fuel becomes entrained in the cavity

($y/d \leq 0.0$), especially noted in the low \bar{q} case. For the low \bar{q} case, the counter-rotating vortices are defined, but are much smaller. At $x/d = 29.6$, mixing is no longer dominated by the vortex structures. In the low \bar{q} case, diffusion of fuel has clearly taken over and the presence of the vortex is no longer discernable; however, the maximum concentration of fuel (noted by maximum equivalence ratio, Φ_{max}) remains near the plume center. At the

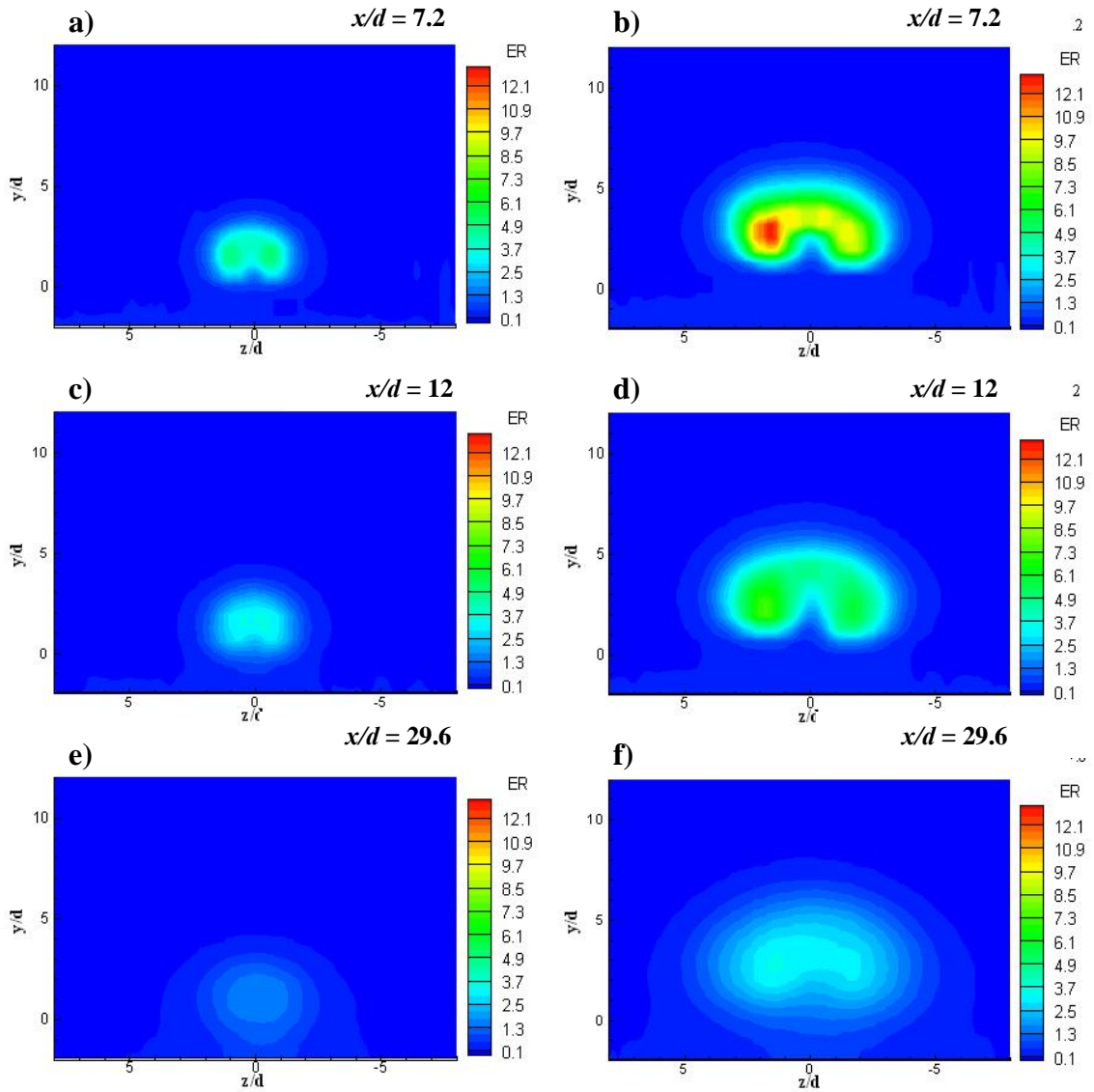


Figure 38. Baseline equivalence ratio contours for a), c), e) $\bar{q} = 1$ and b), d), f) $\bar{q} = 4$.

higher injection pressure, the counter-rotating vortices are still apparent, but have lost much of their previous resolution. The plume continues to expand in area and apparent penetration height. Overall, for both \bar{q} , Φ_{max} decreases as the plume moves downstream, a sign of fuel being transported away from and air being transported into the interior of the plume where the fuel concentration is the highest.

Species concentration data are presented for the wide pylon at an $x/d = 7.2, 12$ and 29.6 in Figure 39. Results are presented in the same format as in the baseline configuration. At $x/d = 7.2$ it is apparent that the distribution of fuel is drastically changed due to the presence of the pylon. Penetration is increased and plume width is decreased compared to baseline. Additionally, Φ_{max} is lower for both $\bar{q} = 1.0$ and 4.0 . A third fuel lobe is present and the location of Φ_{max} is lifted above the vortex pair. The vortex pair is not as large and defined as seen in the baseline, and only the right lobe is readily seen in the low \bar{q} case. The location of Φ_{max} and the decrease in size and shape of the vortices indicate that the core of the fuel plume is no longer centered within the vortex pair. Note that the asymmetric distribution of fuel in the vortex pair is opposite that seen in the baseline. This suggests an additional three-dimensional quality added to the flow by the pylon shape and possible misalignment with the freestream. At $x/d = 12$ (Figure 39c and Figure 39d), the major concentration of fuel continues to migrate up away from the counter-rotating vortices into the freestream (for the high \bar{q} case) and out away from the interior of the plume (for both high and low \bar{q}); little change is seen in the jet penetration for the lower injection pressure case. By $x/d = 29.6$ (Figure 39e and Figure 39f), the counter-rotating vortex pair seen in the high \bar{q} case is almost totally absent as the plume continues to expand. Plume area increases and plume interior fuel concentration decreases for both values of \bar{q} .

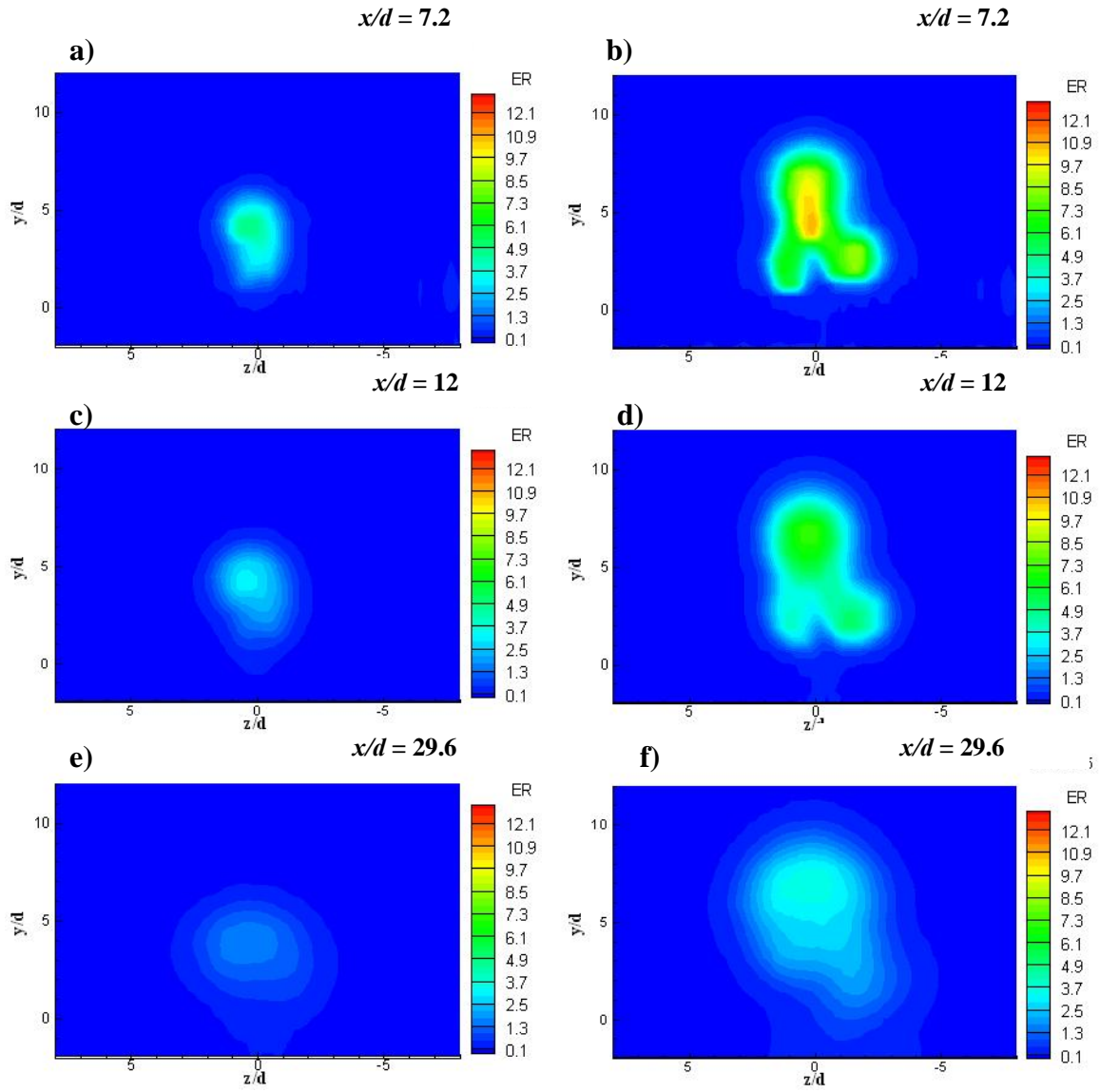


Figure 39. Wide equivalence ratio contours for a), c), e) $\bar{q} = 1$ and b), d), f) $\bar{q} = 4$.

Species concentration data are presented at a location of $x/d = 12$ for both the medium and tall configurations. Figure 40 shows Φ contour plots for the medium pylon. Comparison is made to both the baseline and wide configurations at the same axial location. The fuel plume structure and concentration distribution is similar in shape to the

wide pylon. The location of Φ_{max} is again located above the counter-rotating vortices, the value of which is slightly lower than in the wide and much lower than baseline for both values of \bar{q} . The vortex pair is visible in the high \bar{q} case (Figure 40b) and only the right vortex is apparent in the low \bar{q} case (Figure 40a), evidence of the same asymmetric distribution of fuel within the vortices seen in the wide configuration. At high \bar{q} , the fuel penetrates into the freestream higher than the baseline but less than observed in the wide case. At low \bar{q} , penetration appears approximately equal to the penetration found in the wide configuration.

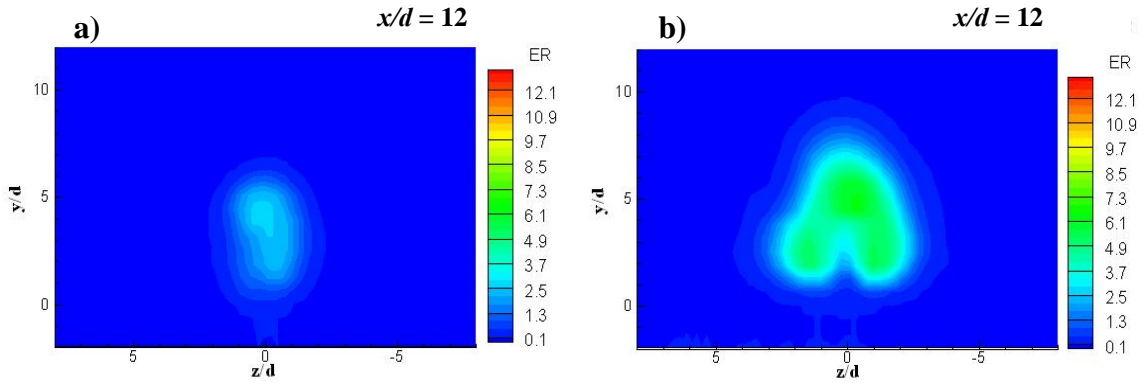


Figure 40. Medium equivalence ratio contours for a) $\bar{q} = 1$ and b) $\bar{q} = 4$.

Figure 41 shows the Φ contours for the tall configuration at $x/d = 12$. Overall plume structure for both $\bar{q} = 1.0$ (Figure 41a) and $\bar{q} = 4.0$ (Figure 41b) is similar to that seen in both the wide and medium configurations. The two bottom lobes of fuel indicate the presence of the counter-rotating vortex pair. The third fuel lobe is located above the vortices. Penetration of the fuel plume is much higher than baseline, and as high if not higher than the wide and medium configurations at both \bar{q} . The location of Φ_{max} for the

$\bar{q}=1.0$ case is above the vortex pair as seen in the other pylon configurations, but within the right vortex at $\bar{q} = 4.0$. The tall configuration's penetration of the maximum fuel concentration is higher in the freestream for the lower \bar{q} case.

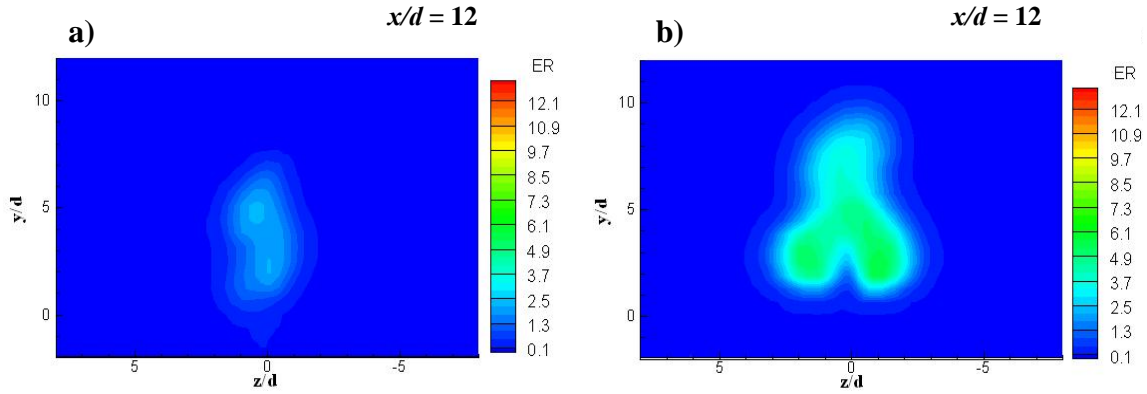


Figure 41. Tall equivalence ratio contours for a) $\bar{q} = 1$ and b) $\bar{q} = 4$.

5.4. Mixing Analysis

5.4.1. Overview

Mixing analysis aims to investigate the ability to prepare fuel for quick and efficient burning over as large of a flow cross-section as possible. Examination of each configuration's mixing effectiveness is done primarily by analyzing the species concentration data. All pylon configurations are compared against one another at $x/d = 12$. The availability of species concentration data at several axial locations ($x/d = 7.2, 12$ and 29.6) for the baseline and wide configurations allow for trajectory analyses and mixing rates to be obtained. Figures of merit for fuel mixedness in this study include:

fuel plume penetration, maximum fuel equivalence ratio penetration, plume area, and finally mixing efficiency (η_m). It should be noted that uncertainty and error in the species concentration measurements must be taken into consideration when viewing the data. This uncertainty is dealt with in Appendix E.

5.4.2. Fuel Penetration

Fuel plume penetration (h_p/d) is defined here as the maximum vertical height from the transverse centerline to the edge of the fuel plume, where Φ is 0.2. This value of the plume's edge is chosen because it is adequately below the ethylene-air lower flammability limit but high enough to define the fuel plume and separate it from fuel that becomes entrained within the cavity (which appears at Φ up to approximately 0.15). The penetration of Φ_{max} (h_c/d) is also determined. The core of the fuel jet is assumed here to be at the location of Φ_{max} . This value is simply the vertical height above the transverse centerline to the location of the given configuration's value for Φ_{max} . Finally, plume penetration analysis also allows for comparison to previous research⁵.

5.4.2.1. Plume Penetration Height Comparison

All configurations' penetration are compared at $x/d = 12$. The plume penetration (h_p/d) is shown for each injection case in Figure 42. Pylon height is shown to compare plume penetration above each pylon. Plume penetration data are summarized in Table 5 where change in h_p/d is shown as percent difference. As expected, the pylons increase plume penetration over that of the baseline for both values of \bar{q} . At $\bar{q} = 1.0$, the tall configuration's plume penetrates the highest over the baseline. Plume penetration is

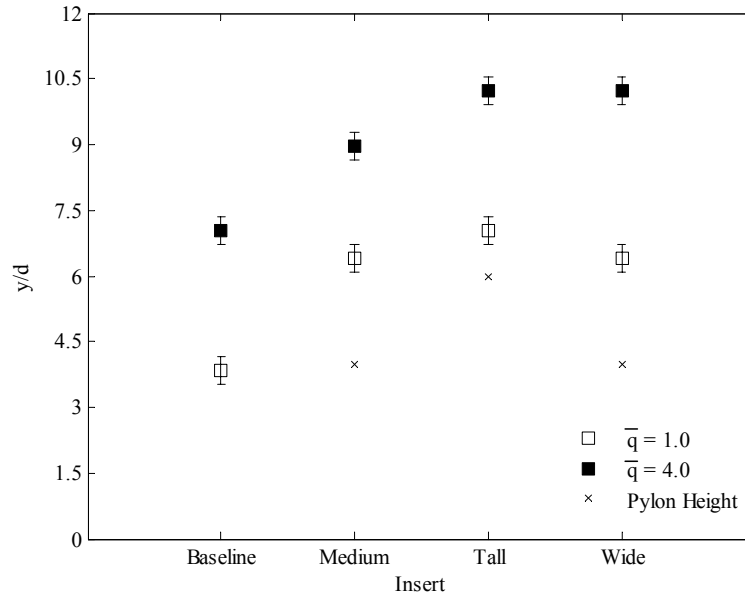


Figure 42. Plume penetration (h_p/d) comparison between inserts at $x/d = 12$

greater at $\bar{q} = 4.0$. The wide and tall configurations have approximately the same plume penetration increase over the baseline, while the medium configuration has the least increase in plume penetration over the baseline. All fuel plumes penetrate higher than their respective pylon insert. The medium and wide configurations have the greatest plume penetration above their pylons at $\bar{q} = 1.0$. Penetration above the tall pylon is limited.

Penetration above pylon height is increased in the high \bar{q} cases. The wide configuration's plume penetrates the most over the pylon, while the tall configuration has the smallest increase in plume penetration above the pylon. Penetration increase due to \bar{q} change from 1.0 to 4.0 is noted as well. Baseline plume penetration is the most improved out of all configurations as \bar{q} is increased. Of the three pylons, the wide sees a greater augmentation in plume penetration as \bar{q} rises, while both the medium and tall pylons see approximately the same change.

Table 5. Plume penetration (h_p/d) comparison between inserts at $x/d = 12$

	Baseline		Medium		Tall		Wide	
	$\bar{q} = 1.0$	$\bar{q} = 4.0$	$\bar{q} = 1.0$	$\bar{q} = 4.0$	$\bar{q} = 1.0$	$\bar{q} = 4.0$	$\bar{q} = 1.0$	$\bar{q} = 4.0$
h_p/d (-)	3.84	7.04	6.40	8.96	7.04	10.24	6.40	10.24
Difference over								
Baseline (%)	—	—	67	27	83	46	67	46
Difference over								
Pylon								
Height(%)	—	—	60	124	17	71	60	156
Difference as								
\bar{q} increases								
(%)	83		40		45		60	

5.4.2.2. Core Penetration Height Comparison

The location of the maximum equivalence ratio within the plume is associated with the core of the fuel jet. Therefore, the fuel core penetration (h_c/d) is determined by the vertical distance from the transverse centerline ($y/d = 0.0$) to the location of maximum Φ within the plume. As in the analysis of h_p/d , all configurations are compared at x/d of 12. Figure 43 presents the values of h_c/d for all configurations at both \bar{q} . Pylon height is again added to the figure. Tabulated values of core penetration data is presented in Table 9. At low \bar{q} , all pylons see increase in h_c/d over the baseline case, with the tall pylon being the best performer. As \bar{q} increases to 4.0, the wide configuration's enhancement of

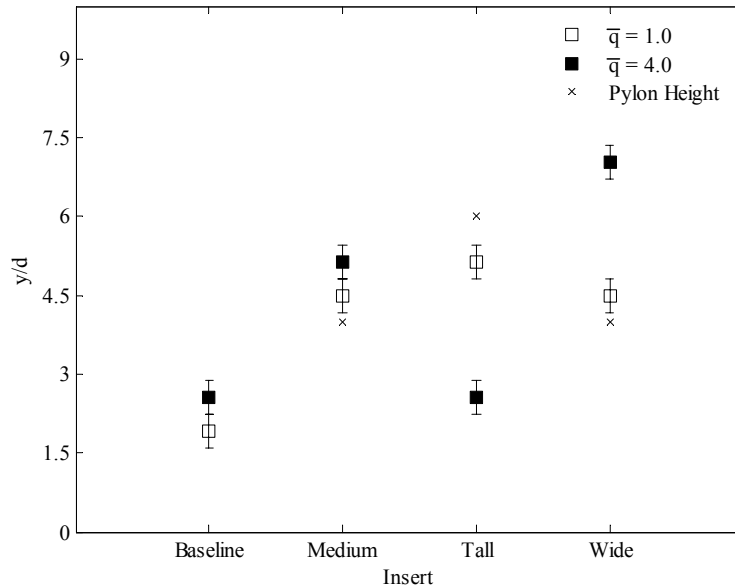


Figure 43. Plume core penetration (h_c/d) comparison between inserts at $x/d = 12$

core penetration is the most amplified. It is interesting to note that the tall configuration's h_c/d actually decreases and matches the baseline's value as injection pressure rises. This trend is seen in the tall pylon's Φ contour plots in Figure 41. The majority of fuel concentration remains within the counter-rotating vortices.

The height of the plume core relative to the pylon may shed light on total plume penetration. Core penetration is above the pylon for both the wide and medium pylons. However, the presence of maximum concentration of fuel for the tall configuration appears lower than the pylon for both values of \bar{q} .

Changes in core penetration occur with variation in injection pressure. As expected in the baseline, an increase in injection pressure translates to an increase in core penetration. Both the medium and wide pylons see a positive change in core penetration as \bar{q} is raised, with only the wide pylon's h_c/d increase being greater than that of the baseline. The tall pylon's core penetration change is actually negative for a rise in \bar{q} .

Table 6. Plume core penetration (h_p/d) comparison between inserts at $x/d = 12$

	Baseline		Medium		Tall		Wide	
	$\bar{q} = 1.0$	$\bar{q} = 4.0$	$\bar{q} = 1.0$	$\bar{q} = 4.0$	$\bar{q} = 1.0$	$\bar{q} = 4.0$	$\bar{q} = 1.0$	$\bar{q} = 4.0$
h_c/d (-)	1.92	2.56	4.48	5.12	5.12	2.56	4.48	7.04
Difference over								
Baseline (%)	—	—	133	100	167	0	133	175
Difference over								
Pylon								
Height(%)	—	—	12	28	-14	-57	12	76
Difference as								
\bar{q} increases (%)	33		14		-50		57	

Overall, at $x/d = 12$, both h_p/d and h_c/d for each pylon configuration show increases in penetration over the baseline for both injection pressures. At $\bar{q} = 1.0$, h_p/d and h_c/d scale proportionately to pylon height. However, this is not the case in the $\bar{q} = 4.0$ case. Both the wide and medium pylons sustain the core of the fuel plume above the counter-rotating vortices; this allows maximum penetration of the plume into the freestream. The tall pylon's inability to sustain the core of the plume above the vortex pair at high \bar{q} hinders its ability to improve penetration over the baseline effectively. This issue may be due to pylon aspect ratio. The wide pylon shows the best plume and core penetration improvement over the baseline.

5.4.2.3. Comparison to Previous Research

Previous research by Montes performed similar plume penetration analysis on all four configurations at $x/d = 12$.⁵ In the study, the plume penetration heights are obtained through Planar Laser-Induced Fluorescence of nitric oxide (NO-PLIF). Imaging results from the PLIF technique relates image intensity to NO concentration. The plume boundary, defined as where the image intensity drops to 10% of the local maximum intensity, is quite similar to the definition used in this report. Knowing what equivalence ratio occurs at the plume penetration height figured from the previous report may allow a correlation between NO-PLIF intensity and equivalence ratio. Table 7 gives the plume penetration and Φ figured for the previous data and compares the values to the current research. It should be noted that the key difference between the two experiments is that nitric oxide is injected instead of ethylene and the previous research's pylon location is 2.3 inches upstream of the cavity as opposed to 0.35 inches for the current research. All other conditions are the same (facility, freestream conditions, pylons used, injection source, etc.).

As mentioned previously, since the injected gas is of similar molecular weight as ethylene, little difference is expected from the behavior of the fluid. The further upstream pylon location in the previous experiment may simply result in a lifting of the plumes due to interaction with the tunnel floor.

Table 7. Comparison of current and previous plume penetration at $x/d = 12$

	Baseline		Medium		Tall		Wide	
	$\bar{q} = 1.0$	$\bar{q} = 4.0$	$\bar{q} = 1.0$	$\bar{q} = 4.0$	$\bar{q} = 1.0$	$\bar{q} = 4.0$	$\bar{q} = 1.0$	$\bar{q} = 4.0$
Current h_p/d								
(-)	3.84	7.04	6.40	8.96	7.04	10.24	6.4	10.24
Previous h_p/d								
(-)	4.70	7.48	7.30	10.43	8.61	12.35	7.57	11.13
Percent Difference								
(%)	-18.3	-5.9	-12.3	-14.1	-18.2	-17.1	-15.5	-8.0
Φ at Previous								
h_p/d	0.08	0.11	0.07	0.10	0.06	0.08	0.05	0.07
(-)								

Current values for h_p/d are on average 14% below h_p/d found in the previous research. This difference again could be due to rounding error, different pylon locations and different definitions of the plume's boundary. It should be noted when looking at the penetration comparison that the previous research's values for h_p/d have to be rounded to match the closest vertical location in the current species concentration data mesh. This rounding caused a difference in h_p/d from -4.7 to 2.7% between the previous and current values. Nonetheless, values for Φ at the plume boundary computed from the NO-PLIF

data are fairly constant. The mean Φ found at 10% PLIF intensity corresponds approximately to 0.08 with a standard deviation of 0.02.

5.4.2.4. Penetration Trajectory

The plume and core penetration trajectories for the wide and baseline configurations are evaluated at both injection pressures. Plume penetration trajectory is defined as the variation in plume penetration with downstream distance. The downstream locations used to determine the penetration trajectories are $x/d = 7.2, 12$ and 29.6 . Past studies show that plume data varies exponentially in the far-field region.³² Therefore, power-law curve fits are used to predict the rate of change in penetration with downstream location. Even though the first axial location may not be considered far-field, it is included in the correlation for prediction of the local trajectory. The power law used is of the following form:

$$\frac{h}{d} = \beta \left(\frac{x}{d} \right)^n \quad (32)$$

Where the values for β and n are found using the method of least squares described in Appendix D. The exponent n relates the rate of change of the variable of interest. Therefore, a positive value of n indicates a rate of penetration increase. In the instance of penetration trajectory, large positive values of n are desirable since they indicate increased rates of penetration into the freestream.

The measured plume penetration heights (h_p/d) for the wide and baseline configurations at both injection pressures are shown along with their respective correlations in Figure 44. A basic trend in plume penetration rate of change can be seen. For each

value of \bar{q} , the wide pylon penetrates higher over the baseline at each streamwise location. The plume penetration of the wide pylon's low \bar{q} case is nearly as high as the baseline's plume penetration at high \bar{q} . Values for n for the $\bar{q}=1.0$ case are very near zero for the wide pylon and slightly negative for the baseline. As \bar{q} is increased, rates of change are still small, but noticeably positive. While similar in value (taking into account error), the

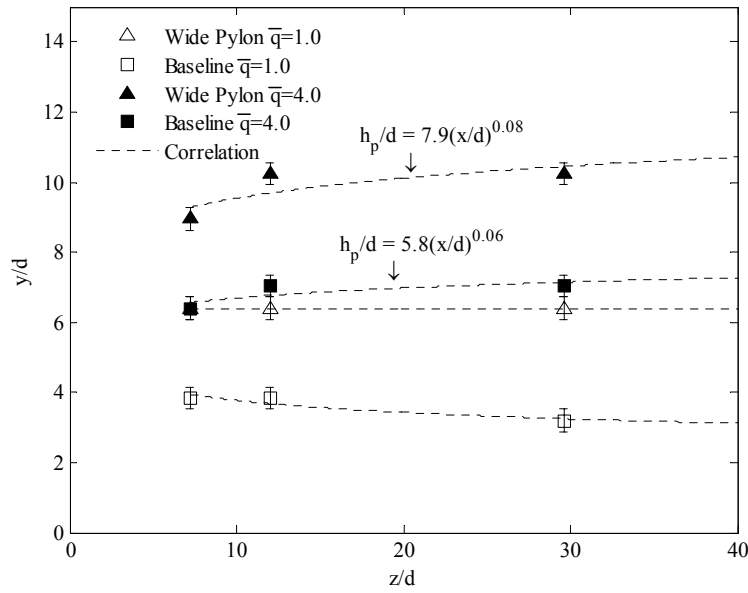


Figure 44. Ethylene plume penetration trajectory

wide pylon's plume penetration rate of change seems slightly greater than the baseline.

The measured values are presented below in Table 8.

In the same manner, the core penetration (h_c/d) trajectory is determined. Power law correlations are made to obtain rate of change information for each configuration. Figure 45 shows the core penetration trajectory for the wide and baseline configurations at $\bar{q} = 1.0$ and 4.0 with their respective correlations. Once again, discontinuity in the penetration heights appears in the near-field. The wide configurations at both \bar{q} values penetrate the

fuel plume core the highest at all streamwise locations. Both trajectories for the low \bar{q} case have values of n of either zero or slightly negative, therefore, their power-law equations are not shown. Correlation equations are shown for the $\bar{q} = 4.0$ cases. The most striking feature is the order of magnitude increase in core penetration seen in the wide pylon over the baseline in the high \bar{q} case. This indicates that the plume core for the high \bar{q} wide pylon case is migrating upward inside the fuel plume. This drift is also noticed by visual observation of Figure 39. Measured data for the plume core are presented in Table 8.

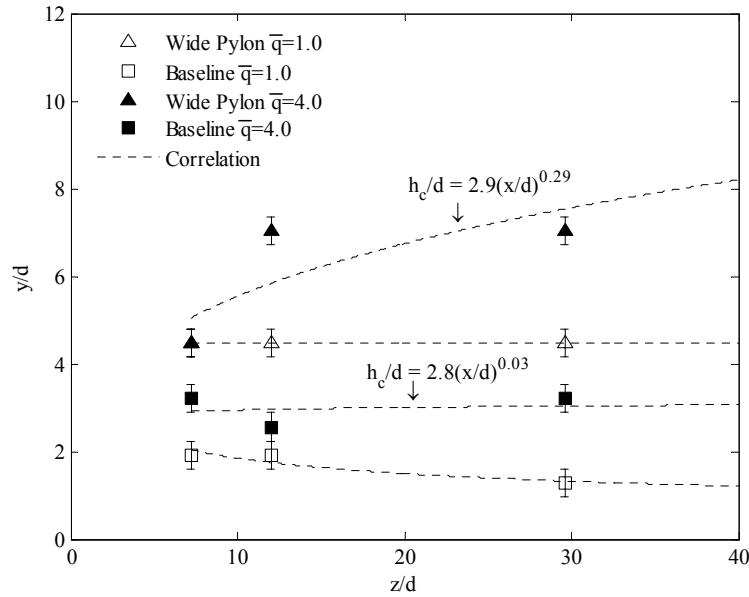


Figure 45. Ethylene plume core penetration trajectory

Overall, the low \bar{q} cases' lack of noticeable plume and core penetration increase shows that the injected jet momentum is no longer able to force the fuel further into the freestream. The added jet momentum in the $\bar{q} = 4.0$ cases allow the fuel plume to continue penetrating for both the wide and baseline configurations.

Table 8. Plume penetration trajectory for the wide and baseline inserts

		x/d (-)		
		7.2	12.0	29.6
Baseline h_p/d (-)	$\bar{q} = 1.0$	3.84	3.84	3.20
	$\bar{q} = 4.0$	6.40	7.04	7.04
Wide pylon h_p/d (-)	$\bar{q} = 1.0$	6.40	6.40	6.40
	$\bar{q} = 4.0$	8.96	10.24	10.24
Baseline h_c/d (-)	$\bar{q} = 1.0$	1.92	1.92	1.28
	$\bar{q} = 4.0$	3.20	2.56	3.20
Wide pylon h_c/d (-)	$\bar{q} = 1.0$	4.48	4.48	4.48
	$\bar{q} = 4.0$	4.48	7.04	7.04

5.4.3. Decay of Maximum Equivalence Ratio

The values of Φ_{max} for each configuration give an idea of the distribution of fuel within the plume. Since the same amount of mass is injected for a given value of \bar{q} regardless of injector configuration, a smaller value of Φ_{max} indicates better fuel-air mixing than a larger value. Hence, Table 9 gives a general view of fuel mixing. Each configuration's Φ_{max} is given at $x/d = 12$. At both values of \bar{q} , all pylons have a lower value of Φ_{max} compared to the baseline. This indicates that the pylons disperse the fuel core better than the baseline at this given location. The best performer at $x/d = 12$ is the tall pylon, with the lowest value of Φ_{max} . The tall pylon's increase in fuel core dispersal may be in part due to the pylon's height stretching out of the fuel plume, and the proximity of the fuel plume core inside the counter-rotating vortices for the high \bar{q} case.

Table 9. Maximum equivalence ratios for configurations

		x/d (-)		
		7.2	12.0	29.6
Baseline ϕ_{max} (-)	$\bar{q} = 1.0$	4.99	3.46	1.65
	$\bar{q} = 4.0$	12.73	7.30	3.36
Wide pylon ϕ_{max} (-)	$\bar{q} = 1.0$	4.63	3.07	1.53
	$\bar{q} = 4.0$	10.67	7.07	3.55
Medium pylon ϕ_{max} (-)	$\bar{q} = 1.0$	-	2.62	-
	$\bar{q} = 4.0$	-	6.17	-
Tall pylon ϕ_{max} (-)	$\bar{q} = 1.0$	-	2.22	-
	$\bar{q} = 4.0$	-	5.67	-

It is also expected that for an increase in downstream distance from the injection source, the fuel plume deteriorates and becomes increasingly mixed with the surrounding air. Therefore, a decrease in ϕ_{max} with x/d is expected. The rate at which this occurs can be used as a figure of merit for mixing effectiveness. Generally, the decay of maximum concentration with downstream distance proceeds exponentially,³² therefore, power law correlations can be made. A larger overall rate of decay is desirable and is indicated by a larger, negative value for n . The average rate of decay of -0.8 for jets in a crossflow³² compares well with the rates in this report. Figure 46 shows the decay of maximum equivalence ratio with downstream distance for the wide and baseline configurations. The data are presented with a logarithmic scale on both the vertical and horizontal axes. Error bars are not shown due to their small relative size. At $\bar{q} = 1.0$, there is no significant

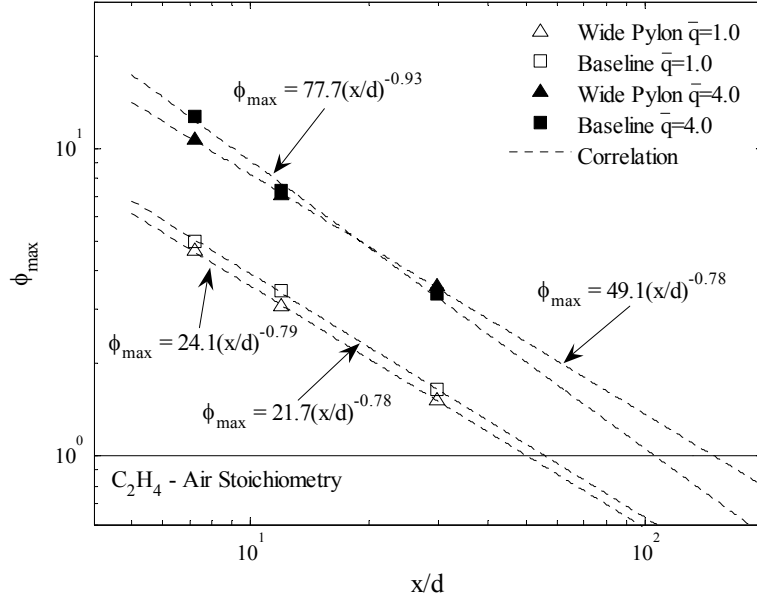


Figure 46. Maximum equivalence ratio decay vs. axial distance for wide and baseline inserts

difference in the decay rate of the wide and baseline configurations, both values of n are at approximately -0.78. When \bar{q} increases to 4.0, the rate of decay for the wide pylon stays about the same, while the rate for baseline increases to about -0.93. Note that for the high \bar{q} case, a transition between the wide's faster near-field mixing and the baseline's faster far-field mixing occurs at $x/d \approx 20$. This is due to the wide pylon's initially lower fuel concentration and the baseline's greater rate of concentration decay.

Typically, once the maximum concentration of a fuel reaches stoichiometric conditions, the injectant is considered fully mixed³²; the entire fuel plume is at or below the composition needed for total combustion. For this reason, a straight line at stoichiometric Φ is drawn on the figure. The fully mixed distance, x_{fm} , is desired to be small and is a factor of both rate of concentration decay and initial magnitude of Φ . For low \bar{q} , x_{fm} is

approximately $50d$ and $60d$ for the wide pylon and baseline respectively. At the high \bar{q} condition, x_{fm} increases to about $150d$ and $110d$ for the wide pylon and baseline respectively. These values for high injection pressure are at the same order of magnitude as the historical x_{fm} trend of approximately $200d$.³²

The accepted practice of determining a flow to be fully mixed once the maximum concentration of fuel reaches stoichiometric is perhaps not the best gauge of a specific fuel's mixing for combustibility (although it does give a fixed point of comparison to previous research done with varying fuel types). Typically, most hydrocarbon fuels burn at concentrations above stoichiometric. It may be prudent to establish how far downstream it takes for a plume's maximum concentration to reach the upper flammability limit (Φ_U) for a specific fuel. The published value of Φ_U for an ethylene-air mixture at standard temperature and pressure is 5.5.⁵⁴ The distance required for an ethylene plume's maximum concentration to reach Φ_U , is termed in this report as the flammable mixture distance x_{flam} . In other words, after x_{flam} , the entire plume is at or below the concentration of fuel required for combustion. At $\bar{q} = 1.0$, the value of x_{flam} for the wide and baseline configurations about $1d$ and $2d$ respectively, almost immediately after injection. This low value for x_{flam} is because of the low amount of mass being injected into the freestream. At $\bar{q} = 4.0$, the value of x_{flam} for each the wide and baseline configurations is almost identical at approximately $20d$.

Both the wide and baseline configuration's decay of maximum equivalence ratio are comparable at each respective injection pressure. For $\bar{q} = 1.0$, both configurations' rate of decay are similar, with the wide pylon holding a slight if almost insignificant advantage in values for x_{fm} and x_{flam} due to its initial lower overall magnitude in concentration. Despite

the baseline's better decay rate at $\bar{q} = 4.0$, the superior near-field mixing of the wide pylon allows for analogous values for both x_{fm} and x_{flam} . It may be observed that the rate of max concentration decay appears related to the strength of the vortex pair. Note that as \bar{q} increased, the wide pylon's value for n remains fairly constant, while n for the baseline became more negative. This may be due to the fact that the baseline's fuel plume is located within the vortex pair, which aids mixing, while the wide pylon's plume lies above the vortices for both injection pressures.

5.4.4. Plume Area

Total plume area (A_p) is determined from the definition of the plume edge, where the plume is the area encompassing the outermost contour at $\Phi = 0.2$. Another useful area used in this report is the flammable plume area (A_f), where A_f is defined as the area of the plume that has fuel concentration between the published upper and lower flammability limits of ethylene in air at standard temperature and pressure ($\Phi_U = 5.5$ and $\Phi_F = 0.4$ respectively, but a 10% buffer is added to narrow the limits used in the research to 5.0 and 0.36 to account for variation).⁵⁴ This figure of merit represents the area of the fuel plume that is in the proper concentration for combustion. Comparisons are made for both A_f and A_p in all configurations at an x/d of 12. Plume spreading is determined for the wide and baseline inserts as the change in both A_f and A_p with downstream distance. As performed in previous sections, the trajectory analysis uses measurements at x/d of 7.2, 12 and 29.6. As before, all data are determined at both $\bar{q} = 1.0$ and 4.0. Error bars are not shown due to their small relative size.

5.4.4.1. Plume Area Comparison

Figure 47 shows the total and flammable plume areas (A_p and A_f) normalized by the injection port area A_i for all test cases at $x/d = 12$. At low \bar{q} , all pylons demonstrate approximately the same total and flammable area. The baseline configuration shows a noticeably larger A_p compared to the pylons. However, when comparing A_f , the difference between the baseline and the pylon configurations is not as significant since more of the baseline plume is not within the flammability limits than the other configurations. Both the baseline and tall configurations appear to have slightly larger flammable plume areas than the wide and medium pylons, however, this increase is not substantial enough to deem either the baseline or tall configurations as superior at this streamwise station.

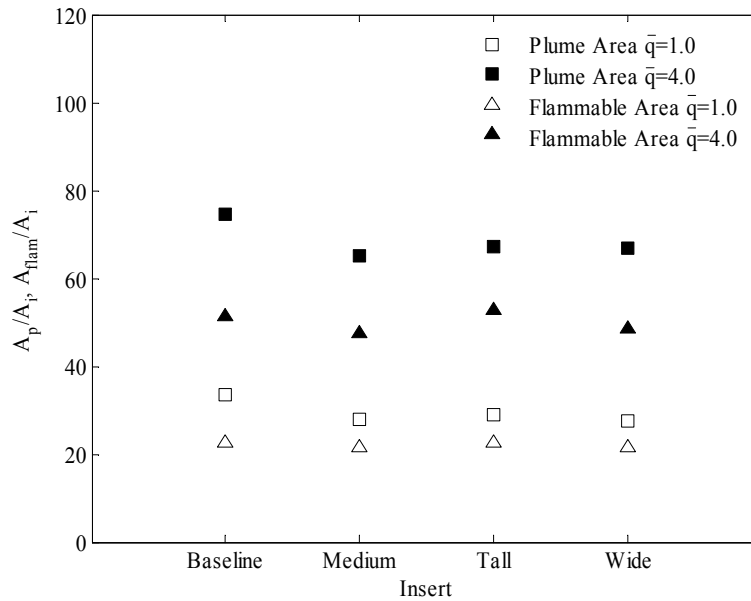


Figure 47. Total (A_p) and flammable plume (A_f) area comparison for all inserts at $x/d = 12$

Table 10 gives the percentage of the fuel plume that is flammable. These values were determined from the following simple equation:

$$FPP = \frac{A_f}{A_p} \times 100\% \quad (33)$$

where

$$FPP = \text{Flammable Plume Percentage (\%)}$$

A higher percentage is desirable and indicates higher fuel plume combustibility and better plume mixing. However, values for *FPP* should be examined with overall plume areas in mind, since the percentages do not give indication of plume size. Pylons show a noticeable *FPP* percent difference of about 15% greater than the baseline at the low injection pressure setting, but do not seem to differ significantly from one another. At the higher injection

Table 10. Flammable plume percentage for each configuration at $x/d = 12$

	% Difference over Baseline		
	$\bar{q} = 1.0$	$\bar{q} = 4.0$	$(\bar{q} = 1.0 / \bar{q} = 4.0)$
Baseline <i>FPP</i> (%)	68	69	—
Medium <i>FPP</i> (%)	78	73	14.7 / 5.8
Tall <i>FPP</i> (%)	78	78	14.7 / 9.0
Wide <i>FPP</i> (%)	78	73	14.7 / 5.8

pressure, the wide and medium pylons' values of FPP decreases to similar percentages seen in the baseline (which remains about constant). The tall pylon's FPP remains around 10% higher than the baseline.

Overall, all configurations demonstrate similar plume area size. The baseline's A_p is the highest in both injection pressure cases since its proximity to the cavity causes an extensive amount of fuel to become entrained within. However, when considering A_f , very little difference is noticed between the test cases. This is apparent when viewing the baseline's values for FPP . These values are noticeably less than the values for the pylons, indicating that the fuel entrained within the cavity is in insufficient concentration to allow for combustion. At $\bar{q}=1.0$, values for A_f higher than the medium and wide are apparent in both the baseline and tall cases since their plume cores are within the counter-rotating vortices. The variable which had the strongest effect on total and flammable plume sizes regardless of configuration is injection pressure, which caused significant increases in plume sizes with increasing \bar{q} .

5.4.4.2. Plume Spreading

As axial distance from the injection port increases, the plume is expected to dissipate and enlarge. This causes increases in both A_p and A_f . This section compares spreading of A_p and A_f with downstream distance for both the baseline and wide inserts. Figure 48 and Figure 49 show the total plume area (A_p) and flammable plume area (A_f) spreading respectively for the two configurations taken at axial locations of $x/d = 7.2$, 12 and 29.6. As in previous trajectory plots, a power law correlation of the form seen in Equation 32 is added to each case. Plume spreading trajectories for A_p given in Figure 48

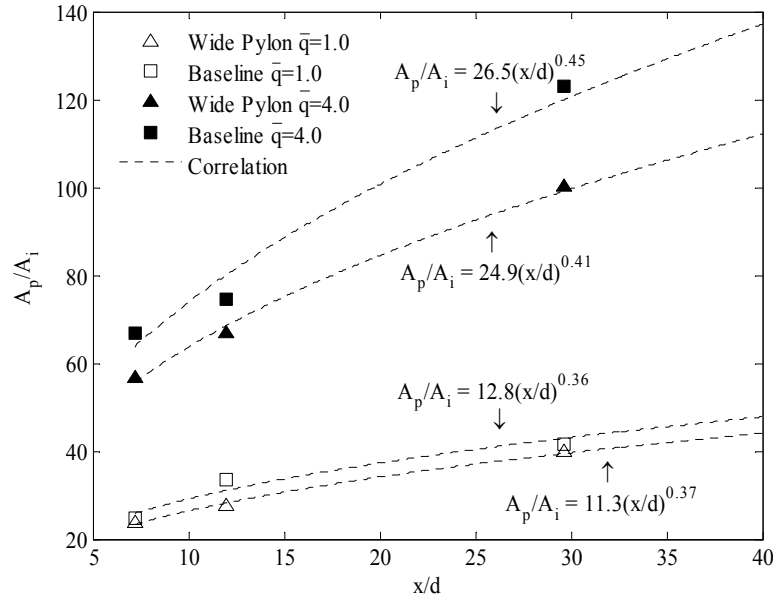


Figure 48. Total plume area (A_p) trajectory for baseline and wide inserts

show that for both injection pressures, the baseline configuration has increased spreading compared to the wide pylon over the region tested. At low \bar{q} , baseline A_p has a greater magnitude, but similar spreading rates to the wide. When \bar{q} is increased to 4.0, both the magnitude and spreading rates are increased in both configurations. At the higher injection pressure, the baseline shows better overall magnitude and spreading rate compared to the wide. Trajectories of A_f shown in Figure 49 display similar trends to those seen for A_p . At both injection pressures, the baseline cases demonstrate larger magnitudes of A_f at each axial location and spreading rates compared to the wide. With increasing injection pressure, a positive change in both A_f and n is noticeable. It is also interesting to note that for both low \bar{q} configurations, rate of spreading of A_f is less than the rate of spreading of A_p . This suggests that most of the plume is spreading in concentrations outside of the flammability limits. The opposite is seen in the high \bar{q} cases; the rates of

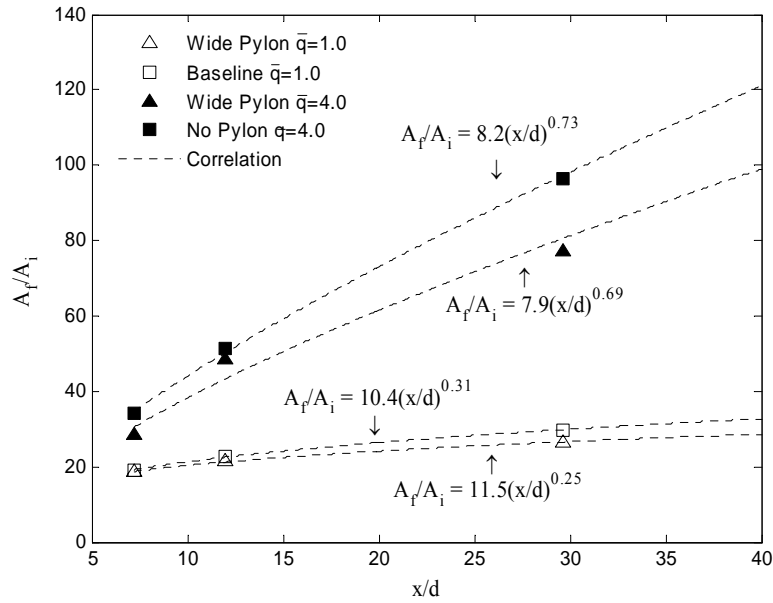


Figure 49. Flammable plume area (A_f) trajectory for baseline and wide inserts

flammable plume spreading are greater than the rates of total plume spreading, indicating that the plume's fuel is mixing into concentrations within the upper flammable limit faster than in the total plume is spreading.

Flammable Plume Percentages, or *FPP*, are given in Table 11 below for the wide and baseline cases at the three axial stations tested. Profiles of *FPP* variation with downstream location are evident in the table and are different for each configuration.

Table 11. Flammable plume percentage for baseline and wide inserts

		$x/d (-)$		
		7.2	12.0	29.6
Baseline <i>FPP</i> (%)	$\bar{q} = 1.0$	77	68	71
	$\bar{q} = 4.0$	51	69	78
Wide pylon <i>FPP</i> (%)	$\bar{q} = 1.0$	78	78	66
	$\bar{q} = 4.0$	50	73	77

Drops in percentage downstream indicate a larger rate of spreading for A_p than for A_f as evident in both inserts at low \bar{q} . The wide pylon's FPP remains at a higher value further downstream before decreasing. For the high \bar{q} cases, an opposite, increasing trend in FPP values is apparent. The rise in percentage with axial location indicates lower rates of spreading for A_p than for A_f . Values for FPP are similar for both configurations for a given \bar{q} , indicating that the pylons have little effect on FPP .

Overall, the baseline configuration at both injection pressures displays better total and flammable plume spreading than the wide pylon configuration. This may be due in part to the baseline cases' fuel plume being located within the vortex pair, which aids in mixing and spreading. As injection pressure increases, the magnitude and rate of spreading of A_p and A_f increases, indicating that increasing \bar{q} has a favorable effect on plume spreading. Additionally, at high \bar{q} , A_f 's rate of spreading is greater than that of A_p for both configurations. At low \bar{q} , A_f 's rate of spreading is less than that of A_p . This may be seen when examining the equivalence ratio contours in Figure 38 and Figure 39. As axial distance increases the fuel within the plume disperses. For low \bar{q} (lower mass injected), at $x/d = 7.2$, the maximum equivalence ratio within the plumes starts below Φ_U . Therefore, as the plume fuel dissipates and mixes, fuel concentration drops below Φ_L without any new fuel added. For the high \bar{q} cases at the same axial location, the maximum equivalence ratio starts above Φ_U , so as fuel dissipates below Φ_L , fuel at high concentrations is also mixing into flammable limits at a higher rate. Eventually, the maximum equivalence ratio for high \bar{q} cases will eventually drop below Φ_U . Once this occurs, both injection pressures' area spreading rates may be similar.

5.4.5. Mixing Efficiency

Mixing efficiency, η_m is given as the ratio of the mixed fuel mass flow rate, $\dot{m}_{f,mixed}$, to the total fuel mass flow rate, $\dot{m}_{f,total}$, where a mixed fuel has a mass concentration at or below stoichiometric. The definition used here for mixing efficiency is developed by NASA and presented in the form given by Fuller et al.^{29,55} In a fuel-rich region, all local air is considered mixed, the opposite is true for fuel-lean regions. For the case of a single injector in a relatively large test section, the flow is described as fuel-lean allowing the definition of mixing efficiency to be as follows.

$$\eta_m \equiv \frac{\dot{m}_{f,mixed}}{\dot{m}_{f,total}} = \frac{\int X_r \rho u dA}{\int X \rho u dA} \quad (34)$$

and

$$X_r \equiv \begin{cases} X & X \leq X_{stoich} \\ \frac{1-X}{1-X_{stoich}} X_{stoich} & X > X_{stoich} \end{cases} \quad (35)$$

where X is *fuel mass fraction*, A is the *fuel plume area* and subscript *stoich* represents *stoichiometric*. A value of $\eta_m = 0$ corresponds to a perfectly segregated jet, while $\eta_m = 1$ corresponds to a perfectly mixed system. Therefore, a higher value of η_m is desirable and indicates more efficient mixing compared to a lower value. Values for η_m are presented below in Table 12 for each configuration at both injection pressures at $x/d = 12$. All pylons achieve at least slight increase in η_m over the baseline at the low \bar{q} condition. However, these increases are almost negligible when error is taken into consideration. The tall and wide pylons appear to be the best performer over the baseline, with slight improvements in

η_m . As \bar{q} increases, mixing efficiency drops significantly across all configurations. The pylons actually demonstrated lower η_m compared to baseline, with the wide and medium pylons' η_m closest to that of baseline.

Table 12. Mixing efficiency (η_m) for all configurations at $x/d = 12$

	$\bar{q} = 1.0$		$\bar{q} = 4.0$		% Difference over Baseline ($\bar{q} = 1.0 / \bar{q} = 4.0$)
Baseline $\eta_m (-)$	0.743	± 0.032	0.470	± 0.020	—
Medium $\eta_m (-)$	0.745	± 0.032	0.443	± 0.019	0.3 / -5.6
Tall $\eta_m (-)$	0.795	± 0.034	0.463	± 0.020	7.1 / -1.5
Wide $\eta_m (-)$	0.789	± 0.033	0.478	± 0.021	6.2 / 1.6

Mixing efficiencies remain fairly constant across all insert configurations. The better penetration of the fuel plume may help enhance η_m for the pylons, while the increased effect of the vortex pair may aid the baseline case (especially at the high \bar{q} condition). These physical effects may balance out and help equalize mixing efficiency between the configurations. It should be noted that these results compare relatively well with the flammable plume areas seen in Figure 47.

5.5. Aerodynamic Loss Analysis

5.5.1. Overview

Quantifying aerodynamic losses is defined within as total pressure loss and momentum loss. Total pressure losses are determined from total pressure contours and a total pressure loss coefficient. Momentum losses are determined from observations of Mach number contours. The following sections discuss and compare total pressure and Mach number contours for each configuration at $x/d = 12$. The raw cone-static and pitot pressure as well as reduced static pressure data is presented in Appendix F

5.5.2. Total Pressure Contours

Figure 50 gives the normalized P_t contours at an axial location of $x/d = 12$ for all eight conditions tested. Normalization is done against the tunnel plenum pressure, which represents the total pressure upstream of the combustor section. The axes are aligned in the same manner seen in the species concentration contours. The spatial range varies from $-8 \leq z/d \leq 8$ and $0 \leq y/d \leq 9$. Contour color bars are scaled consistently to aid in plot-to-plot comparisons. The bow shock is seen as a curved contour under which the values for normalized total pressure are less than 1.0. For this analysis, the region of interest is the area beneath the shock.

The baseline $\bar{q} = 1.0$ and 4.0 cases are shown in Figure 50 a) and b) respectively. The location of the fuel plume is evident by the region of low pressure penetrating into the freestream. The surrounding low total pressure region is due to the counter-rotating vortices transferring kinetic energy into the transverse direction. Because of the low

resolution, the vortex structures are unidentifiable, but their overall effect of lowering total pressure can be clearly seen. The region of low total pressure near the bottom of the figure is due to diffusion of the lower momentum fluid from the cavity. Notice in the high \bar{q} case, the asymmetric quality of the jet plume is evident, and increased total pressure loss occurs in the left lobe (left side of centerline) where a higher fuel concentration is present. Also apparent in the high \bar{q} case, total pressure losses penetrate further into the flow. Overall, greater pressure recovery is evident in the low \bar{q} case.

The medium pylon is seen in Figure 50 c) and d). Similar physical features are apparent in the medium configurations as seen in the baseline. Higher fuel plume penetration brings total pressure loss upward into the flow, but the gradients are less severe since the losses are distributed further. Again, as injection pressure increases, the plume losses encompass a greater area and there is less total pressure recovery.

The tall pylon's P_t contours, are shown in Figure 50 e) and f). The increased height of the pylon penetrates the flow losses into the core flow higher than the medium pylon, but seem to distribute P_t losses better than the medium. As injection pressure increases, bow shock strengthens, and losses penetrate further into the flow. However the losses are unevenly distributed, with the majority of the losses being concentrated near the bottom of the pylon. This occurrence is most likely due to the lower location of the fuel plume core within the counter-rotating vortices.

The total pressure losses for the wide pylon, shown in Figure 50 g) and h), are very similar to those seen in the medium pylon, due to their similar geometry. It appears that the added width of the wide pylon slightly widens the total pressure loss distribution.

By visual observation of Figure 50, the pylons do not appear to greatly improve total pressure recovery compared to the baseline in the area below the bow shock. The pylons do appear to distribute the losses into the flow more effectively than the baseline due to their increased plume penetration.

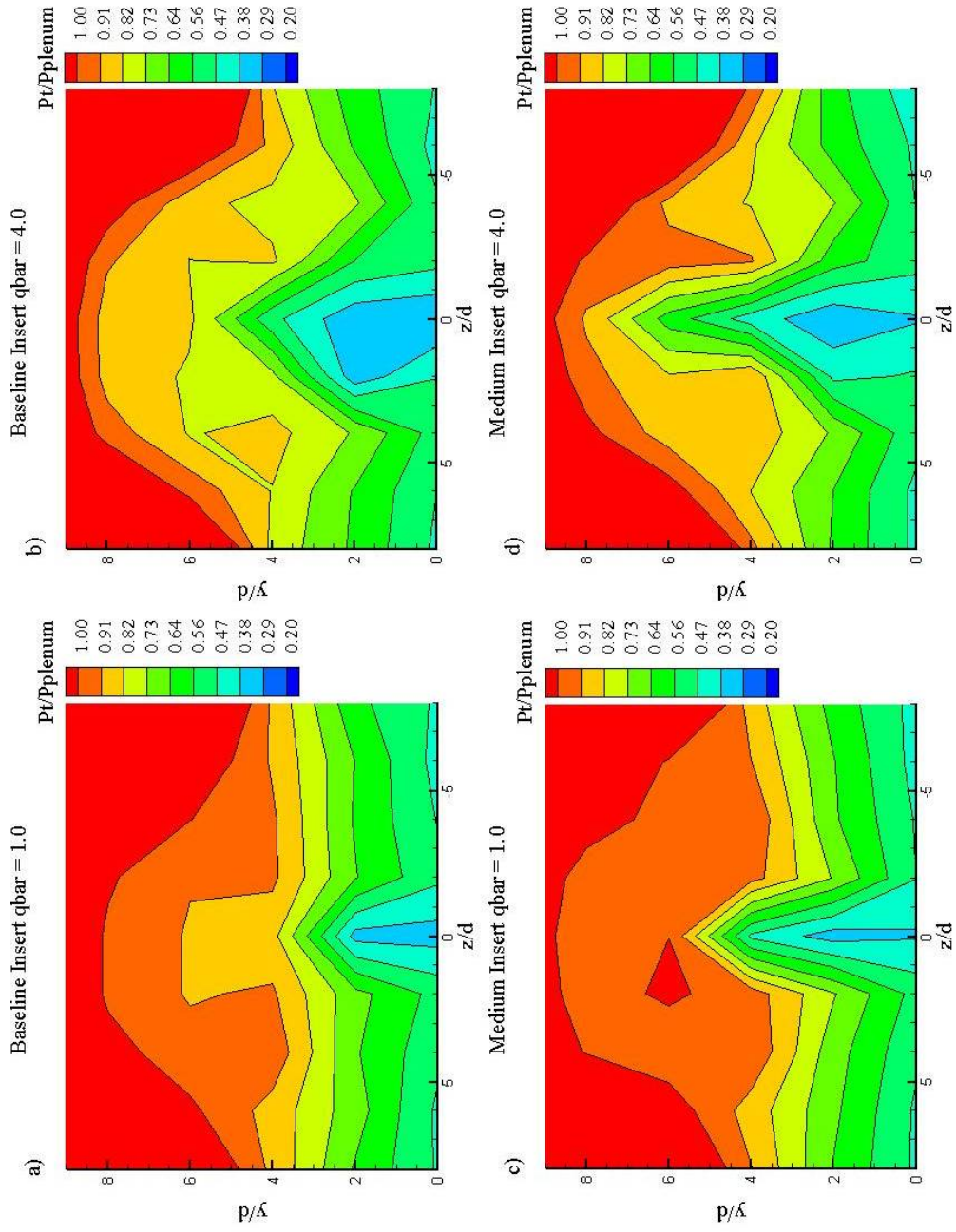


Figure 50. Normalized total pressure contours at $x/d = 12$

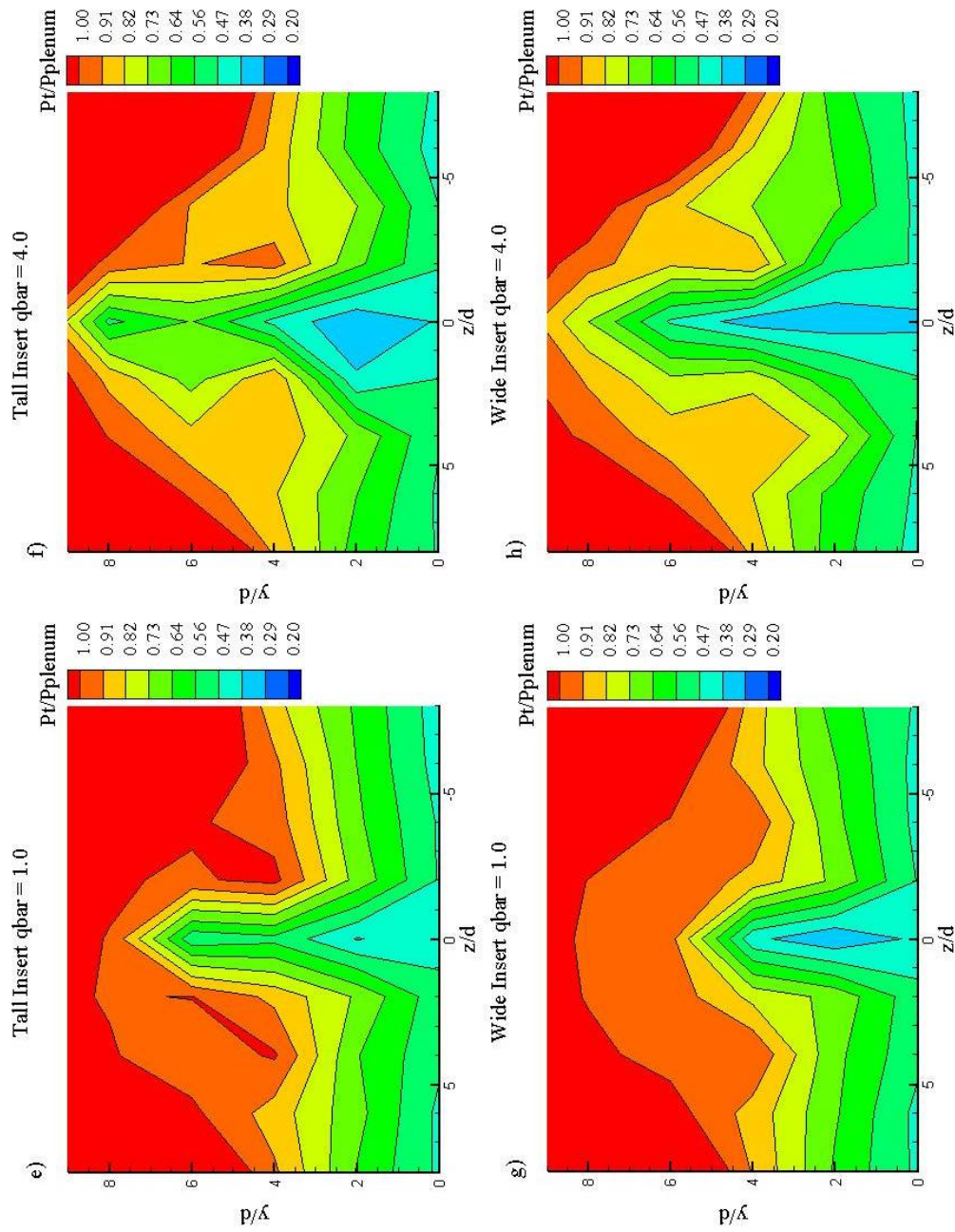


Figure 50. cont Normalized total pressure contours at $x/d = 12$

5.5.3. Mach Number Contours

Momentum loss for each configuration may be quantified through observations of Mach number contours. The freestream Mach number is approximately 2.15. Momentum losses will manifest as lower than freestream Mach numbers. Therefore, for good recovery, it is desirable to have Mach numbers as close to freestream as possible. Since total pressure changes proportional to velocity for a given static pressure, Mach profiles are expected to be similar to those seen for total pressure. Figure 51 give the Mach contours for all four insert configurations at both injection pressures. All data shown in the plots is taken at $x/d = 12$ and have the same data range as the total pressure contours. Like the pressure plots in Figure 50, the color scale varies from the lowest to freestream Mach number and is constant across all configurations for ease of comparison. The area of interest is again the bow shock where Mach numbers are below freestream.

Figure 51 a) and b) show the baseline cases' Mach contours for $\bar{q} = 1.0$ and 4.0 respectively. The plume's affect on momentum is visible as an area of low Mach number near the bottom of the figures. The local minima at the center of the plume signify fluid that went through the Mach disk. Notice that the losses near the cavity are not apparent in the Mach contours as they are in the total pressure contours. The highest losses generally remain in the area immediately around the fuel plume, with Mach numbers of the air surrounding the plume varying between approximately 1.7 and 2.0. It is readily apparent that losses increase with increasing injection pressure as Mach number in the flow surrounding the plume appear lower at the $\bar{q} = 4.0$ case.

The medium cases are shown in Figure 51 c) and d) and show increased penetration of losses due to the pylon's presence for both \bar{q} . As injection pressure increases, the area of low Mach number within the plume remains relatively the same size, however, greater Mach number reduction is evident in the flow around the plume compared to low injection pressure case. Compared to baseline, the medium pylon high injection case appears to localize the low Mach flow better and have higher Mach numbers in the region surrounding the plume.

The tall pylons cases for high and low injection pressure are shown in Figure 51 e) and f) respectively. Increased penetration of low Mach number flow is evident for both injection pressures compared to baseline and the low Mach values are not as concentrated near the cavity. Mach number profiles similar to those found in the baseline case surround both the high and low \bar{q} plumes. Overall, the tall pylon's high \bar{q} case appears to have higher Mach number reduction and higher penetration of losses in the region of interest compared to the low \bar{q} case. It is also apparent that losses are greater than in the medium configuration.

Figure 51 g) and h) give the Mach number contours for the wide pylon's high and low \bar{q} cases respectively. At low \bar{q} , Mach number reduction is very comparable to the medium pylon. This observation is consistent in both the plume and the region surrounding except for a small area of low Mach in the plume center. Penetration of Mach loss due to the fuel plume is higher compared to the baseline, similar to the medium pylon and lower than the tall pylon for both \bar{q} . Comparing the wide pylon's two injection pressure cases reveals higher penetration of Mach loss within both the fuel plume and the surrounding region for the high \bar{q} condition, consistent with observations for other configurations. Of

all the pylons, the wide plume's Mach numbers are the lowest for both \bar{q} . However, no immediate difference is noticed in the Mach number profiles in the region surrounding the plume when comparing to the medium and tall pylons'.

Overall, the Mach number profiles for the pylons appear to have greater distribution of Mach number losses into the main flow compared to the baseline at both \bar{q} values. This is most apparent in the tall and wide cases. The two tall cases have the greatest penetration and distribution of Mach number loss of all the configurations; this is obviously due to the larger size of the pylon and increased fuel plume penetration. The wide cases seem to have the most localized concentration of Mach losses within the plume. In the regions surrounding the plumes, the pylons seem to retain higher Mach numbers compared to baseline at both injection pressures. When varying injection pressure, it is readily apparent that the increased plume turbulence and bow shock strength contribute to greater Mach loss in the high \bar{q} case. This observation is constant across all inserts.

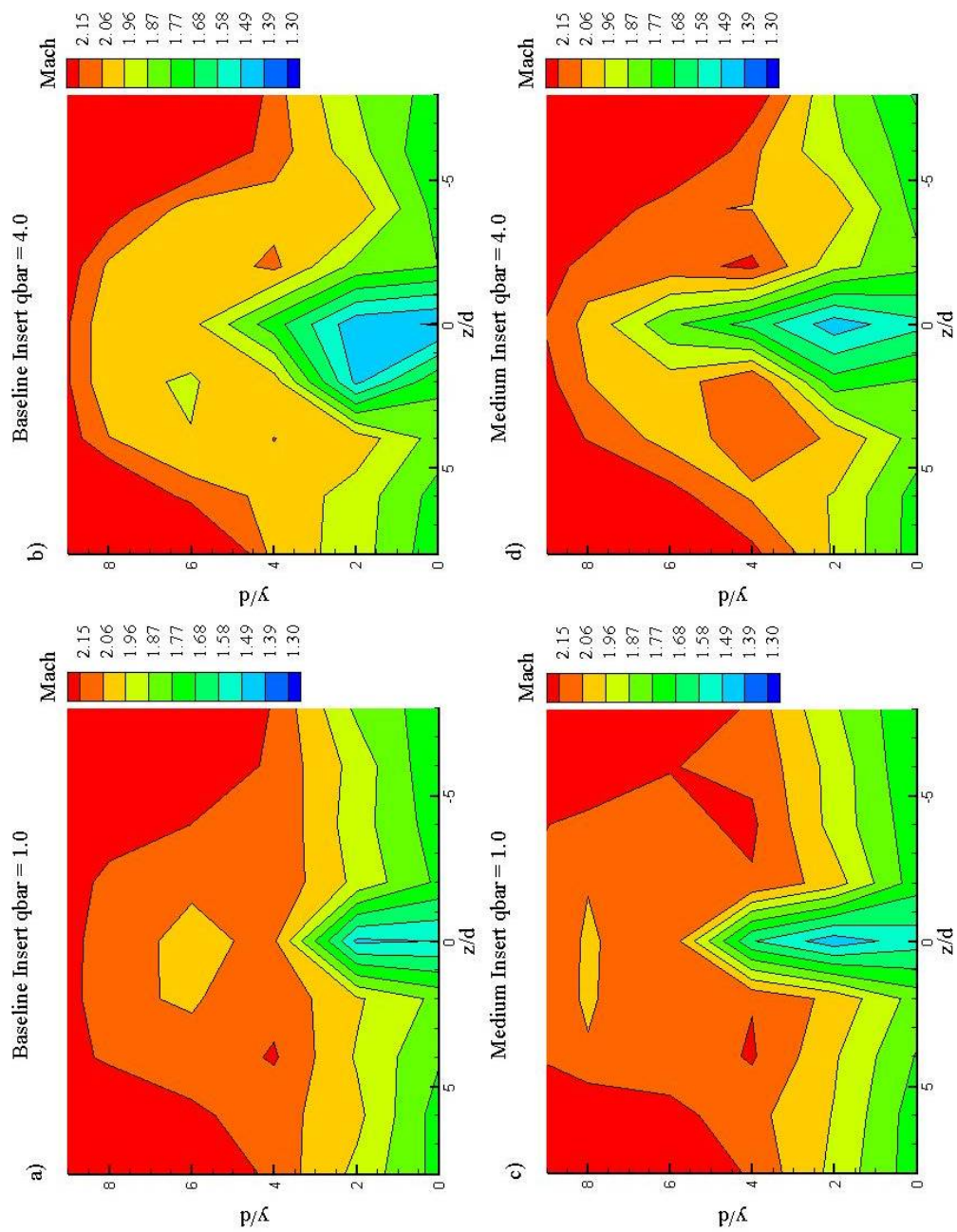


Figure 51. Mach number contours at $x/d = 12$

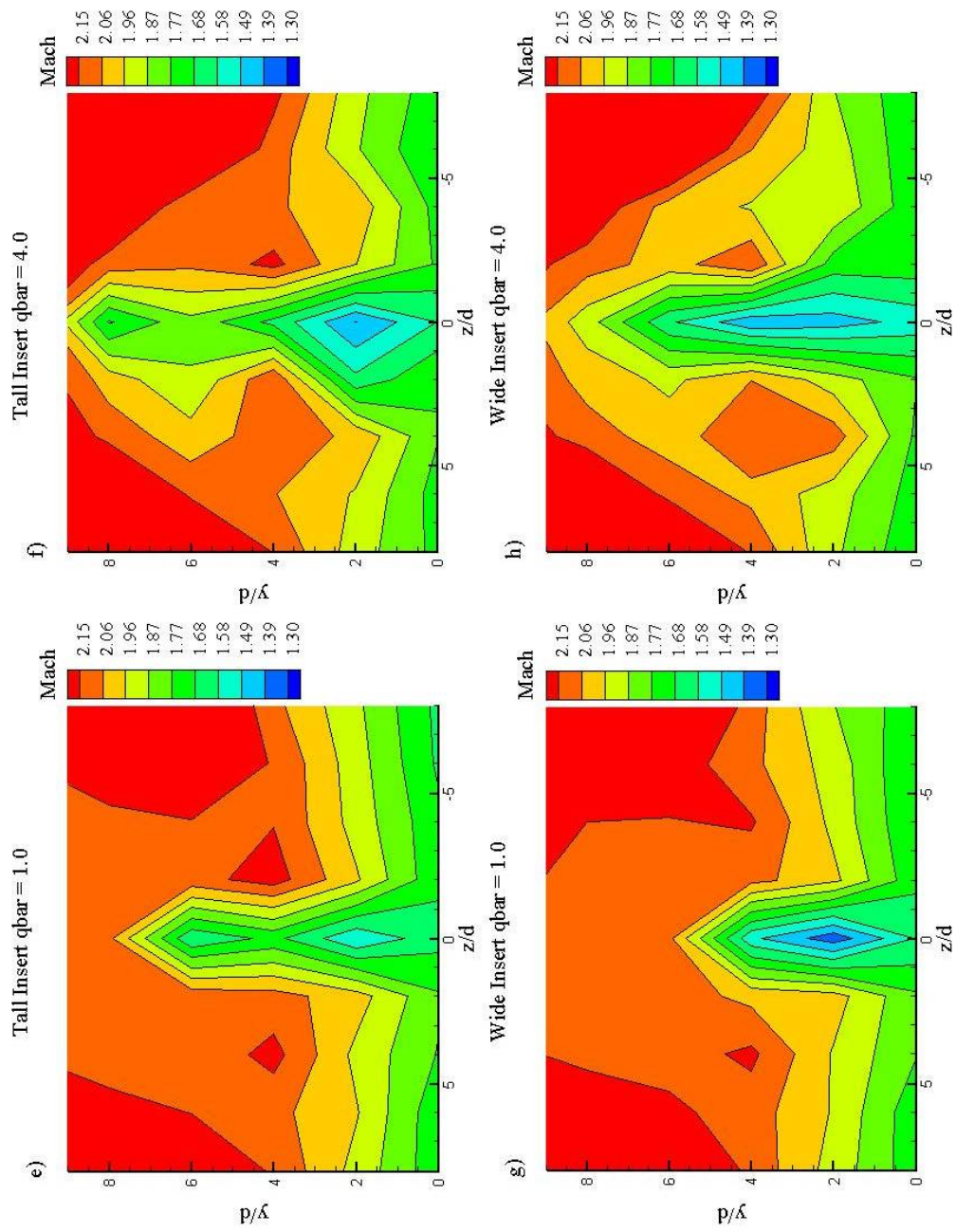


Figure 51. cont Mach number contours at $x/d = 12$

5.5.4. Total Pressure Loss Coefficient

The total pressure loss coefficient, defined as $\bar{\omega}$ provides a mass-averaged fraction of total pressure loss for a given field and is represented in the equation below.

$$\bar{\omega} = 1 - \frac{\bar{P}_t}{P_{t_{ref}}} \quad (36)$$

Where \bar{P}_t is the *mass-averaged total pressure* for a region of interest and $P_{t_{ref}}$ is the *measured tunnel plenum pressure*. Values for \bar{P}_t may be found using the equation below.

$$\bar{P}_t = \frac{\int P_t \rho u dA}{\int \rho u dA} \quad (37)$$

This definition allows for the local impact of flow momentum through an area. An $\bar{\omega} = 1$ means complete P_t loss and $\bar{\omega} = 0$ denotes no P_t loss. Therefore, a small value for $\bar{\omega}$ is desired. Mass averaging is performed across a cross section consistent for all configurations. The cross section spans from $-8 \leq z/d \leq 8$ and varies in the transverse coordinate to avoid the effect of the bow shock and ensure capture of the plume. At the edges of the cross section, the transverse coordinate varies from $0 \leq y/d \leq 6$ and $0 \leq y/d \leq 6$ at the centerline. Table 13 gives values of $\bar{\omega}$ for each configuration at $x/d = 12$.

Additionally, the table presents the percent difference between the pylon configurations and the baseline. In the low injection pressure cases, $\bar{\omega}$ remains fairly consistent. All pylons have increased total pressure loss compared to the baseline at $\bar{q} = 1.0$. The most sizeable increase at this injection pressure occurs in the tall and wide configurations, as the pylons have larger cross-sectional areas compared to the medium and baseline inserts.

However, those differences in losses are negligible when error is taken into account. As

\bar{q} increases to 4.0, the pressure losses increase. This is to be expected when viewing both the shadowgraphs and total pressure contour plots. The increased plume area and momentum strengthens the bow shock and introduces larger regions of total pressure reduction into the flow. Most pylon's $\bar{\omega}$ are actually reduced compared to baseline. Again taking into account uncertainty, the tall and wide pylons show little change compared to the baseline, only the medium pylon shows sizeable decrease in pressure loss compared to baseline.

Table 13. Total pressure loss coefficient ($\bar{\omega}$) for all configurations at $x/d = 12$

	$\bar{q} = 1.0$		$\bar{q} = 4.0$		% Difference over Baseline ($\bar{q} = 1.0 / \bar{q} = 4.0$)
Baseline $\bar{\omega}$ (-)	0.213	± 0.009	0.284	± 0.012	—
Medium $\bar{\omega}$ (-)	0.214	± 0.009	0.256	± 0.011	0.5 / -9.9
Tall $\bar{\omega}$ (-)	0.221	± 0.010	0.275	± 0.012	3.8 / -3.2
Wide $\bar{\omega}$ (-)	0.223	± 0.010	0.293	± 0.013	4.7 / 3.2

Overall, values for $\bar{\omega}$ indicate little change in the pylon's total pressure losses in comparison to the baseline. The best performer appears to be the medium pylon being the only configuration with notable decrease in total pressure loss at the high injection pressure condition, and the configuration with the smallest calculated percent difference increase in $\bar{\omega}$ at the low injection pressure.

6. Conclusions and Recommendations

6.1. *Experiment Overview*

Experimental research was conducted with the goal of comparing the performance of pylon-aided transverse injection with transverse injection without a pylon. All tests were conducted in a Mach 2 flow to simulate the environment inside a scramjet combustor section. Three pylon and one no pylon configurations were tested at two injection pressures. The extent of the investigation dealt with mixing potential and supersonic losses. Mixing was characterized by fuel penetration, maximum plume equivalence ratio, plume area, and mixing efficiency. Furthermore, qualitative treatment of equivalence ratio contour plots allowed general observations into the mixing qualities produced by each configuration. Losses were parameterized by the total pressure loss coefficient. Total pressure and Mach contours allowed observations of losses seen in the flow field. Data for all configurations was taken at $x/d = 12$, additional species sampling data was taken at $x/d = 7.2$ and 29.6 for the wide and baseline configurations

6.2. *Synopsis of Results*

Shadowgraph images of the baseline condition indicated no shock structures in the vicinity of the injection port prior to injection. Once injection occurred, classic bow shocks formed and were lifted as injection pressure increased. For the pylon configurations bow

shocks formed at the pylon's trailing edge. When injection occurs the attached pylon shocks strengthen and lift. Increases in injection pressure in the pylon configurations corresponded with additional shock lifting and strengthening.

Equivalence ratio contour plots allowed general comments to be made on the fuel plume structures and fuel distribution. The baseline cases' fuel plumes were dominated by the presence of the two counter-rotating vortices. Pylons tended to demonstrate a three fuel lobe structure as their presence allowed further penetration of the fuel into the freestream. Counter-rotating vortices were apparently weakened due to pylon presence which may negatively impact mixing. Additionally, the medium and wide cases tended to lift the core of the plume higher out of the vortex pair, while the tall pylon's plume core remained within the vortices. As injection pressure increased, plume area and penetration increased and the vortex pair was strengthened in all configurations.

Fuel penetration was the most significant difference between the pylons and baseline configurations. Pylons increased h_p/d over baseline across all configurations. At low \bar{q} , the tall pylon had the highest percent difference over the baseline with an 83% increase in h_p/d . At high \bar{q} , the wide pylon had the highest percent difference over the baseline with 46%. Percent differences compared to baseline were even higher for h_c/d . At low \bar{q} , the tall pylon had the greatest change of 167% over the baseline's core penetration, while the wide pylon had the greatest change of 178% over the baseline at high \bar{q} . As injection pressure increased, h_p/d rose for both configurations; however the baseline appeared to be the most affected. Rise in injection pressure increased h_c/d in all configurations except for the tall, as the maximum equivalence ratio remained within the counter-rotating vortices. The medium configuration was a nominal performer for both

h_p/d and h_c/d . Comparison of h_c/d to previous research showed analogous penetration heights and allowed for a rudimentary correlation with NO-PLIF intensity and species concentration. Penetration trajectory comparison showed little change in rate of penetration with axial location between wide and baseline configurations.

Values for Φ_{max} were determined for all configurations. A low value of Φ_{max} was deemed a good indication of the configuration's ability to distribute fuel into the flow. All pylons demonstrated comparable values for Φ_{max} slightly lower than that of the baseline at $x/d = 12$. The tall pylon had the overall lowest value for Φ_{max} at both injection pressures, due most likely to its size's ability to increase penetration. Comparison was made in Φ_{max} decay between the wide and baseline. Fuel decay rates were comparable at each respective injection pressure and matched well to historical data. For $\bar{q} = 1.0$, both configurations' rate of decay are similar, the wide pylon demonstrates slightly lower values for x_{fm} and x_{flam} due to its initially lower overall magnitude in concentration. At $\bar{q} = 4.0$, the baseline configuration had a better decay rate; however superior near-field mixing in the wide configuration allowed for similar values for both x_{fm} and x_{flam} .

Comparison in A_p and A_f was made between the pylons and baseline at $x/d = 12$. Results showed that the baseline's A_p was greater than the pylons due to a higher rate of fuel entrainment into the high circulation regions of the cavity. However, all configurations demonstrated similar values for A_f , indicated little variation in mixing effectiveness. Trajectory data was again figured for the wide and baseline configurations. Rates of plume spreading were calculated for both A_p and A_f . Data showed that the baseline configuration displayed better total and flammable plume spreading than the wide; due in part to the majority of the baseline's fuel was located inside the vortex pair. An

increase in injection pressure had positive effects on area spreading rates. At high \bar{q} , flammable plume spreading rates were higher than total plume.

Values for mixing efficiency were found to be similar for all configurations at both injection pressures at $x/d = 12$. Slightly better values were found in the wide and tall configurations. For the conditions studied, injection pressure had a much greater impact on η_m than pylon configuration. At high injection pressure, the plume is much more structured and is not dominated by diffusive mechanisms.

Total pressure and Mach number contour plot observations were made for all configurations at $x/d = 12$. Losses appeared to be centralized around the fuel plume and spread throughout the flow field. Losses were comparable across all configurations. Injection pressure had the highest effect on total losses. A high injection pressure caused stronger bow shocks, lower Mach numbers and total pressure within the region around the plume. These observations were confirmed by values of $\bar{\omega}$ which were fairly similar at a given value of \bar{q} .

6.3. Conclusions of Research

All pylon configurations demonstrated better penetration and appeared to shift the fuel plume core higher compared to the baseline at both \bar{q} . The pylons lifted the fuel plumes higher above the cavity allowing better fuel dispersion into the main flow. While pylons demonstrated slightly lower values of maximum equivalence ratio, similar mixing effectiveness to the baseline was noticed. Pylon presence contributed to increased spreading, their weaker counter-rotating vortices had less of an impact on mixing. The

strength of the vortex pair was dictated by the amount of fuel entrained within. Pylon presence did not contribute to greater aerodynamic losses than the baseline; in fact, losses attributed to the pylons were similar to if not slightly better than those found in the baseline. Increase in form drag introduced by the pylons was offset by the highly oblique bow shock produced. Injection pressure held the strongest influence on both mixing and loss.

Due to its size and geometric shape the medium pylon proved to be a nominal performer in all aspects. It provided the lowest overall increase in penetration of all pylons, and displayed smaller (if similar) plume area sizes than the other pylons. It indicated similar total pressure and momentum losses when compared to the baseline, and no significant improvement was noticed.

The tall pylon demonstrated interesting mixing and loss traits. It provided the highest plume penetration at the low \bar{q} but its low fuel plume core location prevented a sizeable increase in penetration at the high \bar{q} case. However, the location of the plume core within the vortex pair aided mixing better than the other pylons. The larger size of the tall pylon did not appear to contribute significantly to drag.

The wide pylon provided the best overall mixing performance of all the pylons. While similar to the tall and medium, it did provide slightly better values for penetration (at high \bar{q}), plume area and flammability. It provided the nominal to slightly high values for mixing efficiency relative to the other pylons and slightly better values than the baseline. Losses appeared to be minimized in the wide configuration, and it provided the lowest values for the total pressure loss coefficient, indicating comparable to slightly better flow losses to the baseline. Additionally, the wide pylon's trajectory characteristics were similar

to the baseline despite the location of the wide's fuel plume outside the counter-rotating vortices.

Statistically, mixing efficiency (η_m), plume penetration height (h_p/d) and the total pressure loss coefficient ($\bar{\omega}$) best quantify the performance and loss. Pylons increase h_p/d but do not significantly change η_m and $\bar{\omega}$ when compared to baseline.

6.4. Recommendations for Future Action

The ability of the pylons to increase fuel penetration with similar mixing potential without additional flow losses compared to baseline indicates a good candidate for future study. To further clarify the shock features in the probing data, it is recommended that the probe resolution is increased. It is recommended that reacting research be conducted with the pylons to obtain a better understanding of their ability to provide mixed fuel for burning into the main flow. Verification of the trends suggested herein may be validated by additional measurements at far-field locations beyond $x = 30d$. Utilizing swirl injectors may increase fuel mixing and is a possible area of study. There is a lack of computational research concerning pylon-aided fuel injection, conducting such a study may shed light into to mechanics behind pylon-fuel jet interaction. An interesting area of further research would be in the creation of a computational model of the pylon-cavity system. Any results may then be compared to experimental data. Finally, the pylon system may be compared to other intrusive injection systems for comparison of mixing effectiveness and flow loss.

Appendix A Species Sampling and Aerothermodynamic Probing Data Meshes

The following data meshes give the number and order of data points used for both species sampling and the conventional probing. Gray areas are the tunnel coordinates programmed into the traverse through a computer interface. Note that the species sampling mesh only lists coordinates on the y -axis, the Raman procedure required only 29 transverse locations for each run, data points for the z -axis were obtained from image pixels (128 for each measurement plane). The data points and the order in which they are acquired are indicated within the array. For example, the last data point taken for the conventional probing was located at a (-0.5, 1.0) inches from the tunnel centerline (coordinates in z,y format) and was the 90th data point taken for each specific run.

Table 14. Species sampling data mesh used for each run


<u>DATA MESH</u>	Inches	mm
<u>PLANE #</u>		
29	1.000	25.40
28	0.960	24.38
27	0.920	23.37
26	0.880	22.35
25	0.840	21.34
24	0.800	20.32
23	0.760	19.30
22	0.720	18.29
21	0.680	17.27
20	0.640	16.26
19	0.600	15.24
18	0.560	14.22
17	0.520	13.21
16	0.480	12.19
15	0.440	11.18
14	0.400	10.16
13	0.360	9.14
12	0.320	8.13
11	0.280	7.11
10	0.240	6.10
9	0.200	5.08
8	0.160	4.06
7	0.120	3.05
6	0.080	2.03
5	0.040	1.02
4	0.000	0.00
3	-0.04	-1.02
2	-0.080	-2.03
1	-0.120	-3.05
<div style="text-align: center;">  Y Axis </div>		

Table 15. Aerothermodynamic probing data mesh used for each run

PROBING MESH									
Lane Haubelt									
9/22/2005									
<u>DATA MESH</u>	Yaxis								
(INCHES)	1	90	89	88	87	86	85	84	83
	0.875	73	74	75	76	77	78	79	80
	0.75	72	71	70	69	68	67	66	65
	0.625	55	56	57	58	59	60	61	62
	0.5	54	53	52	51	50	49	48	47
	0.375	37	38	39	40	41	42	43	44
	0.25	36	35	34	33	32	31	30	29
	0.125	19	20	21	22	23	24	25	26
	0	18	17	16	15	14	13	12	11
	-0.125	1	2	3	4	5	6	7	8
Zaxis		-0.5	-0.375	-0.25	-0.125	0	0.125	0.25	0.375
									0.5

Appendix B Image Correction Methods

Before any analysis of raw Raman images can occur, the images require correction for unwanted effects, as apparent in Figure 29. Many of these effects are a result of reflections off of surfaces other than the intended particles, nonuniform laser lighting and even CCD irregularities. The uncertainty due to these effects is discussed in Appendix E. Correction of raw images is a delicate process, and any changes must be done uniformly across all images. Any “fixing” of the image to make it look aesthetically pleasing must be avoided. Image correction is performed to reduce the two major sources of error seen: magnitude and signal oscillation. Three steps are used and described in the following paragraphs.

Background error presents itself as an overall irregular magnitude shift in intensity accompanied by oscillation around the magnitude seen in the data. This error is evident but difficult to characterize when viewing the Raman spectrum for a range of spanwise coordinates (as in Figure 29). Figure 52 gives the Raman spectrum at a single point ($x/d = 7.2$, $y/d = 16$, $z/d = -8$) for the wide configuration $\bar{q} = 4.0$, no injection. As mentioned previously, number densities of nitrogen and ethylene are proportional to the signal located at a wavenumber consistent with their respective Raman shift, which is indicated in the figure.

Step 1: Consider a raw image described by the array $I_{m,n}^r$ where m pixels represent the Raman shift and n pixels represent the tunnel spanwise coordinate (as defined previously), the superscript r indicates raw image. The local background magnitude error can be approximated as a constant intensity increase of the overall signal defined symbolically as B_n . This increase is different for each n spanwise location pixels. The

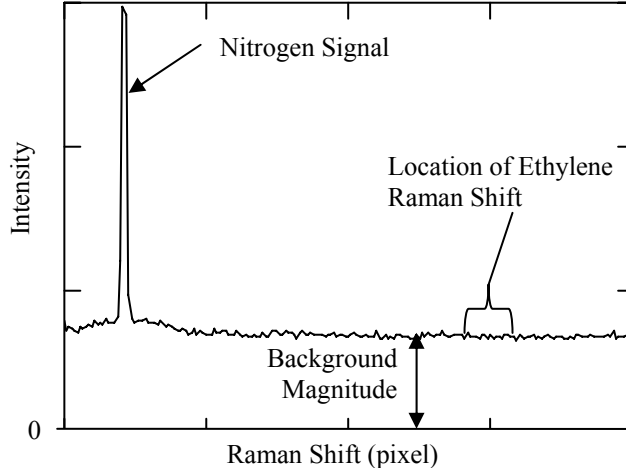


Figure 52. Raman scattering for wide insert at $x/d = 7.2$, $y/d = 16$, $z/d = -8$

background magnitude must be subtracted from the image. A method is determined from the average intensity of the signal between the Raman shifts of the nitrogen and ethylene buffered by 10 pixels either side, or:

$$B_n = \left(\frac{1}{m_{end} - m_{begin}} \right) \sum_{m=m_{begin}}^{m_{end}} I_{m,n}^r \quad (38)$$

where m_{begin} is the Raman shift pixel located at the last nitrogen signal pixel plus 10 and m_{end} is the Raman shift pixel located at the first ethylene signal pixel minus 10. Thus n background values are then subtracted from every pixel in n columns as shown below:

$$I_{m,n}^l = I_{m,n}^r - B_n \quad (39)$$

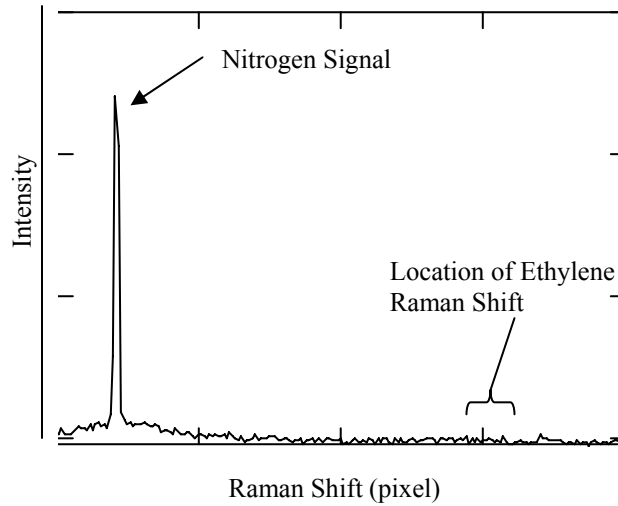


Figure 53. Background subtracted Raman scattering for wide insert, $x/d = 7.2$, $y/d = 16$, $z/d = -8$

Note that the superscript l indicates that the local magnitude is subtracted. Figure 53 shows the same Raman spectrum in Figure 52, except with the background magnitude subtracted. Notice the overall magnitude is not constant at zero (as should be expected for this case).

Step 2: After the local magnitude error is subtracted, the resulting equivalence ratio distribution across the tunnel span will still have a high amount of oscillation. Figure 54 shows the equivalence ratio distribution for the wide configuration, no injection at $x/d = 7.2$ and $y/d = 16$, with only local background magnitude subtracted as described in *step 1*. At this location, no fuel is present and the equivalence ratio should be constant at zero, however variation in Φ is still apparent.

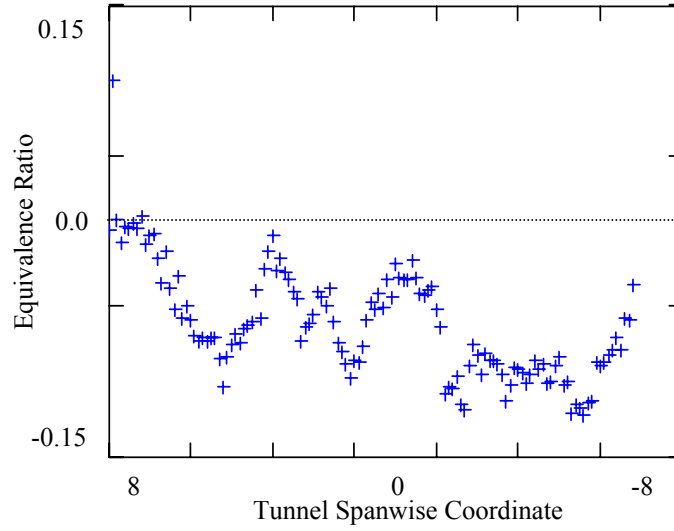


Figure 54. Equivalence ratio with correction step 1 for wide insert, $x/d = 7.2$ and $y/d = 16$

As mentioned in previous sections, the last five measurements taken from every data run are the five highest vertical locations in the test mesh (within the freestream). These measurements are taken without ethylene injection and processed through *step 1* listed above. These five freestream images with local background subtraction should be similar and are averaged together. The same variation in background magnitude in all data sets is seen in the averaged freestream image. This image ($\bar{I}_{m,n}^f$) may be subtracted from $I_{m,n}^l$ in the range of the ethylene integration area. This effectively rids the image of the background oscillation seen in Figure 54. Figure 55 shows the same data set as in Figure 54, except with the averaged freestream image subtracted. Notice, the equivalence ratio for this spatial location is approximately zero as expected. Standard deviation between Figure 54 and Figure 55 is decreased by an order of magnitude. The subtraction of image $\bar{I}_{m,n}^f$ is

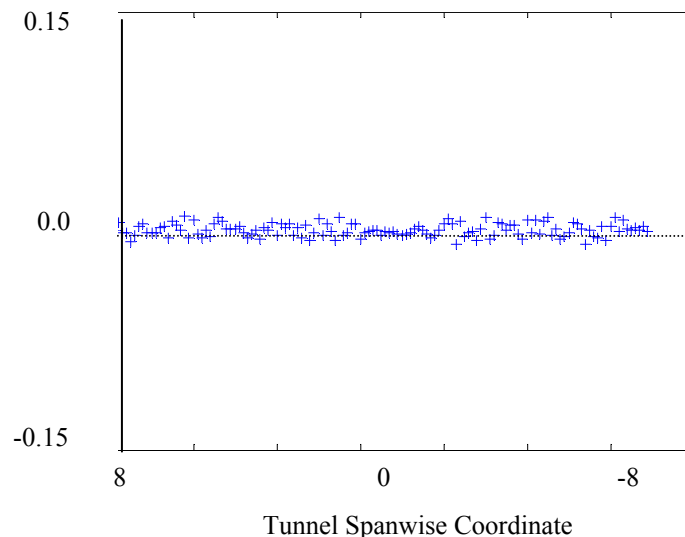


Figure 55. Equivalence ratio with correction steps 1 and 2, wide insert, at $x/d = 7.2$ and $y/d = 16$

applied to all data sets, and does not effect the overall equivalence ratio values obtained from the data reduction routine, rather it tends to reduce standard deviations in the images where little ethylene is present.

Step 3: Even with the background subtraction, noise is still noticeable in the figure. Many of these anomalies are due to the “salt and pepper” quality seen on the raw image, or individual pixels within the areas of integration at uncharacteristically high intensity values. A median filter is employed to all images to help reduce the noise’s occurrence. A median filter is a non-linear image enhancement technique which attempts to smooth out and suppress image noise while preserving the edges of physical features (such as peaks in ethylene and nitrogen).⁵⁶ For a given pixel $Px_{i,j}$ in an image whose location is (i,j) , the filtered intensity for that pixel is the median of an assignment array. The assignment array can be any size, typically about nine data points: eight data points in the immediate vicinity

Table 16. Illustration of assignment array used for median filtering

$Px_{i+1,j-1}$	$Px_{i+1,j}$	$Px_{i+1,j+1}$
$Px_{i,j-1}$	$Px_{i,j}$	$Px_{i,j+1}$
$Px_{i-1,j-1}$	$Px_{i-1,j}$	$Px_{i-1,j+1}$

plus the pixel being assigned. The assignment array used in the current median filter is illustrated in Table 16, where the pixel being assigned is $Px_{i,j}$. By picking the pixel with the median intensity value for assignment into pixel $Px_{i,j}$, any extreme outliers are thrown out. Figure 56 shows the spanwise equivalence ratio values with and without median filtering for the wide configuration at $\bar{q} = 4.0$, located at $x/d = 7.2$ and $y/d = 8$. This case has one of the greatest amount of additional noise seen in the data. Notice that the

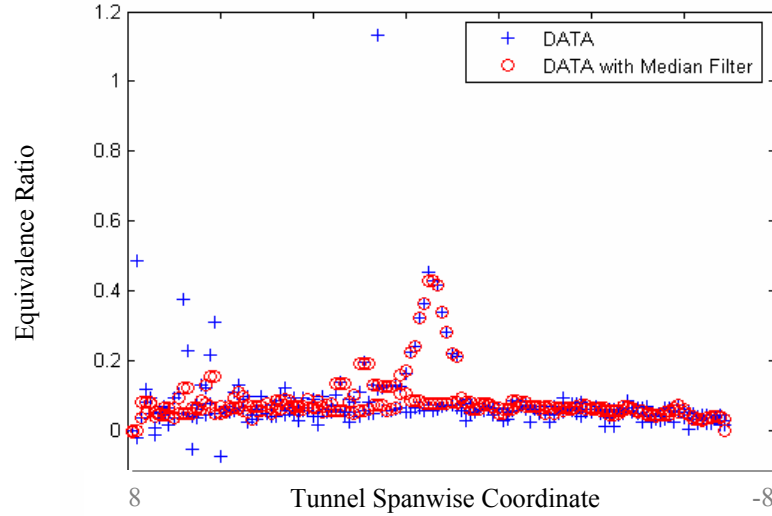


Figure 56. Equivalence ratios with and without correction Step 3, wide insert, $x/d = 7.2$ and $y/d = 8$

variation in equivalence ratio further away from the fuel is much tighter with median filtering and extreme outliers are for the most part discarded. Slight rounding off of the equivalence ratio peak is noticed but is not appreciable. This trend is uniform throughout all data sets.

All three correction steps were applied to every data set to ensure uniform application of correction. The goal of the steps is to isolate only the signals issuing from the species of interest and to discard any disconformities and unwanted scattering in an objective manner.

Appendix C High Resolution Equivalence Ratio Plots

The following appendix is presented to verify the similarities in plume structure between the two injection pressures. In section 5.3, equivalence ratio contours are given for all configurations using the same color bar scale. However, because of the lower injectant mass, resolution of the plume is limited at $\bar{q} = 1.0$. The following figures present the equivalence ratio contours of two example cases with a color bar range of $0.1 \leq \Phi \leq 3.0$.

The two cases shown are the baseline and wide configurations at $x/d = 12$ for both injection pressures. Note that overall plume area does not change when compared to the figures in section 5.3, but finer detail into fuel concentration distribution is seen at lower injection pressure. Figure 57 presents the baseline inserts equivalence ratio contours. Notice at low injection pressure, the vortex pair while apparent, are closer together and not as large as the high injection pressure condition. For the wide insert, Figure 58, the vortex pair is not seen and the majority of the fuel remains in the upper lobe. The observations seen at the lower injection pressure are related to the mass flow rate being injected into the freestream.

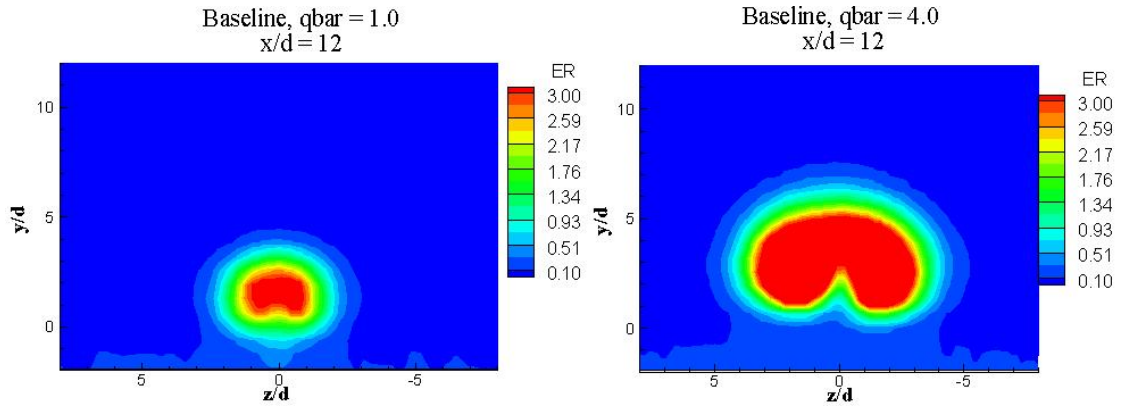


Figure 57. High resolution equivalence ratio contours for baseline, $\bar{q} = 1.0$ and 4.0

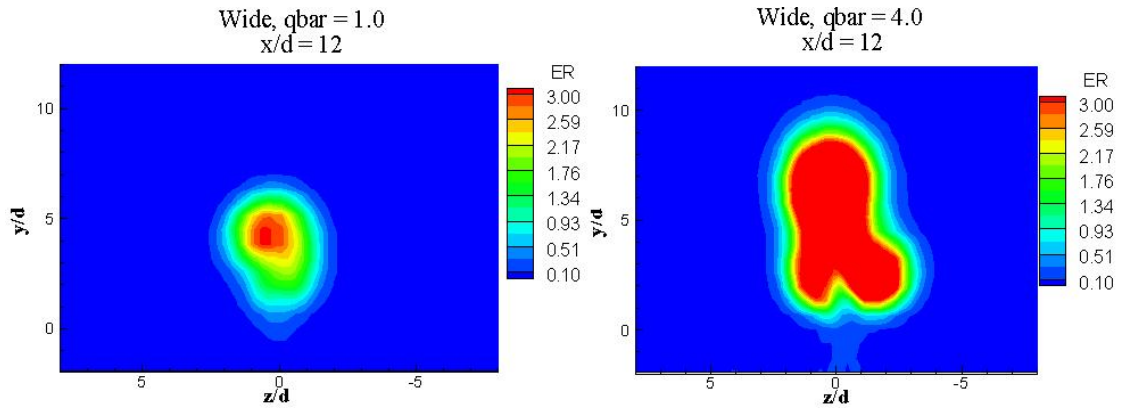


Figure 58. High resolution equivalence ratio contours for wide insert, $\bar{q} = 1.0$ and 4.0

Appendix D Method of Least Squares Correlation

The method of least squares is used to find correlations to all trajectory data presented in the report. The purpose of the method of least squares is to minimize the sum of the squares of the fit's offset (residual). Minimization of the sum of the squares allows residuals to be treated as a continuous function.⁵⁷ Mixing has historically shown variation with axial location in the form x^n , allowing close correlation with the power law curve fit.³²

The equation used for the correlations is presented in section 5.4.2.4 and is repeated below:

$$Y = A(X)^B \quad (40)$$

For a variable of interest Y the correlation is performed for three axial locations represented here as the independent variable X . In other words, a correlation is made for three data points in the form (X_i, Y_i) . The coefficients A and B are found below:

$$b = \frac{m \sum_{i=1}^m (\ln X_i \cdot \ln Y_i) - \sum_{i=1}^m (\ln X_i) \cdot \sum_{i=1}^m (\ln Y_i)}{m \sum_{i=1}^m (\ln X_i)^2 - \left(\sum_{i=1}^m (\ln X_i) \right)^2} \quad (41)$$

$$a = \frac{\sum_{i=1}^m (\ln Y_i) - b \sum_{i=1}^m (\ln X_i)}{m} \quad (42)$$

where $B = b$ and $A = e^a$.⁵⁷

Appendix E Error Analysis

E-1 Overview

All data this report presents is associated with error. The following section documents estimations for uncertainty and its sources. Both species sampling and conventional probing is analyzed. The analysis is done by simple assumptions and traditional uncertainty propagation with 95% confidence intervals. Table 17 and Table 18 give the uncertainty estimates for the species sampling and conventional probing respectively. A summary of the analysis techniques used is presented in the following sections.

Table 17. Species composition sampling uncertainty

x/d	$\pm 0.25d$
$y/d, h_p/d, h_c/d$	$\pm 0.32d$
z/d	$\pm 0.1d$
$A_p/A_b, A_c/A_i$	$\pm 0.04A_i$
ϕ	$\pm 3.8 \%$
ϕ_{max}	$+ 3.8\% : -3.8\% - 0.02$

Table 18. Aerothermodynamic probing uncertainty

x/d	$\pm 0.25d$	u^*	$\pm 1.3\%$
y/d	$\pm 1d$	P^*	$\pm 2.8\%$
z/d	$\pm 1d$	T^*	$\pm 0.8\%$
P_t^*	$\pm 2.8\%$	X_f	$\pm 2.8\%$
M^*	$\pm 1.7\%$	η_m	$\pm 4.3\%$
ρ^*	$\pm 3.0\%$	$\bar{\omega}$	$\pm 4.3\%$
		* See Reference 29	

E-2 Species Composition Sampling: Equivalence Ratio Uncertainty

The significant error sources in the Raman technique is systematic error in the optical calibration constants (k_i), and precision error from variations in individual measurements. Both these errors can be combined using the root of the sum of the squares (RSS) to give an uncertainty approximation. Error associated with the laser power and shutter exposure time variations are very small ($\sim 0.1\%$ or less) and assumed negligible.

The optical calibration constants are found by relating signal intensity with a known number density. The formulation is presented in equation 16 and is solved for both the nitrogen and ethylene components. Since tunnel temperature and pressure is used to determine the calibration constants, any error in tunnel property readings propagate into the calibration error. Tunnel error estimates for temperature is $\pm 1^\circ \text{F}$ and pressure is ± 0.036 psia, corresponding to $\pm 1.4\%$ variation in temperature and $\pm 0.25\%$ variation in pressure.

The number density for nitrogen (N_{N_2}) is found directly using the perfect gas relation, however, the ethylene number density $N_{C_2H_4}$ is a function of the tunnel temperature, pressure, and the nitrogen calibration constant (k_{N_2}). Note that the number densities are independent of each another since k_{N_2} and $N_{C_2H_4}$ are determined from two separate calibrations. The error from the tunnel readings (w_p and w_t) propagate into the calibration number density (w_n) and into the optical calibration constant (w_k). The equation for RSS is used to find an estimate for w_n which is proportional to the uncertainty found in density.

$$\frac{w_k}{k} \approx \frac{w_N}{N} = \frac{w_\rho}{\rho} = \left[\left(\frac{w_p}{P} \right)^2 + \left(\frac{w_T}{T} \right)^2 \right]^{\frac{1}{2}} \quad (43)$$

This leads to an error of $\pm 1.4\%$ for k_{N_2} and $\pm 2.0\%$ for $k_{C_2H_4}$. These errors are also the systematic errors for the species composition sampling.

Precision error is due to variation in signal between individual measurements resulting from primarily camera read noise and photon shot noise (which occurs when light photons are converted into electrons on the CCD). An estimate for the mean precision error ($P_{\bar{x}}$) is found by taking the standard deviation of the average pixel-to-pixel intensity between fourteen separate images at the same location and tunnel conditions. Since the degrees of freedom are less than 30, the standard deviation is then related to the precision uncertainty in the mean by a Student's t of 2.16. This leads to a $P_{\bar{x}}$ of $\pm 2.01\%$. Combining the precision and systematic errors using the RSS obtains an estimated uncertainty of $\pm 2.45\%$ for nitrogen number density and $\pm 2.84\%$ for ethylene. Since equivalence ratio

is derived from both number densities, an approximate uncertainty in equivalence ratio is $\pm 3.75 \%$.

As noted in Appendix B, median filtering is applied to all Raman data measurements. The filtering tended to “smooth” the spanwise equivalence ratio peaks (see Figure 56) by a $\Delta\Phi$ of about 0.02 or less. This additional error may be applied to the lower error bounds of equivalence ratio local maxima.

E-3 Aerothermodynamic Probing Uncertainty

All flow property uncertainty obtained from conventional probing are computed by Fuller as they appear in Table 18.²⁹ Those errors also propagate into the two derived quantities presented in this report, η_m and $\bar{\omega}$. Uncertainty estimates for η_m contain error from ethylene number density as found in the above section.

E-4 Dimensional Uncertainty

The axial location error is approximated by the systematic error from the initial alignment of the traverse with the origin. The error of the traversing table is several orders of magnitude less and is assumed insignificant. Traverse alignment is done with a standard ruler with a graduate of 1/32 inches. This creates an error of about $\pm 0.25d$ for the streamwise axis.

The transverse and spanwise uncertainties are primarily due to test mesh refinement, any error in the traversing mechanisms is assumed insignificant. All dimensional quantities in the y - z plane are not interpolated. Species sampling mesh refinement varies in the transverse and span coordinates based on laser beam width and pixel size. All vertical locations ($y/d, h_p/d, h_c/d$) have a variation of $\pm 0.32d$ and the spanwise locations z/d varies as $\pm 0.1d$. Therefore, variation in areas ($A_p/A_i, A_j/A_i$) is assumed to be $\pm 0.04A_i$. Probing dimensional variation is based on the diameter of the probes. Variation in the transverse and spanwise coordinate is $\pm 1d$.

Appendix F Supplimentary Pressure Data

The following images give the contour plots of raw pitot and cone-static pressure obtained from the probe measurements and the reduced static pressure as obtained from the Fuller algorithm. Contour plots are shown for all eight configurations. The color scales are unique for each plot.

Possible bow shock interaction with the probes and flow angle variation may cause distortion and inaccurate data in the region of the bow shock ($y/d > \sim 9$). Due to the cone-static pressure orifices being located downstream of the probe tip, unfavorable probe-shock interactions may occur, additionally changes in flow angle may prevent accurate the Taylor-McCall solutions in the vicinity of the bow shock. These conjectures, however, should be investigated more fully. Because of this uncertainty in the validity of the pressure data near the bow shock, all data to be used in analysis is taken below the region of the shock interaction.

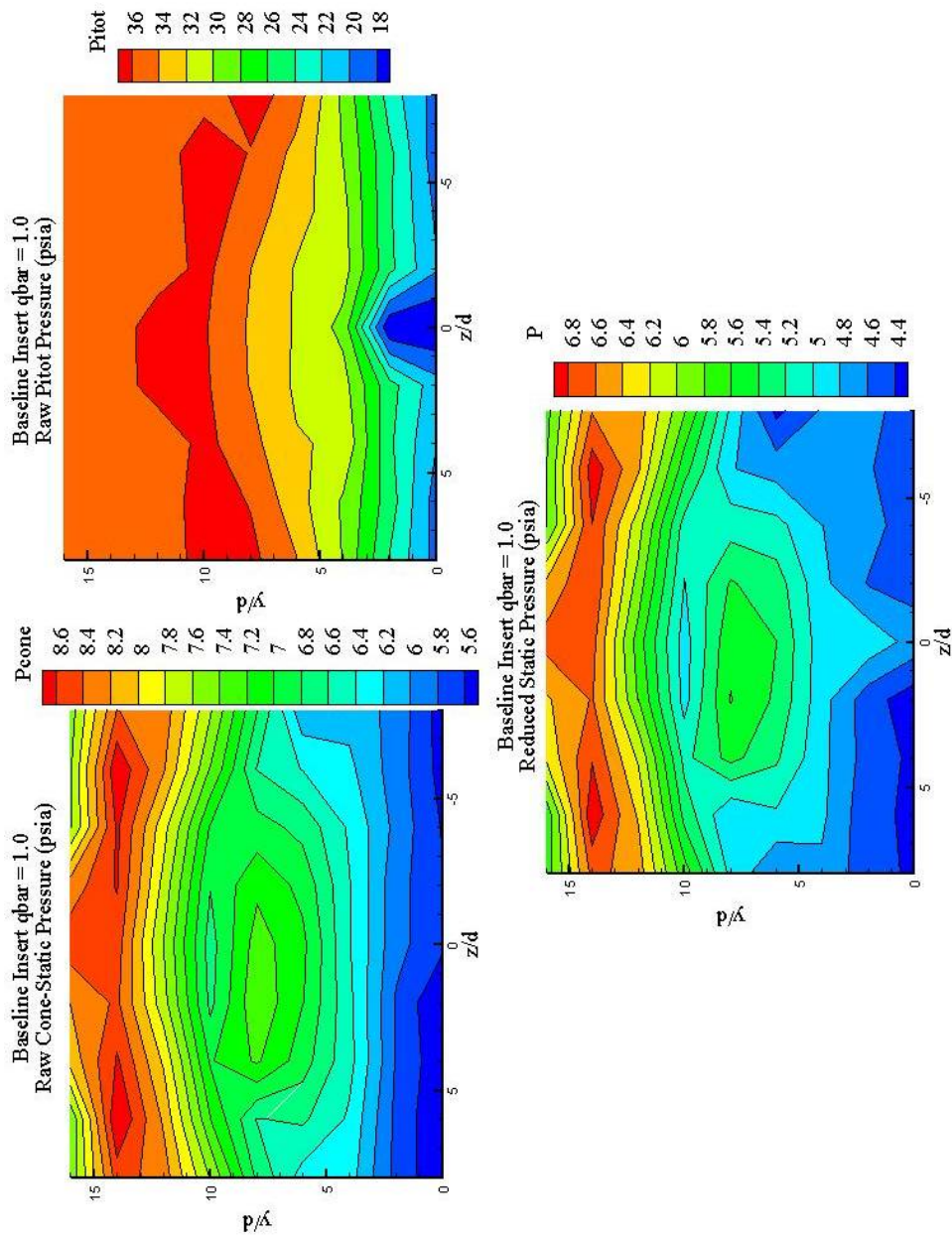


Figure 59. Supplementary pressure plots for baseline, $q = 1.0$ at $x/d = 12$

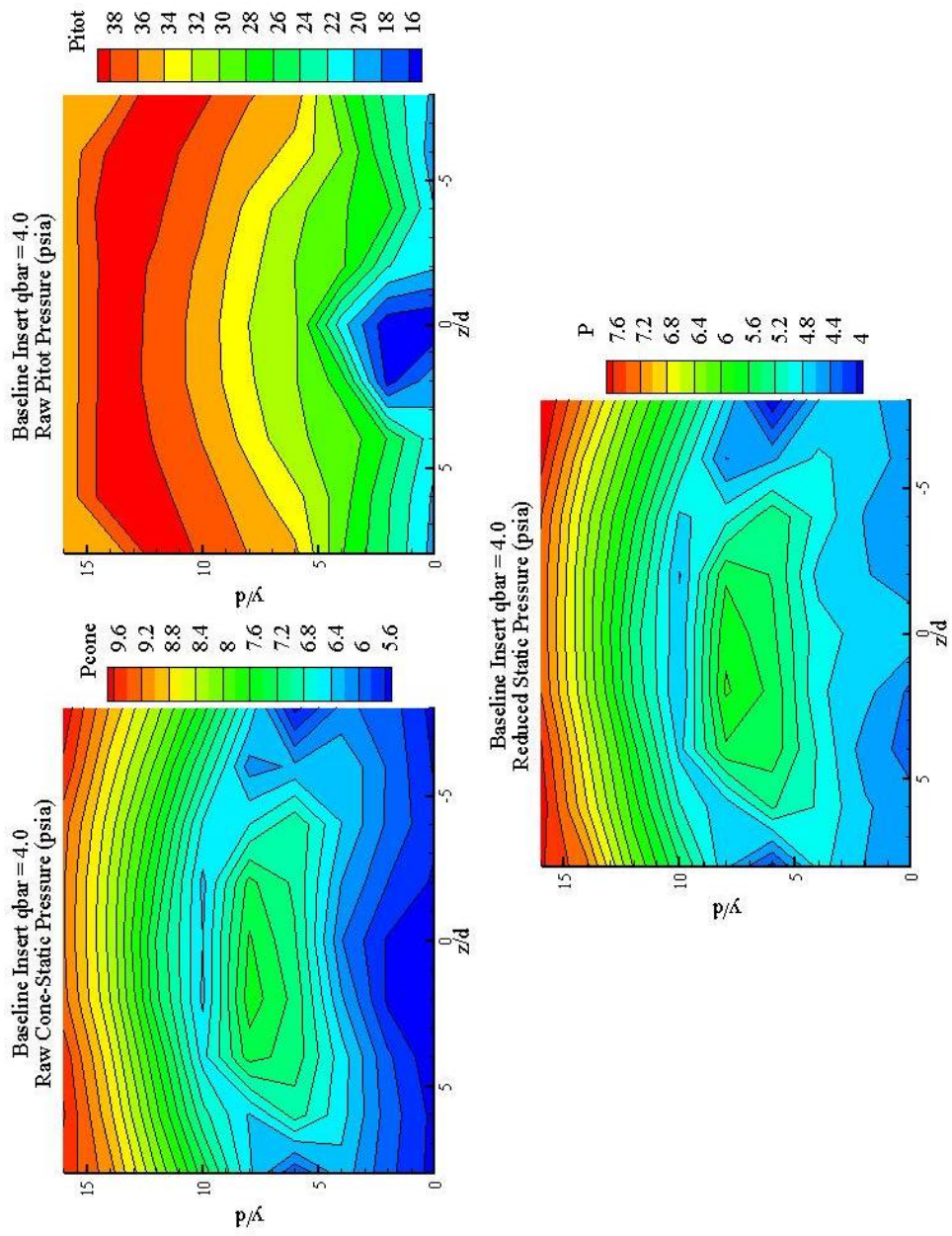


Figure 60. Supplementary pressure plots for baseline, $q = 4.0$ at $x/d = 12$

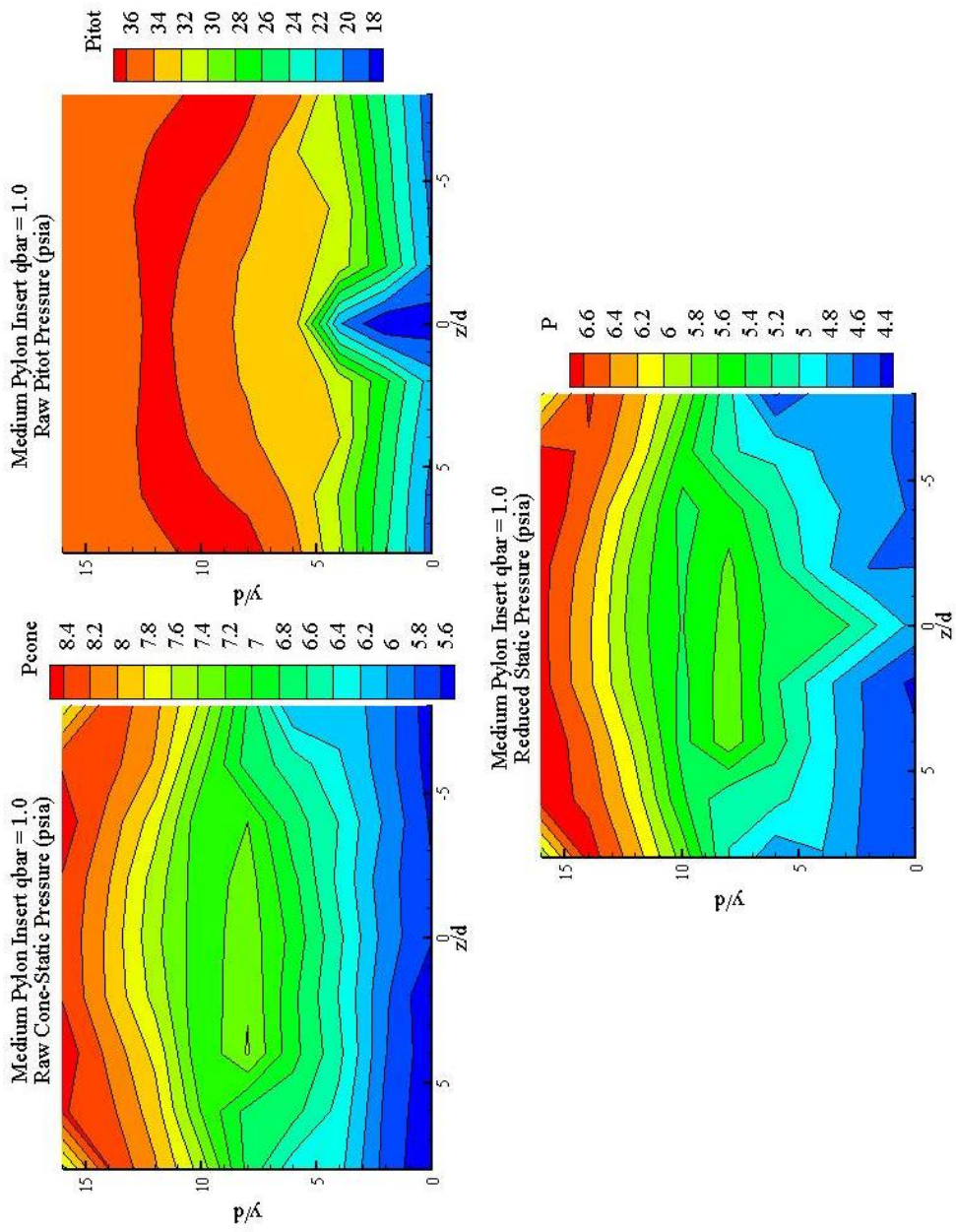


Figure 61. Supplementary pressure plots for the medium pylon, $q = 1.0$, at $x/d = 12$

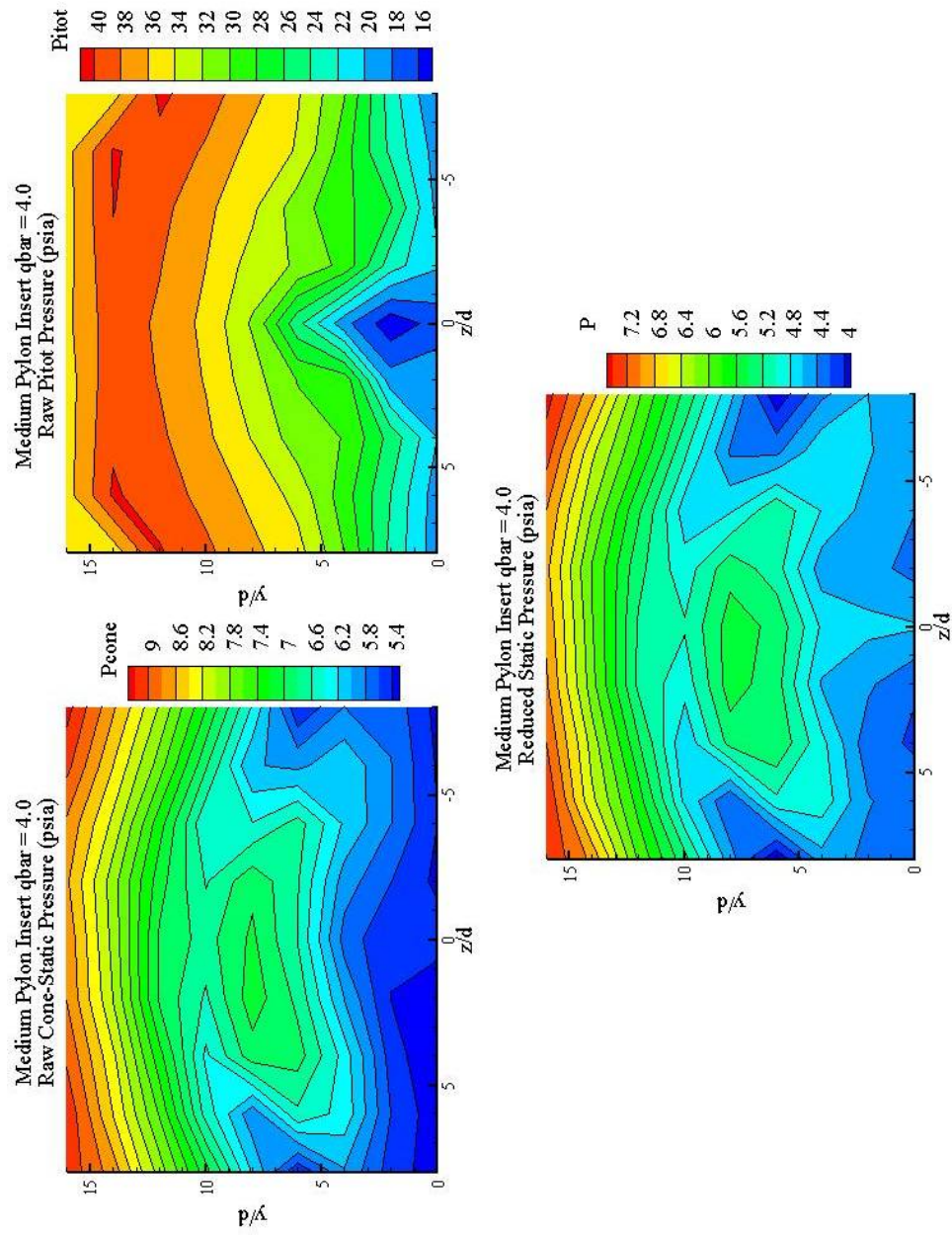


Figure 62. Supplementary pressure plots for the medium pylon, $q = 4.0$, at $x/d = 12$

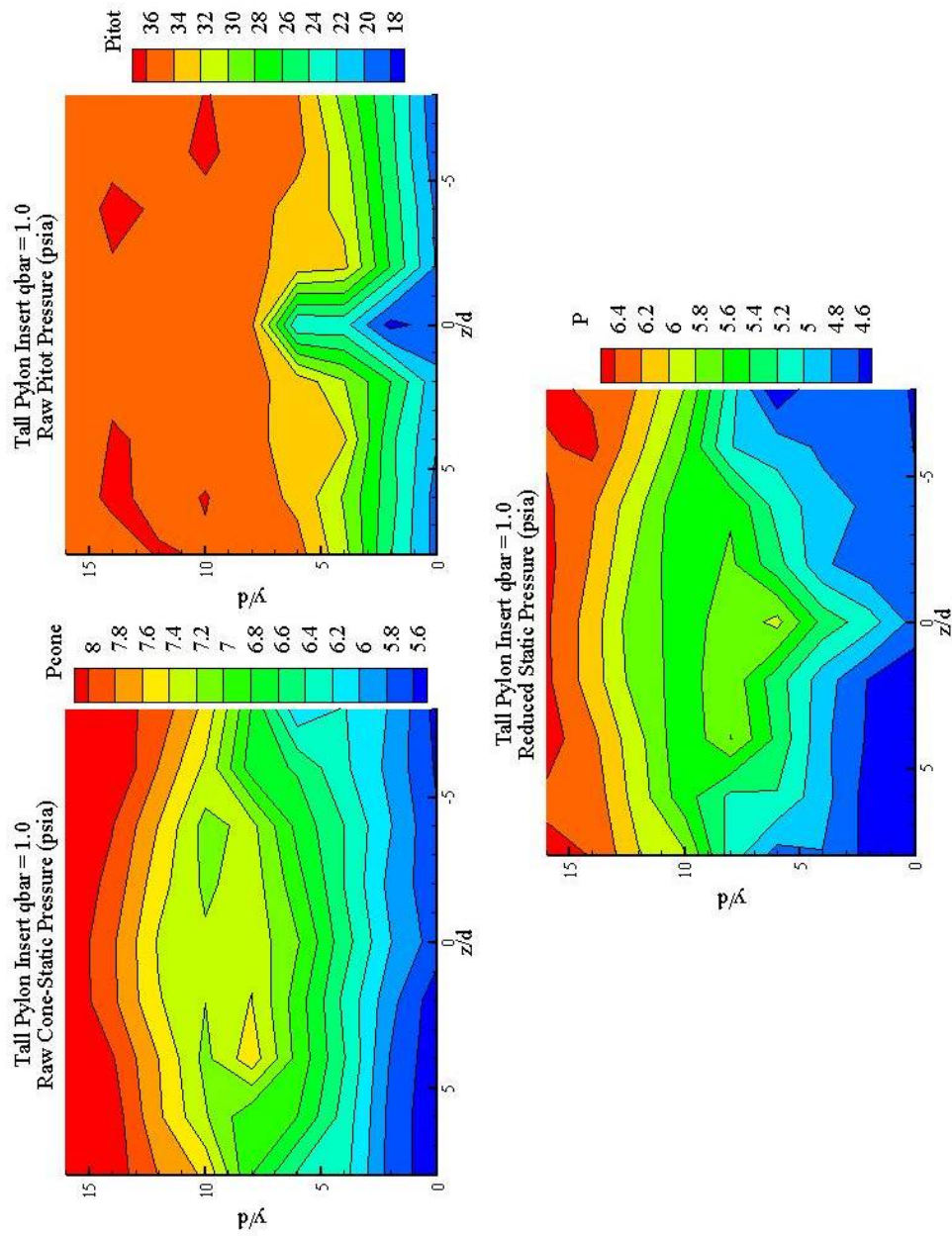


Figure 63. Supplementary pressure plots for the tall pylon, $q = 1.0$ at $x/d = 12$

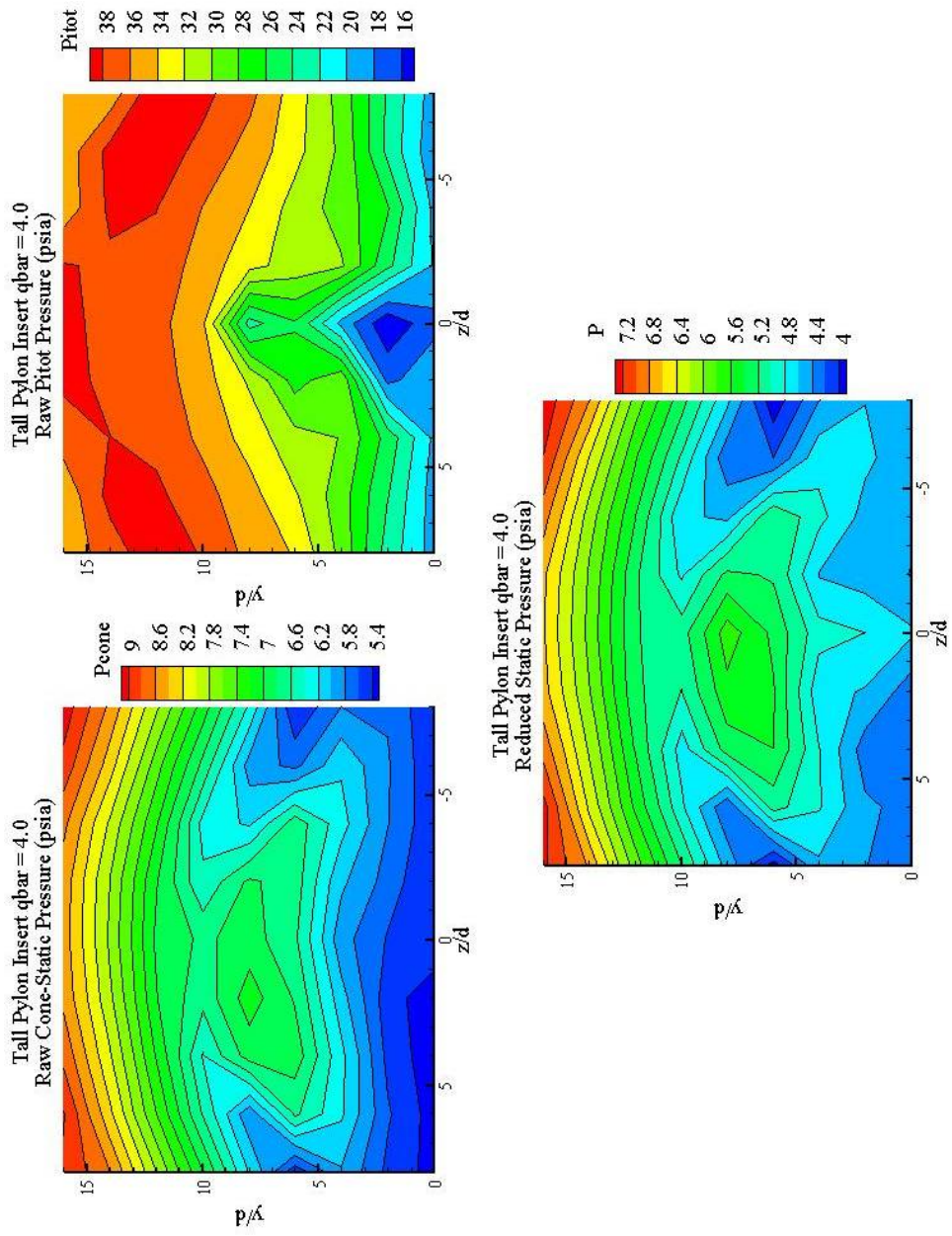


Figure 64. Supplementary pressure plots for the tall pylon, $q = 4.0$ at $x/d = 12$

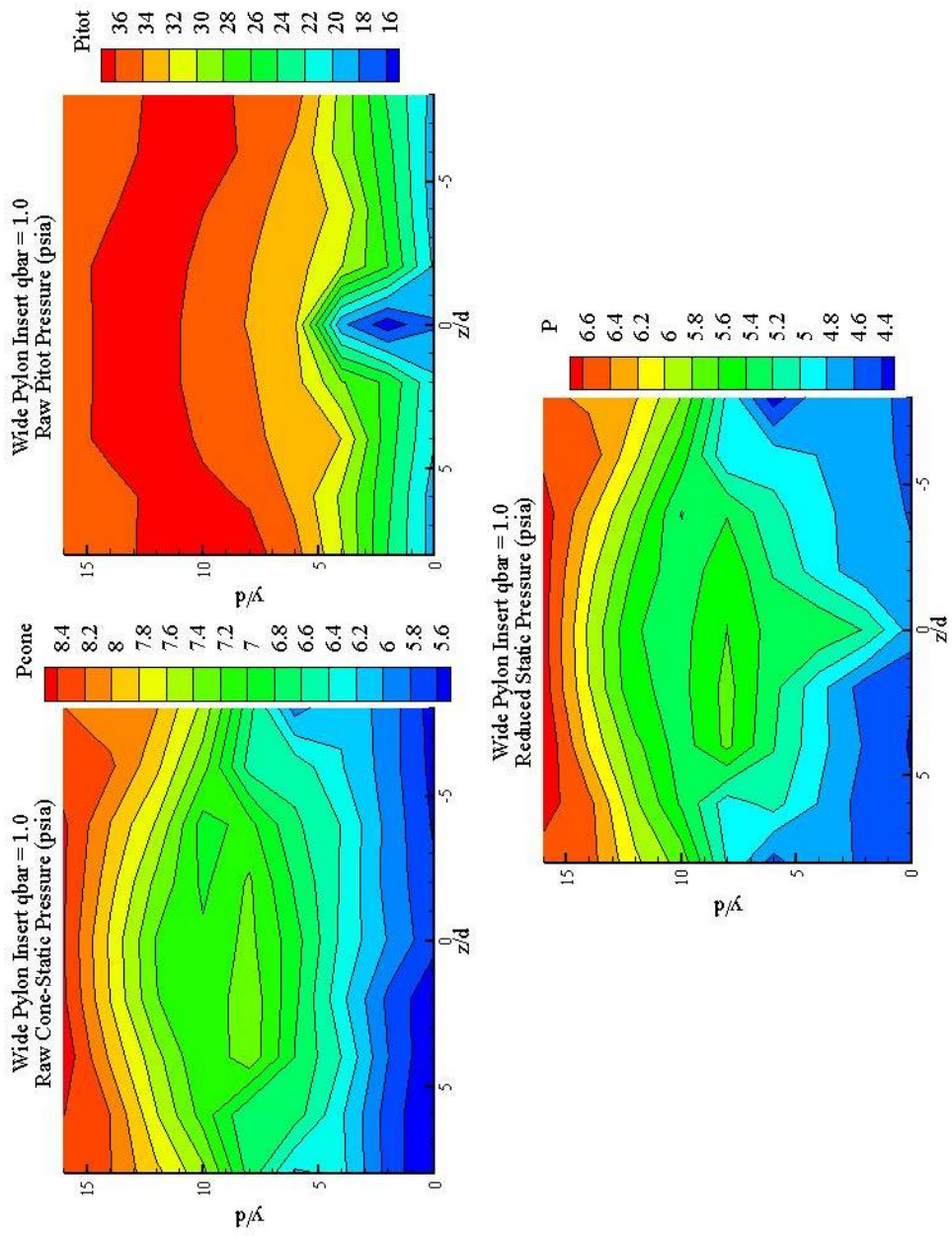


Figure 65. Supplementary pressure plots for the wide pylon, $q = 1.0$ at $x/d = 12$

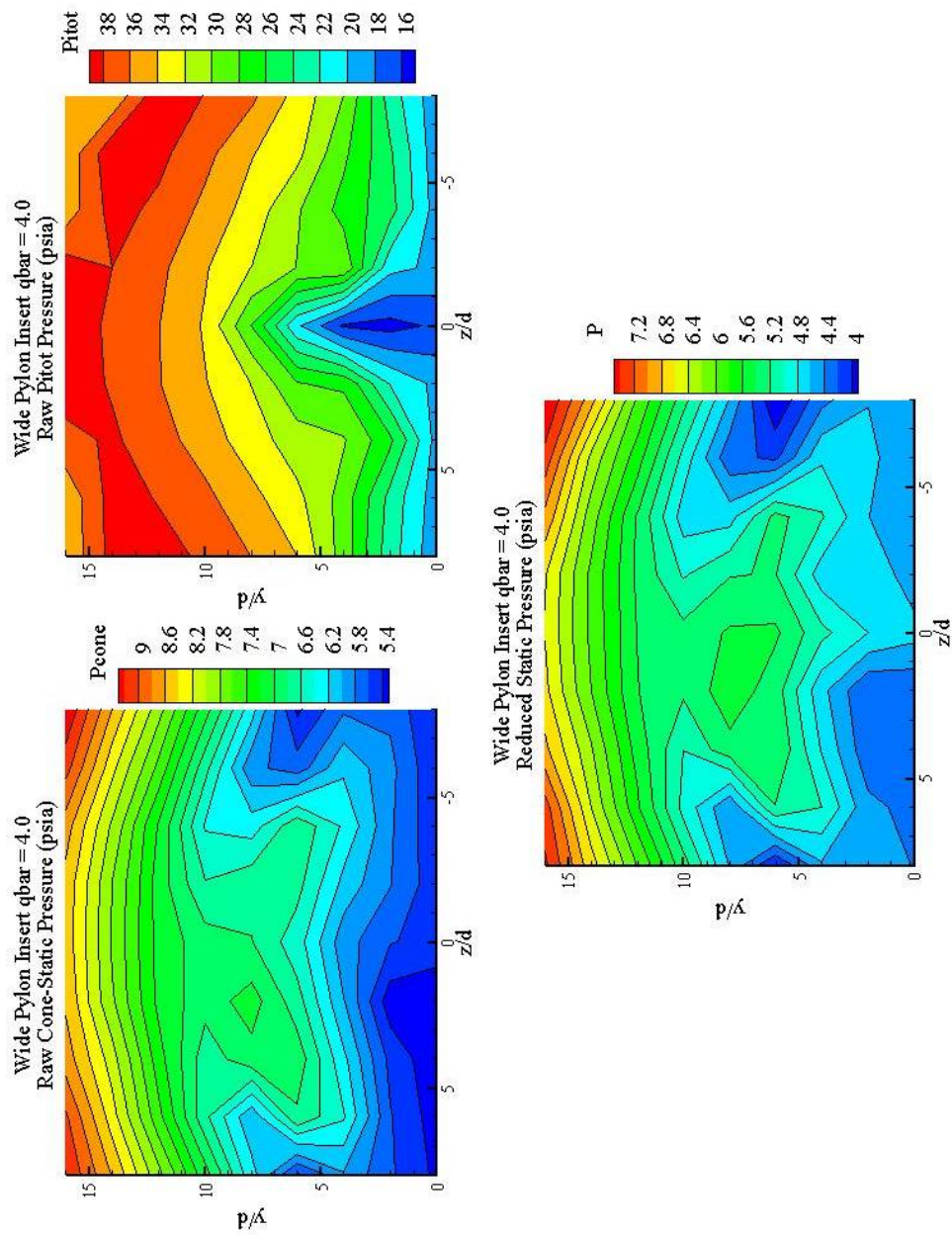


Figure 66. Supplementary pressure plots for the wide pylon, $q = 4.0$ at $x/d = 12$

Bibliography

- ¹ Gruber, M.R., Baurle, R.A., Mathur, T., and Hsu, K.-Y., “Fundamental Studies of Cavity-Based Flame holder Concepts for Supersonic Combustors,” AIAA Paper 99-2248, June 1999.
- ² Mathur, T., Gruber, M.R., Jackson, K., Donbar, J., Donaldson, W., Jackson, and T., Billig, F., “Supersonic Combustion Experiments with a Cavity-Based Fuel Injector”, *Journal of Propulsion and Power*, Vol. 17, No. 6, 2001, pp. 1305-1312.
- ³ Livingston, T., Segal, C., Schindler, M., and Vinogradov, V.A., “Penetration and Spreading of Liquid Jets in an External-Internal Compression Inlet”, *AIAA Journal*, Vol. 38, No. 6, 2000, pp. 989-994.
- ⁴ Vinogradov, V.A., Owens, M., Mullagiri, S., and Segal, C., “Effects of Fuel Pre-Injection on Mixing in a Mach 1.6 Airflow,” AIAA Paper, 99-45503, November 1999.
- ⁵ Montes, D.R., “Mixing Effects of Pylon-Aided Fuel Injection Located Upstream of a Flameholding Cavity in Supersonic Flow,” AFIT Thesis AFIT/GAE/ENY/05-M12, (Mar 05)
- ⁶ Gouskov, O., Kopchenov, V., and Vinogradov, V., “Numerical Research of Gaseous Fuel Pre-injection in Hypersonic 3-D Inlet,” AIAA Paper, 2000-3599, July 2000.
- ⁷ Livingston, T., and Segal, C., “Penetration and Spreading of Liquid Jets in an External-Internal Compression Inlet,” *AIAA Journal*, Vol. 38, No. 6, 2000, pp. 989-994.
- ⁸ Owens, M.G., Mullagiri, S., and Segal, C., “Effects of Fuel Preinjection on Mixing in Mach 1.6 Airflow,” *Journal of Propulsion and Power*, Vol. 17, No. 3, 2001, pp. 605-610.
- ⁹ Mattingly, Jack D., Elements of Gas Turbine Propulsion. New York:McGraw-Hill. 1996.
- ¹⁰ The Aviation History Online Museum. <http://www.aviation-history.com>. Accessed 1 February 2006.
- ¹¹ Hill, P.G., and Peterson, C.R., Mechanics and Thermodynamics of Propulsion. New York: Addison-Wesley. 1992.
- ¹² Powell, O.A., Edwards, J.T., Norris, R.B., Numbers, K.E., and Pearce, J.A., “Development of Hydrocarbon-Fueled Scramjet Engines: The Hypersonic Technology (HyTech) Program,” *Journal of Propulsion and Power*, Vol. 17, No. 6, 2001. pp. 1170-1176.

- ¹³ Tishkoff, J.M., Drummond, J.P., Edwards, T., and Nejad, A.S., "Future Directions of Supersonic Combustion Research," AIAA Paper 97-1017, January 1997.
- ¹⁴ Billig, Fredrick.S., "Research of Supersonic Combustion," *Journal of Propulsion and Power*, Vol. 9, No. 4, 1993, pp. 499-514.
- ¹⁵ Owens, M.G., Mullagiri, S., and Segal, C., "Thermal Choking Analyses in a Supersonic Combustor," *Journal of Propulsion and Power*, Vol. 17, No. 3, 2001, pp. 611-616.
- ¹⁶ Sabelnikov, V.A., Voloschenko, O.V., Ostras, V.N., and Sermanov, V.N., "Gasdynamics of Hydrogen-Fueled Scramjet Combustors," AIAA Paper 93-2145, June 1993.
- ¹⁷ Lewis, M. J., and Gupta, A.K., "Impact of Fuel Selection on Hypersonic Vehicle Optimization," International Symposium on Air Breathing Engines, Paper 97-7200, September 1997.
- ¹⁸ Ben-Yakar, A., and Hanson, R.K., "Cavity Flame holders for Ignition and Flame Stabilization in Scramjets: An Overview," *Journal of Propulsion and Power*, Vol. 17, No. 4, 2001, pp. 869-877.
- ¹⁹ Abbitt, J.D., Segal, C., McDaniel, J.C., Krauss, R.H., and Whitehurst, R.B., "Experimental Supersonic Hydrogen Combustion Employing Staged Injection Behind a Rearward-Facing Step," *Journal of Propulsion and Power*, Vol. 9, No. 3, 1993, pp. 472-479.
- ²⁰ Riggins, D.W., McClinton, C.R., Rogers, R.C., and Bittner, R.D., "Investigation of Scramjet Injection Strategies for High Mach Number Flows," *Journal of Propulsion and Power*, Vol. 11, No.3, 1995, pp. 409-418.
- ²¹ Fuller, R.P., Wu, P., Nejad, A.S., and Schetz, J.A., "Comparison of Physical and Aerodynamic Ramps as Fuel Injectors in Supersonic Flows," *Journal of Propulsion and Power*, Vol. 14, No. 2, 1998, pp. 135-145.
- ²² Huellmantel, L.W., Ziemer, R.W., and Cambel, A.B., "Stabilization of Premixed Propane-Air Flames in Recessed Ducts," *Jet Propulsion*, January 1957, pp. 31-43.
- ²³ Perng, S.W., and Dolling, D.S., "Passive Control of Pressure Oscillations in Hypersonic Cavity Flow," AIAA Paper 98-0776, January 1998.
- ²⁴ Zhang, X., Rona, A., and Edwards, J.A., "The Effect of Trailing Edge Geometry on Cavity Flow Oscillation Driven by a Supersonic Shear Layer," *Aeronautical Journal*, March 1998, pp. 129 -136.

- ²⁵ Yu, K.H., Wilson, K.J., and Schadow, K.C., "Effect of Flame-Holding Cavities on Supersonic-Combustion Performance," *Journal of Propulsion and Power*, Vol. 17, No. 6, 2001, pp. 1287 – 1295.
- ²⁶ Gruber, M.R., Baurle, R.A., Mathur, T., and Hsu, K.-Y., "Fundamental Studies of Cavity-Based Flame holder Concepts for Supersonic Combustors," *Journal of Propulsion and Power*, Vol. 17, No. 1, 2001, pp. 146 – 153.
- ²⁷ Ben-Yakar, A., and Hanson, R.K., "Supersonic Combustion of Corss-Flow Jets and Influence of Cavity Flame-Holders," AIAA Paper 99-0484, January 1999.
- ²⁸ Yu, K., Wilson, K.J., Smith, R.A., and Schadow, K.C., "Experimental Investigation on Dual-Purpose Cavity in Supersonic Reacting Flows," AIAA Paper 98-0723, January 1998.
- ²⁹ Hsu, K.-Y., Carter, C., Crafton, J., Gruber, M., Donbar, J., Mathur, T., Schommer, D., and Terry, W., "Fuel Distribution about a Cavity Flame holder in Supersonic Flow," AIAA Paper 2000-3585, July 2000.
- ³⁰ Mays, R.B., Thomas, R.H., and Schetz, J.A., "Simulated Fuel Injection Through Wedge-Shaped Orifice Into Supersonic Flow," AIAA Paper 89-2461, July 1989.
- ³¹ McMillin, B.K., Seitzman, J.M., and Hanson, R.K., "Comparison of NO and OH Planar Fluorescence Temperature Measurements in Scramjet Model Flowfields," *AIAA Journal*, Vol. 32, No. 10, 1994, pp. 1945-1952.
- ³² Schetz, J.A., Thomas, R.H., and Billig, F.S. "Mixing of Transverse Jets and Wall Jets in Supersonic Flow," *Seperated Flows and Jets*, edited by V.V. Kozlov and A.V. Dovgal, Springer-Verlag, Berlin, 1991.
- ³³ Schetz, J.A., and Billig, F.S., "Penetration of Gaseous Jets Injected into a Supersonic Stream," *Journal of Spacecraft and Rockets*, Vol. 3, No. 11, 1966, pp. 1658-1665.
- ³⁴ VanLerberghe, W.M., Santiago, J.G., Dutton, J.C, and Lucht, R.P., "Mixing of a Sonic Trasverse Jet Injected into a Supersonic Flow," *AIAA Journal* Vol 38., No. 3, 2000, 470-479.
- ³⁵ Gruber, M.R., Nejad, A.S., Chen, T.H., and Dutton, J.C., "Transverse Injection from Circular and Elliptic Nozzles into a Supersonic Crossflow," *Journal of Propulsion and Power*, Vol. 16, No. 3, 2000. 449-457.
- ³⁶ Orth, R.C., Schetz, J.A., and Billig, F.S., "The Interaction and Penetration of Gaseous Jets in Supersonic Flow," NASA CR-1386, July 1969.
- ³⁷ Kelso, R.M., Lim, T.T., and Perry, A.E., "An Experimental Study of Round Jets in Crossflow," *Journal of Fluid Mechanics*, Vol. 306, pp. 111-144, January 1996.

- ³⁸ Murugappan, S., Gutmark, E., Carter, C., Donbar, J., Gruber, M., and Hsu, K.-Y., "Control of a Transverse Supersonic Jet Injection into a Supersonic Cross-Stream," AIAA Paper 2004-1204, January 2004.
- ³⁹ Northam, G.B., Greenberg, I., and Byington, C.S., "Evaluation of Parallel Injector Configurations for Supersonic Combustion," AIAA Paper 89-2525, July 1989.
- ⁴⁰ Gruber, M.R., and Nejad, A.S., "New Supersonic Combustion Research Facility," *Journal of Propulsion and Power*, Vol. 11, No. 5, 1995, pp. 1080-1083.
- ⁴¹ National Institute of Standards and Technology Thermophysical Properties of Fluid Systems. <http://www.nist.gov/chemistry/fluid> Accessed 1 November 2005.
- ⁴² Anderson, John D. Fundamentals of Aerodynamics. 3rd Ed. New York: McGraw-Hill. 2001.
- ⁴³ Demtröder, Wolfgang. Laser Spectroscopy: Basic Concepts and Instrumentation. New York: Springer-Verlag. 1981.
- ⁴⁴ Eckbreth, Alan C. Laser Diagnostics for Combustion Temperature and Species. Cambridge: Abacus. 1988.
- ⁴⁵ Ferraro, J.R., and Kazuo, N. Introductory Raman Spectroscopy. San Diego: Academic Press. 1994.
- ⁴⁶ Bombach, Roff. ERCOFTEC Summer School, March 2002, Zurich, Paul Scherrer Institut. pp. 3.1 – 3.18.
- ⁴⁷ Liepmann, H. W., and Roshko, A., Elements of Gasdynamics. Mineola : Dover Publications. 1985.
- ⁴⁸ Fuller, Raymond P., "Fuel-Vortex Interactions for Enhanced Mixing In Supersonic Flow," Ph.D. Dissertation, Department of Aerospace and Ocean Engineering, Virginia Polytechnic Institute and State University, Blacksburg, VA, 1996.
- ⁴⁹ Winkler, E.M., "Design and Calibration of Stagnation Temperature Probes for Use at High Supersonic Speeds and Elevated Temperatures," *Journal of Applied Physics*, Vol. 25, 1954, pp 231.
- ⁵⁰ Wheeler, A.J., and Ganji, A.R., Introduction to Engineering Experimentation. Upper Saddle River : Prentice Hall. 1996.
- ⁵¹ Yang, Wen-jei. Handbook of Flow Visualization. Taylor and Francis. 1989.
- ⁵² Kuo, Kenneth, K., Principles of Combustion. 2nd Ed. Hoboken : John Wiley and Sons, Inc. 2005.

- ⁵³ Sims, J.L., "Tables for Supersonic Flow Around Right Circular Cones at Zero Angle of Attack," NASA SP-3004, 1964.
- ⁵⁴ Glassman, Irvin. Combustion. 3rd ed. New York: Academic Press, 1996.
- ⁵⁵ Mao, M., Riggins, D.W., and McClinton, C.R., "Numerical Simulation of Transverse Fuel Injection," NASP CR 1089, May 1990.
- ⁵⁶ Russ, John C., The Image Processing Handbook. 4th Ed. Boca Rotan : CRC Press. 2002.
- ⁵⁷ Weisstein, Eric, W., "Least Squares Fitting--Power Law." *MathWorld*
<http://mathworld.wolfram.com/LeastSquaresFittingPowerLaw.html>.

Vita

Second Lieutenant Lane C. Haubelt graduated from Mary Carroll High School in Corpus Christi, Texas. He entered undergraduate studies at the United States Air Force Academy in Colorado Springs, Colorado where he graduated with a Bachelor in Science degree in Aeronautical Engineering. He was recognized as a Distinguished Graduate and received his commission in June 2004.

In August of 2004, he entered the Graduate School of Engineering and Management, Air Force Institute of Technology. There he sequenced in aerodynamics and rocket propulsion. His thesis research was under the direction of Dr. Paul I. King. Upon graduation, he will be assigned to the 412th Flight Test Wing at Edwards AFB, California.

REPORT DOCUMENTATION PAGE				Form Approved OMB No. 074-0188	
<p>The public reporting burden for this collection of information is estimated to average 1 hour per response, including the time for reviewing instructions, searching existing data sources, gathering and maintaining the data needed, and completing and reviewing the collection of information. Send comments regarding this burden estimate or any other aspect of the collection of information, including suggestions for reducing this burden to Department of Defense, Washington Headquarters Services, Directorate for Information Operations and Reports (0704-0188), 1215 Jefferson Davis Highway, Suite 1204, Arlington, VA 22202-4302. Respondents should be aware that notwithstanding any other provision of law, no person shall be subject to a penalty for failing to comply with a collection of information if it does not display a currently valid OMB control number.</p> <p>PLEASE DO NOT RETURN YOUR FORM TO THE ABOVE ADDRESS.</p>					
1. REPORT DATE (DD-MM-YYYY) 23-03-2006		2. REPORT TYPE Master's Thesis		3. DATES COVERED (From – To) August 2004 – March 2006	
4. TITLE AND SUBTITLE Aerodynamic Loss and Mixing over a Cavity Flame Holder Downstream of Pylon-Aided Fuel Injection				5a. CONTRACT NUMBER	
				5b. GRANT NUMBER	
				5c. PROGRAM ELEMENT NUMBER	
6. AUTHOR(S) Haubelt, Lane, C., Second Lieutenant, USAF				5d. PROJECT NUMBER	
				5e. TASK NUMBER	
				5f. WORK UNIT NUMBER	
7. PERFORMING ORGANIZATION NAMES(S) AND ADDRESS(S) Air Force Institute of Technology Graduate School of Engineering and Management (AFIT/EN) 2950 Hobson Way, Building 640 WPAFB OH 45433-8865				8. PERFORMING ORGANIZATION REPORT NUMBER AFIT/GAE/ENY/06-M13	
9. SPONSORING/MONITORING AGENCY NAME(S) AND ADDRESS(ES) Gruber, M. R. AFRL/PRAS 1950 Fifth Street Wright-Patterson Air Force Base, OH, 45433				10. SPONSOR/MONITOR'S ACRONYM(S)	
				11. SPONSOR/MONITOR'S REPORT NUMBER(S)	
12. DISTRIBUTION/AVAILABILITY STATEMENT APPROVED FOR PUBLIC RELEASE; DISTRIBUTION UNLIMITED.					
13. SUPPLEMENTARY NOTES					
14. ABSTRACT Cavity-based fuel injection and flame holding found in hydrocarbon-fueled scramjet applications are of interest. The Air Force Research Lab (AFRL) and the Air Force Institute of Technology (AFIT) at Wright-Patterson Air Force Base in Ohio are investigating the enhancement of fuel-air mixing with small pylons that project into the supersonic flow upstream of a flame holder cavity. This follows previous qualitative (Mie scattering and NO-PLIF visualizations) results which suggested that injection behind pylons, may improve fuel-air mixing. Three pylons geometries (medium, tall, and wide) shaped as thin triangular wedges with a 30° inclination angle were tested and compared to baseline transverse injection without pylons at two injection pressures. The AFRL provided facility, was a supersonic (Mach 2) continuous flow wind tunnel with existing cavity and pylon setup. The goal was to measure mixing efficiency and shock loss of each pylon setup for comparison to the baseline condition of transverse injection without pylons. Non-reacting flow was measured using conventional probing and spontaneous Raman spectroscopy to obtain pitot pressure, total temperature, cone-static pressure and species concentration over the cavity downstream of the injection. Results demonstrated that pylons increase fuel penetration, while not adding significantly to shock losses or overall mixing compared to baseline.					
15. SUBJECT TERMS Propulsion System Components, Supersonic Combustion, Pylon Injection, Jet Mixing Flow, Raman Scattering					
16. SECURITY CLASSIFICATION OF:			17. LIMITATION OF ABSTRACT	18. NUMBER OF PAGES	19a. NAME OF RESPONSIBLE PERSON
a. REPORT	b. ABSTRACT	c. THIS PAGE			Dr. Paul I. King (ENY)
U	U	U	UU	170	19b. TELEPHONE NUMBER (Include area code) (937) 255-3636, ext 4628 (paul.king@afit.edu)